Chemical Industry & Chemical Engineering Quarterly

SERBIA

Belgrade

AChE

Chemical Industry & Chemical Engineering CI&CE Quarterly

| Vol. 31 | Belgrade, January-March 2025 | No. 1 |

CONTENTS

The activities of the Association of Chemical Engineers of Serbia are supported by:

GANG FU[1]

RUIEN YU[1,2]

XIAOLIN YU[1]

XIAOHAN LI[1]

XIAOWEN CHEN[3]

XIAOYAN ZHANG[2]

YANFEI KOU[1]

XIJING ZHU[1]

[1]Shanxi Key Laboratory of Advanced Manufacturing Technology, North University of China, Taiyuan, China

[2]Shanxi Transportation Technology Research & Development Co., Ltd, Taiyuan, China

[3]State Key Laboratory of Special Functional Waterproof Materials, Beijing Oriental Yuhong Waterproof Technology Co., Ltd, Beijing, China

NUMERICAL SIMULATION ON THE PROCESSING OF CRUMB RUBBER-MODIFIED ASPHALT BY ULTRASOUND AND MECHANICAL STIRRING

Article Highlights
- Fluid simulation of modified asphalt is conducted under ultrasound and stirring processing
- The cavitation volume fraction in the tank changes periodically with the ultrasound effect
- The cavitation strength of modified asphalt is compared in the different system viscosities

Abstract

Based on the existing modified asphalt production equipment, the power ultrasound is integrated into the existing stirring dispersion technology, and the FLUENT fluid simulation is used to combine ultrasonic action and stirring. Stirring and ultrasonic action, two motion forms, were realized step by step, and the movement states of crumb rubber-modified asphalt were simulated under the interaction of ultrasonic and stirring, which provided a new method for the research of crumb rubber-modified asphalt production equipment. The results show that under the action of ultrasound, only positive pressure exists in the modified asphalt flow field after adding the cavitation model, and the maximum absolute pressure can reach about 1200 kPa. With the increase of ultrasonic time, the air content rate under the tool head is periodic and regularly changed and will gradually increase, the number of cavitation bubbles will continue to increase, and the cavitation intensity will increase. The influence of asphalt viscosity on the volume fraction of cavitation bubbles was studied, when the viscosity of the system is 0.8 Pa·s, it is more conducive to the occurrence of cavitation, The process of ultrasonic synergistic stirring is conducive to inhibiting the segregation phenomenon of crumb rubber modified asphalt.

Keywords: ultrasound; cavitation; crumb rubber modified asphalt; mechanical stirring; CFD simulation.

Asphalt is one of the indispensable materials in the process of expressway construction. Due to various reasons such as the increase in traffic volume and global warming, base asphalt cannot meet the needs of expressway construction [1,2], polymer modification is currently one of the most common methods to improve the performance of asphalt, and polymer-modified asphalt has been widely used in road construction [3–6]. With the increase in the number of cars in the world, waste tires as a new "black pollution", its number is also increasing, the waste tires broken into crumb rubber as a modifier added to the asphalt, not only reduce the production cost of modified asphalt but also achieve waste utilization, green development [7–8].

At present, the modification of base asphalt is mainly based on the addition of one or more polymers. Ameri *et al.* [9] studied the effect of ethylene vinyl acetate copolymer (EVA) content on the storage stability of asphalt and found that the greater the amount of EVA in asphalt, the greater the degree of segregation. Xiao *et al.* [10] analyzed the rheological

1

properties of the modified asphalt binder with crumb rubber added at high temperatures, and the results showed that the rheological properties of the modified binder depend on the polymer type and asphalt source. Liu *et al.* [11] tested the conventional performance, rheological properties, and infrared spectroscopy test analysis, and found that amorphous poly alpha olefin (APAO) can greatly improve the anti-aging performance of asphalt. Jiang *et al.* [12] prepared epoxy styrene butadiene styrene block polymer (SBS)-modified asphalt and found that the properties of epoxy SBS-modified asphalt depended on the ratio of styrene/butadiene (S/B), the compatibility of SBS and asphalt, the average molecular weight of SBS, and the dispersion of SBS-modified asphalt particles in the continuous epoxy phase. Leng *et al.* [13] conducted experimental studies on composite WTR (waste tire rubber) and waste polyethylene (PE) or polyethylene terephthalate (PET) modified asphalt, and the experimental results proved that the composite-modified asphalt improved the performance of rutting deformation. Ding *et al.* [14] compared the performance of ordinary asphalt recycled material and stable crumb rubber asphalt (SCRA) recycled asphalt mixture and found that the low-temperature performance of SCRA recycled asphalt mixture could be further improved, while other properties remained at a high level. By studying the foaming conditions of foamed warm mix asphalt with crumb rubber (FWMA-CR) binder and combining with the performance evaluation of FWMA-CR binder and mixture, Hu *et al.* [15] found that compared with the hot-mix asphalt mixture containing rubber debris (HMA-CR), the manufacturing temperature of FWMA-CR mixture dropped by 17 °C. The foamed rubber asphalt binders and mixtures showed better low-temperature performance and fatigue resistance, but poor high performance.

Li *et al.* [16] adopted the orthogonal experimental design method and found that when 2% nano-montmorillonite and 8% SBS were cut for 150 min at a shear temperature of 170 °C and a shear rate of 4000 rpm, the modified asphalt with a high content of SBS had good high and low-temperature performance and the best compatibility. Traditional methods by adding surfactants, compatibilizers, stabilizers, and other chemical reagents to promote the compatibility of the two phases and the stability of the blending system, but chemical reagents are not conducive to clean production, and although the performance of asphalt can be improved by adding a modifier, but with the extension of storage time, the modified asphalt will also appear segregation, aging, and other phenomena. As a result, the quality of modified asphalt decreases [17–21], so it is necessary to adopt new technology, new technology, and interdisciplinary research on

polymer-modified asphalt blending systems. Xiong *et al.* [22] adopted a thermochemical mechanics method to efficiently transform polypropylene (PP) waste into maleated epoxidation degradation products through the hybridization of diisopropyl benzene peroxide (DCP), maleic anhydride (MAH), and epoxy soybean oil (ESO), which was used as warm mixed asphalt modifier (PPMs) to achieve better modification effects and enhanced properties. Wang *et al.* [22] abandoned the traditional shear method, and the modified asphalt prepared by the twin-screw shear method had better storage stability and low-temperature performance than the modified asphalt prepared by the traditional shear method. Loderer *et al.* [23] produced rubber particles with a coarser and larger surface area using high-pressure water jet technology, and crumb rubber-modified asphalt produced from such rubber particles has better low-temperature ductility.

Among many emerging technologies, ultrasonic processing offers the advantages of efficiency and cleanliness [24–26]. Studies have shown that the cavitation effect generated by ultrasound can enhance the stirring effect on the system and refine the polymer particles [27]. The research of ultrasonic in the field of asphalt and crude oil has also been widely used, and the high temperature and high-pressure environment generated by ultrasonic cavitation can change the position of weak bond energy in asphalt, thereby promoting the chemical reaction during the development of modified asphalt [28]. Many scholars have applied ultrasound to the research of asphalt and crude oil and studied the influence of ultrasound on it. Based on the effects of ultrasonic cavitation on asphaltene content, rheological properties, and metal content under different ultrasonic frequency and power input conditions, the results of Mohapatra and Kirpalani [29] show that under specific ultrasonic frequencies and powers, the strong attraction phase interaction between asphalt particles decreases, resulting in a decrease in asphalt viscosity, which improves the transportation performance of asphalt. Razavifar & Qajar [30] studied the effect of ultrasonic irradiation on the viscosity and thermal behavior of crude oil with high asphaltene content under different irradiation times and power/frequency, and the reduction in oil viscosity is even greater. Mousavi *et al.* [31] studied the effect of ultrasonic waves on crude oil and found that ultrasonic waves would decompose asphaltenes in crude oil, reducing the viscosity of asphalt and changing the rheology of asphalt. Based on the viscosity-temperature characteristics of asphalt, Wang *et al.* [32] analyzed the viscosity change trend of molten asphalt in the ultrasonic treatment test, the results show that the cyclic vibration and cavitation effect generated by

ultrasonic irradiation can effectively reduce the viscosity of asphalt, thereby enhancing the flow at high temperature.

Although ultrasonic technology has been applied in the field of asphalt research such as viscosity reduction and desulfurization, it is still difficult to apply ultrasonic in actual industrial production, Therefore, based on the modification process of stirring and ultrasound on asphalt, the combined effect of stirring and ultrasound on polymer-modified asphalt is numerically simulated, By analyzing the fluid motion state, velocity and pressure in the tank under the joint action of ultrasonic and mechanical stirring, the feasibility of ultrasonic and mechanical stirring on asphalt modification was studied. Through the parameters of the simulation model and the simulation results, the theoretical foundation for the further optimization of the ultrasonic stirring equipment of polymer-modified asphalt is laid.

NUMERICAL SIMULATION AND SIMULATION METHODS

Construction of the simulation domain

The tanks used in the study are cylindrical, and the agitator is a six-blade disc stirrer, as shown in Fig.1a. Deepen the tool head into the tank, and ensure that there is a certain distance between the agitator and the tool head. The CFD fluid calculation software is used for the numerical simulation of ultrasonic action on polymer-modified asphalt. During the simulation process, the model is simplified to a certain extent, and the multiple reference system method is used to establish the model. The simplified model diagram of the combination of various parts is shown in Fig.1b.
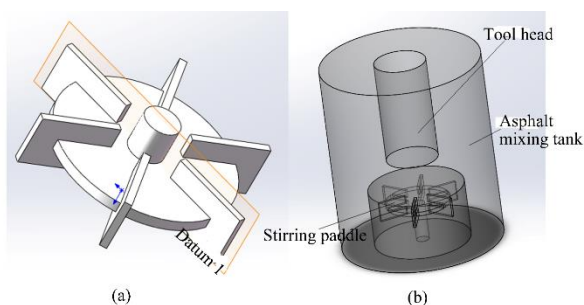
Figure 1. Simulation model: (a) six-blade disc stirrer, (b) simplified mixed tank model.

Construction of the numerical models

According to the three laws followed by fluid mechanics, the law of conservation of mass, momentum, and energy, mathematical models are established, namely continuity equation, momentum conservation equation, and energy conservation equation.

(1) Law of conservation of mass

According to the law of conservation of mass, the difference between the inflowing mass and the outflowing mass of the fluid microelement in unit time is equal to the increment of the fluid mass inside the fluid microelement. When the liquid is incompressible, i.e. the density is unchanged, its expression is as in Eq. 1:

$$\frac{\partial u}{\partial x} + \frac{\partial v}{\partial y} + \frac{\partial w}{\partial z} = 0 \tag{1}$$

where u, v, ω are the components of velocity vector u on x, y, z, respectively.

(2) The momentum equation

The momentum equation is also called the Navier-Stokes equation, which is expressed as the rate of change of the microelement fluid over time equal to the sum of all the forces acting on the microbody externally, and the equations for conservation of momentum in the three directions of three-dimensional space x, y, z are as follows:

$$\frac{\partial(\rho u)}{\partial t} + div(\rho uU) = div(u\,gradu) - \frac{\partial P}{\partial x} + S_u \tag{2}$$

$$\frac{\partial(\rho v)}{\partial t} + div(\rho vU) = div(u\,gradv) - \frac{\partial P}{\partial y} + S_v \tag{3}$$

$$\frac{\partial(\rho w)}{\partial t} + div(\rho wU) = div(u\,gradw) - \frac{\partial P}{\partial z} + S_w \tag{4}$$

Among them, the three relational expressions of S_u, S_v and S_ω, are as follows.

$$S_u = \frac{\partial}{\partial x}(\mu\frac{\partial u}{\partial x}) + \frac{\partial}{\partial y}(\mu\frac{\partial v}{\partial x}) + \frac{\partial}{\partial z}(\mu\frac{\partial w}{\partial x}) + \frac{\partial}{\partial x}(\lambda divU) \tag{5}$$

$$S_u = \frac{\partial}{\partial x}(\mu\frac{\partial u}{\partial x}) + \frac{\partial}{\partial y}(\mu\frac{\partial v}{\partial x}) + \frac{\partial}{\partial z}(\mu\frac{\partial w}{\partial x}) + \frac{\partial}{\partial x}(\lambda divU) \tag{6}$$

$$S_u = \frac{\partial}{\partial x}(\mu\frac{\partial u}{\partial x}) + \frac{\partial}{\partial y}(\mu\frac{\partial v}{\partial x}) + \frac{\partial}{\partial z}(\mu\frac{\partial w}{\partial x}) + \frac{\partial}{\partial x}(\lambda divU) \tag{7}$$

Where μ is the dynamic viscosity and λ is the second molecular viscosity.

(3) Law of conservation of energy

For the flow system in the tank, the law of energy conservation is satisfied. This definition can be described as the increase in energy in the microbody being equal to the sum of the net heat flux into the micro-body and the work done by physical and surface forces on the micro-body, and the expression is as follows.

$$\frac{\partial(\rho T)}{\partial t} + \nabla(\rho uT) = \nabla\left(\frac{k}{C_p} \cdot grad(T) + S_t\right) \tag{8}$$

3

FU *et al.*: NUMERICAL SIMULATION ON THE PROCESSING OF…

Chem. Ind. Chem. Eng. Q. 31 (1) 1−11 (2025)

where T is the temperature, k is the heat transfer coefficient of the fluid, C_p is the specific heat capacity, and S_t is the viscous dissipation term.

Grid division

The established model is imported into ICEM in STP format for meshing, in the process of meshing, the agitator and the nearby area and other areas are separated, the agitator and the nearby area are the moving areas, other areas are static areas, the liquid flow speed near the agitator is significantly higher than other areas, the flow field form is the most complex, therefore, it is divided by a structured grid, the grid of the moving area is refined, the grid of the static area can be slightly thicker, which can not only improve the calculation accuracy, but also shorten the calculation time, the grid quality requirement is higher than 0.6, and the number of grids is about 1.2 million.

Initial and boundary conditions

The fluid simulation is a simulation of liquid-gas mixing, the mixture model is adopted, the main phase is modified asphalt, the secondary phase is air, the wall of the tank with the tool head is the pressure outlet, and the air is allowed to enter and exit freely, and the wall model adopts the scalable wall function.

The wall thickness is set to 2 mm, and the temperature of the entire tank is set to 120 °C to ensure that the asphalt is in a liquid state. The density of the crumb rubber-modified asphalt used is 1.0 g/cm^3, and the viscosity is 1.2 Pa·s. The high-order differential solution format is selected for numerical calculation, and the iterative residual convergence accuracy is 1×10^{-6}. The reference pressure is the standard atmospheric pressure, the acceleration of gravity is 9.81 m/s^2, the direction is negative, the implicit separation algorithm is used, the wall surface adopts the no-slip wall boundary condition, the density-based solution method is adopted, the turbulence model selects the 1 model, and the speed-pressure coupling adopts the SIMPLE algorithm.

For the condition setting of ultrasonic cavitation, the end face of the tool head is the motion boundary. According to the working parameters of the ultrasonic generator, the displacement equation for setting the boundary of motion is Eq. 9.

$$x = A\sin(2\pi ft) \tag{9}$$

where A is the amplitude, and f is the frequency of the ultrasonic transducer.

By deriving it, the vibration velocity equation of the end face of the tool head is Eq. 10.

$$V = 2\pi f \times A \times \cos(2\pi ft) \tag{10}$$

Eq. 10 is compiled into a moving grid boundary by a user-defined functions (UDF) program.

Model validation

Due to the large difference between the frequency of ultrasonic vibration and the rotation speed of the agitator, the agitator was rotated first, and then the ultrasonic vibration simulation was performed. To check a good and appropriate setting of the boundary conditions, as well as the chosen computational mesh, a rough simulation was performed first. The speed of the agitator was set at 300rpm, the iteration time step was 0.01 s, and the iteration was 200 times, and the velocity field distribution in the tank was obtained, as shown in Fig.2. It can be seen from the figure that the velocity is large in the region close to the agitator, relatively small in the region far away from the agitator, and almost zero in the region close to the boundary of the tool head. The flow pattern generated by the six straight-blade turbine agitator is mainly radial flow. The radial flow generated by the rotation of the blades drives the crumb rubber-modified asphalt to flow to the edge of the tank. After the fluid hits the wall, it is divided into two parts, one part moves downward, and the other part moves upward, the fluid moving downward meets the lower wall flows to the stirring shaft, and then returns to the blade area. Due to the inhibition of the tool head, the fluid moving upwards only forms a backflow area between the tool head and the wall, while the liquid below the tool head has almost no fluid movement, and a dead zone will appear in this area. The dead zone does not exist at first, as the fluid continues to move until the motion area expands to cover the bottom surface of the tool head, the dead zone begins to appear, and then this area begins to expand until the fluid in the entire tank begins to move, the dead zone occupies the maximum area, and then iteratively enters the next cycle, and the dead zone area begins to decrease again. When the stirrer rotates to 2s, that is, the stirrer stirs 10 laps at this time, and reaches a steady state.
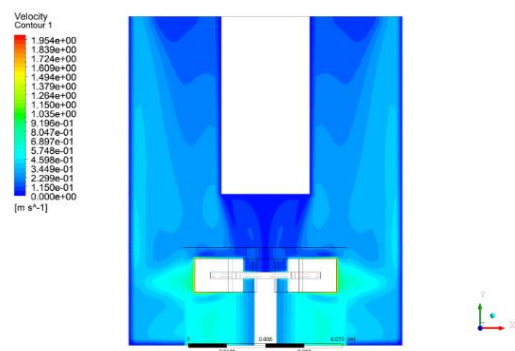
Figure 2. Distribution of velocity field in the tank when stirring for 2 s.

RESULTS AND DISCUSSION

Asphalt movement in the mixing tank

The amplitude of the tool head is 10 μm, the vibration frequency is 20 kHz, the time step is set to 1×10^{-7} s, and the iteration is 1500 steps, which is three cycles. Data is recorded every 10 steps, and a point is taken on the tool head, the speed of movement at this point is shown in Fig.3a. It can be seen that the tool head has no vibration in the first 200 steps, and the speed is 0. The agitator in the tank is given a rotating speed of 300 rpm, and under the action of the agitator, the modified asphalt starts to rotate around the axis. The modified asphalt gradually diffuses outward from the initial rotation, and at 2 s, the modified asphalt in the entire tank moves and forms a circulating field.

After adding the vibration and cavitation model of the tool head, the speed in the tank changes. According to the monitored speed, it can be seen that from step 240 to step 740 is a complete cycle. From 240 steps, the speed of the tool head gradually begins to increase, the tool head is in the lowest point position, and starts

the movement upwards, at this time, the modified asphalt under the tool head has a certain movement speed due to the compression of the tool head in the previous cycle, and the movement of the modified asphalt far away from the tool head has little effect, it is still dominated by stirring movement. Fig.3b shows the velocity of asphalt in the tank when iterating step 440. At this time, the velocity of the tool head reaches a maximum of 1.279 m/s, and the movement speed of the tool head gradually decreases when the iteration continues. When the tool head moves to the highest point, the speed decreases to 0. From then on, the tool head will move down to the lowest point, and start the next cycle of motion at the same time. This reciprocating motion forms high-frequency vibrations in the tool head. The main influence range of ultrasonic is near the end face of the tool head, and the movement of other areas is mainly affected by stirring, and the asphalt inside the tank can flow through the action of stirring, and then ultrasonic has an effect on the asphalt in the entire tank.

(a)   (b)
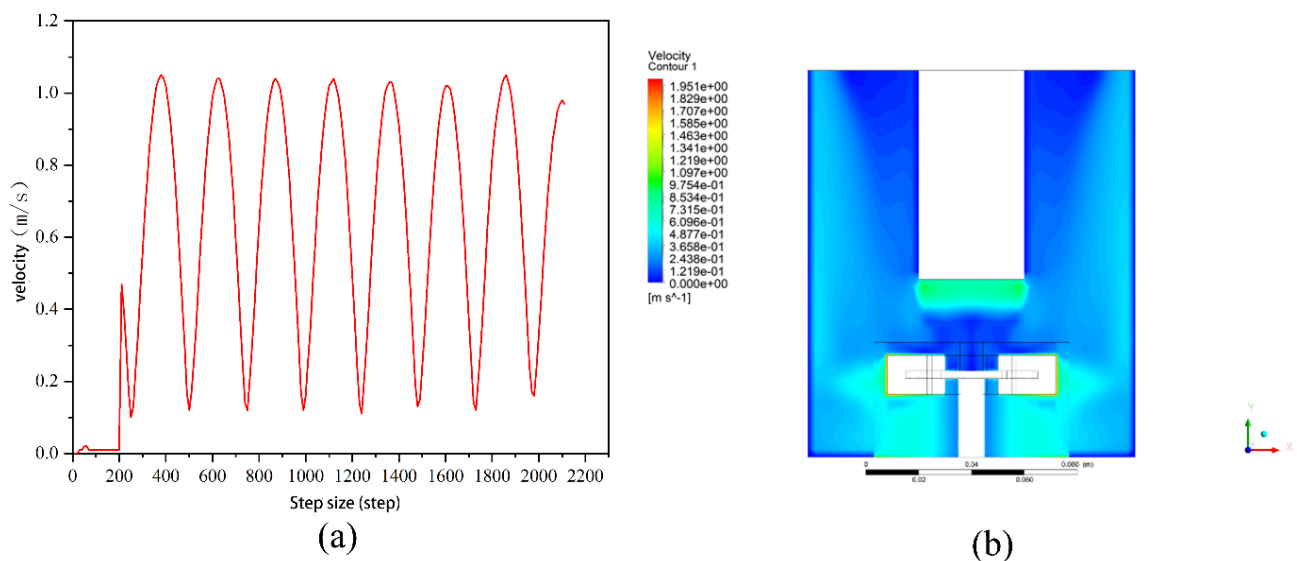
Figure 3. Motion distribution in the mixing tank: (a) The velocity of a point on the tool head, (b) The velocity field distribution in the tank at step 440 of iteration.

Pressure distribution in the mixing tank

First, the UDF-compiled program is loaded into the model, the cavitation model is closed, the agitator stops stirring, and the pressure change is observed to obtain the pressure cloud at high pressure as shown in Fig.4a. It can be seen from the figure that there is a high pressure under the tool head, which diffuses outward and gradually decreases. Under the action of ultrasound with an amplitude of 10 μm and a vibration frequency of 20 kHz, its application range is mainly in a small range under the tool head. When the same cycle changes, negative pressure will also occur at this

position, and negative pressure will make the internal pressure of asphalt lower than the saturated vapor pressure, and cavitation will occur under the action of alternating positive and negative pressure.

Under the action of mechanical vibration and cavitation of the tool head, the maximum value of the absolute pressure in the tank in three cycles changes with the iteration time as shown in Fig. 4b. It can be seen from the figure that the absolute pressure inside the container is positive. In the first 200 steps, there is only stirring in the tank. The maximum pressure in the asphalt is about 100kPa, which is the standard

(a)

(b)
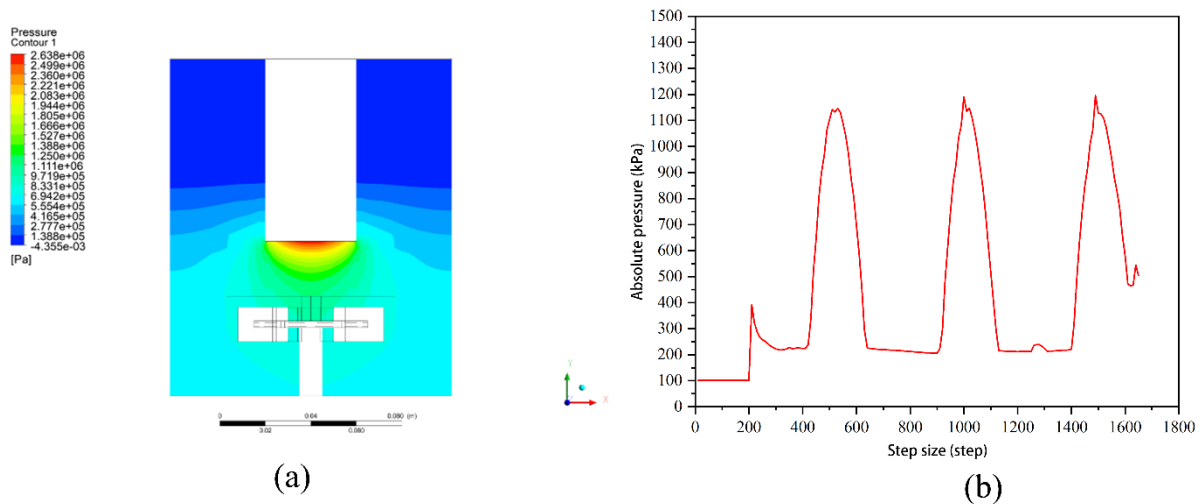
Figure 4. Pressure changes in the mixing tank: (a) Closing the cavitation model and stirring pressure cloud diagram, (b) The maximum absolute pressure change in the mixing tank.

atmospheric pressure. Cavitation does not occur. From step 200 to step 1700, the speed of the tool head presents a trend of sinusoidal motion, which conforms to the characteristics of the vibration cycle. The addition of ultrasonic vibration causes the fluid velocity to change, and under the effect of cavitation, the absolute pressure inside the liquid changes. After applying the ultrasonic vibration model from 2s, the sudden change in pressure from 100 kPa to 390 kPa is due to the change in speed. With the beginning of the iteration, the absolute pressure inside the liquid increases rapidly until it reaches the peak value of about 1100 kPa when the iteration reaches step 510, and then drops rapidly. When the iteration reaches step 640, the absolute pressure returns to 220 kPa, and the iteration continues, the maximum absolute pressure change presents a periodic change, which is consistent with the periodic characteristics of tool head vibration.

Starting from step 240, the absolute pressure diagram in the tank is taken every 50 steps until step 740, as shown in Fig.6. At step 240, the ultrasonic tool head is at the lowest point, and the absolute pressure is shown in Fig. 5a. At this time, the speed of the tool head is 0, and the overall absolute pressure in the tank is very low. The absolute pressure is close to 0 below the tool head, and the maximum pressure is caused by stirring, which is at the same level as the agitator and far from the tool head. At step 340, the tool head is close to the equilibrium position, and the absolute pressure is shown in Fig.5b. At this time, the absolute pressure in the tank does not change much, and the maximum absolute pressure is at the edge of the tool head. This is due to the different flow directions of the asphalt under the tool head and on the side, where the side asphalt rotates around the tool head, while the asphalt below the tool head moves up and down,

resulting in a relatively high pressure here. At step 440, as shown in Fig. 5c, the tool head has crossed the equilibrium position and is close to the highest point. At this time, the absolute pressure near the tool head changes, and the absolute pressure in the tank can reach a maximum of 550 kPa, its value rises significantly, and the absolute pressure changes greatly. At step 540, as shown in Fig. 5d, the absolute pressure at the tool head reaches 1140 kPa. At this time, the tool head moves from the highest point position to the equilibrium position, and the cavitation volume fraction generated at this time reaches near the first peak, and the cavitation intensity is large. The absolute pressure value under the tool head is stable at 1100 kPa from step 500 to step 560. At step 640, the absolute pressure is shown in Fig. 5e. The tool head has just crossed the equilibrium position and moved to the lowest position, and its value drops to 225 kPa, which is not much different from step 240 at the beginning of the above. The position under the tool head first weakens in the middle, then weakens on both sides. At this time, the cavitation intensity decreases, but it is the first inflection point of the gas fraction change, and then the gas fraction will gradually increase. At step 740, the absolute pressure is shown in Fig. 5f. The tool head has reached the lowest point, and the absolute pressure below the tool head returns to 220 kPa, which is the same as at step 240, indicating that the absolute pressure change conforms to the periodic law. Continue iterating to start the cycle of the next cycle. However, the pressure is not consistent away from the tool head, because the absolute pressure distribution is different due to the agitator rotation. To sum up, it can be seen that within a cycle, the increase of the absolute pressure change under the tool head mainly occurs between step 430 and 500, the peak absolute pressure is stable between step 500 and
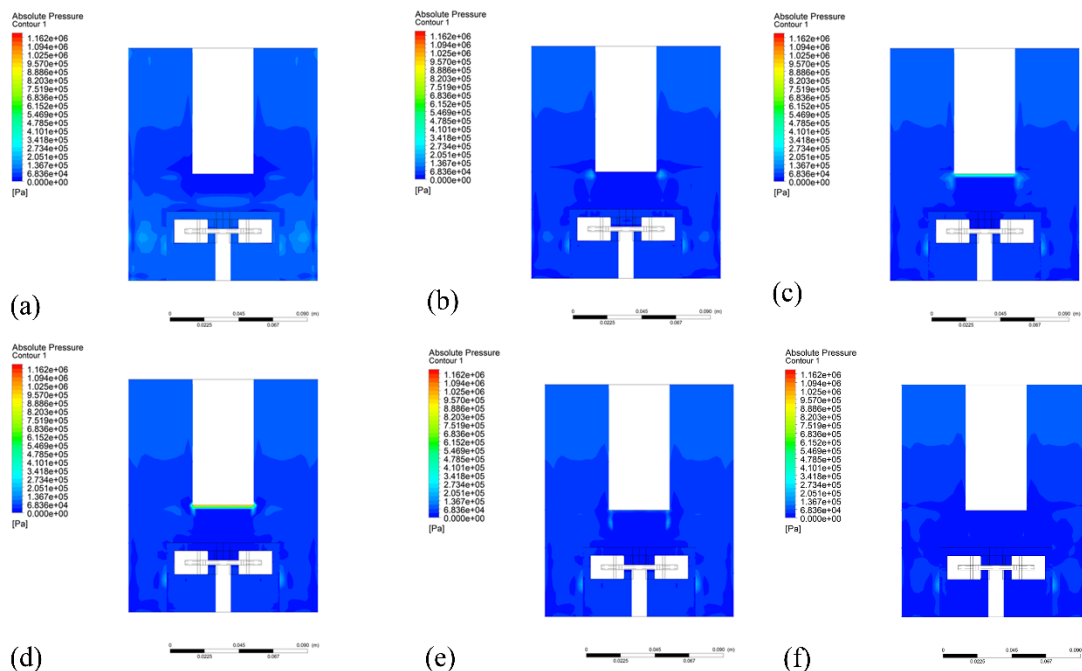
Figure 5. Pressure cloud diagram in mixing tank after iteration of different steps: (a) Iteration step 240, (b) Iteration step 340, (c) Iteration step 440, (d) Iteration step 540 (e), Iteration step 640, (f) Iteration step 740.

step 560, and the decrease occurs between step 560 and step 630. The absolute pressure changes are very small except under the tool head, so the position of ultrasonic cavitation is mainly directly under the tool head, and the cavitation area is small.

Change of gas volume fraction in the mixing tank

Taking the maximum volume fraction of cavitation bubbles in the tank as the research object, the maximum change of the volume fraction of cavitation bubbles in the tank is shown in Fig. 6a. Before step 200, the volume fraction of cavitation bubbles in the tank is 0, and there is only stirring in the tank during this time, so no cavitation occurs and no cavitation bubbles are generated. From step 200, the maximum volume fraction of cavitation bubbles in the tank began to increase, indicating that cavitation reactions began to occur. At step 470, the maximum volume fraction of cavitation bubbles reaches the first inflection point, at which time the cavitation bubble volume fraction is 0.36%, the cavitation intensity reaches the maximum in the first cycle, and then the volume fraction of cavitation bubbles begins to decrease. The second inflection point is reached at step 580 when the volume fraction is 0.29%, the cavitation intensity decreases slightly compared to before, and then the cavitation bubble volume fraction begins to rise again, starting the next cycle of changes. Comparing the volume fraction of cavitation bubbles in the three cycles, the volume fraction of cavitation bubbles in the latter cycle increases compared with the previous cycle, indicating that cavitation bubbles continue to increase under the

action of ultrasound, and the positive and negative pressures in each cycle continue to change, so that the cavitation bubbles have periodic growth, showing a trend of steady-state cavitation.

According to the distribution of cavitation bubbles in the cavitation process, the volume fraction of cavitation bubbles in the third cycle is the largest, that is, at step 1490, and the cavitation bubbles distribution in the tank is shown in Fig. 6b. It can be seen from the figure that the generation of cavitation bubbles is mainly concentrated directly below the tool head. The closer to the tool head, the larger the volume fraction of cavitation bubbles and the higher the cavitation intensity. However, the range of cavitation bubbles is very small, and the asphalt in the entire tank can be driven by stirring, and finally the asphalt in the entire tank is subjected to ultrasound.

Effect of viscosity on simulation results

Asphalt is a temperature-sensitive material when the temperature rises or falls, its viscosity changes greatly. Therefore, Therefore, the ultrasonic simulation of asphalt should pay attention to the influence of asphalt viscosity on the simulation results, and the ultrasonic cavitation intensity is reflected by the volume fraction of cavitation bubbles, so two more. The group control simulation is the ultrasonic cavitation simulation of crumb rubber modified asphalt with viscosities of 0.4 Pa·s and 0.8 Pa·s respectively. The points of volume fraction change of cavitation bubbles obtained by ultrasonic cavitation simulation of crumb rubber
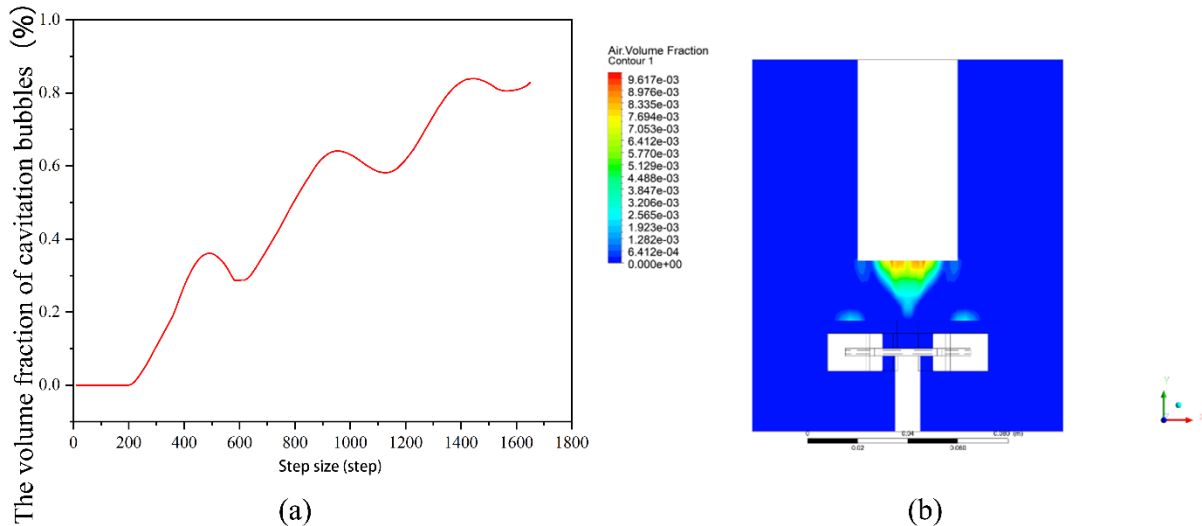
Figure 6. Variation of the volume fraction of cavitation bubbles in the stirring tank (a) Variation diagram of maximum volume fraction of cavitation bubbles in a stirred tank, (b) The Volume fraction distribution of cavitation bubbles in stirring tanks at step 1490 of iteration.

modified asphalt of three viscosities are shown in Fig.7. It can be seen from the figure that the volume fraction of cavitation bubbles in the three groups of experiments is constantly rising, and there is a process of rising first and then falling in a cycle, and the volume fraction of cavitation bubbles with viscosity of 0.4 Pa·s and 1.2 Pa·s is the same in these three cycles. From the beginning of step 200, the volume fraction of cavitation bubbles in the asphalt system with a viscosity of 0.8 Pa·s rises faster than the volume fraction of cavitation bubbles of the other two viscosity asphalt systems, but its cavitation bubble volume fraction also begins to decrease first, therefore, the cavitation bubbles volume fraction of the asphalt system with a viscosity of 0.8 Pa·s between 470 and 670 steps is lower. As the next cycle progresses, the cavitation bubbles volume fraction of the asphalt system with a viscosity of 0.8 Pa·s will increase again and continue to be higher than that of the other two viscosity asphalt systems, indicating that molten asphalt with a viscosity of 0.8 Pa·s is more conducive to ultrasonic cavitation in the process of ultrasonic powder modification of asphalt.

Influence of ultrasound on the stability of crumb rubber modified asphalt

Asphalt is often in a high-temperature state in the storage and transportation stage, so segregation at high temperatures will occur. To explore the influence of ultrasonic collaborative agitation on the storage of crumb rubber-modified asphalt, the storage stability of crumb rubber-modified asphalt was evaluated by simulating a segregation experiment to test the softening point and the difference between the upper and lower sections. Fig. 8 shows the softening point
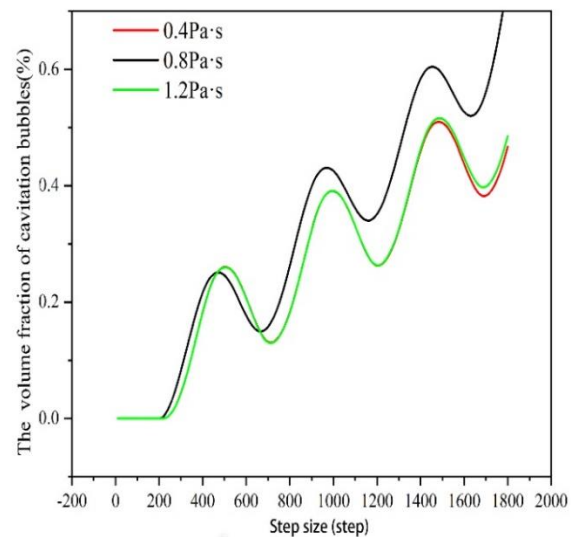
Figure 7. The change of volume fraction of cavitation bubbles at 5 mm below the tool head.

and difference ($\Delta T_{R\&B}$) of crumb rubber-modified asphalt under different control parameters (ultrasonic time is 0 min, 5 min, 10 min, 15 min, 20 min, 25 min) of the ultrasonic cooperative mixing process. It can be seen from the figure that the softening point difference of the upper and lower sections of crumb rubber modified asphalt prepared by ultrasonic collaborative stirring process is smaller than that of the upper and lower sections of crumb rubber modified asphalt prepared by pure stirring process, indicating that the collaborative process has a hindering effect on the segregation of crumb rubber. In Fig. 8, the two figures (a) and (b) are the microscopic morphology images taken by the Optical Super Depth-of-Field Microscope (OSM), where (a) is the crumb rubber modified asphalt prepared by only stirring process, and (b) is the crumb
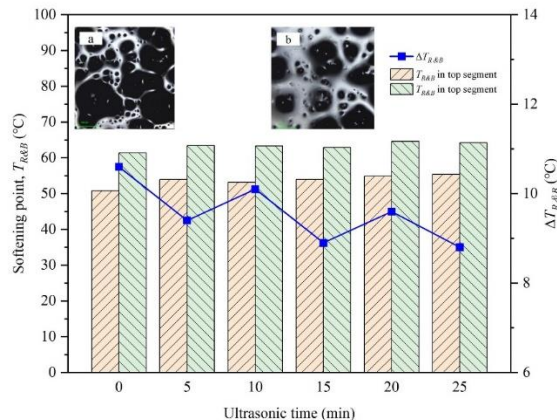
Figure 8. Segregation experimental results and OSM morphology of crumb rubber modified asphalt under different ultrasonic cooperative mixing process.

rubber modified asphalt prepared by the two processes of ultrasound for 5min and cooperative stirring. Comparing the two figures, it can be seen that after the addition of the ultrasonic process, the crumb rubber particles are more refined, indicating that this addition can slow down the agglomeration of crumb rubber.

CONCLUSION

With the assistance of ultrasound, the modified asphalt in the tank is more conducive to moving in the flow field, and its moving speed can reach up to 1.279 m/s within the reach of the tool head. Under the action of ultrasound, only positive pressure exists in the modified asphalt flow field after the application of the cavitation model, and the maximum absolute pressure can reach about 1200 kPa, and the change of absolute pressure conforms to the law of periodic motion. Cavitation bubbles are generated under the tool head, and the volume fraction of cavitation bubbles in the tank changes periodically with the change of ultrasound; with the increase of ultrasonic time, the gas content rate continues to rise, and the cavitation intensity increases. With the progress of ultrasound, the general trend of the volume fraction of cavitation bubbles in crumb rubber-modified asphalt systems with different viscosities is rising, but it is a process of rising first and then falling in a cycle. in the asphalt system with a viscosity of 0.8 Pa·s, the volume fraction of cavitation bubbles will continue to be higher than that of other viscosity asphalt systems. According to the experimental results, the ultrasound process can effectively inhibit the segregation of crumb rubber-modified asphalt and slow the agglomeration of crumb rubber modifier.

ACKNOWLEDGMENT

NOMENCLATURE

u, v, ω	the velocity components in the x-axis, y-axis, and z-axis of the spatial coordinate system are respectively, m/s
ρ	density, kg/m³
P	pressure, Pa
S_u, S_v, S_ω	momentum source components in 3 directions of the x, y, and z axes of the spatial coordinate system, N/m³
μ	dynamic viscosity, Pa·s
λ	second molecular viscosity, Pa·s
T	temperature, ℃
k	fluid heat transfer coefficient, kW/m²·℃
C_p	specific heat capacity, kJ/kg·℃
S_t	sticky dissipative items
x	displacement, m
A	amplitude, μm
f	frequency, Hz
t	time, s
V	velocity, m/s

REFERENCES

[1] M. Bueno, M.R. Kakar, Z. Refaa, J. Worlitschek, A. Stamatiou, M.N. Partl, Sci. Rep. 9 (2019) 20342. https://doi.org/10.1038/s41598-019-56808-x.

[2] F. Zhang, J.Y. Yu, Constr. Build. Mater. 24 (2010) 410–418. https://doi.org/10.1016/j.conbuildmat.2009.10.003.

[3] P.F. Liu, H.N. Xu, D.W. Wang, C.H. Wang, C. Schulze, M. Oeser, Constr. Build. Mater. 162 (2018) 765–780. https://doi.org/10.1016/j.conbuildmat.2017.12.082.

[4] M. Zaumanis, L.D. Poulikakos, M.N. Partl, Mater. Des. 141 (2018) 185–201. https://doi.org/10.1016/j.matdes.2017.12.035.

[5] E.A.A. Siddig, P.F. Cheng, Y.M. Li, Constr. Build. Mater. 169 (2018) 276–282. https://doi.org/10.1016/j.conbuildmat.2018.03.012.

[6] W.Q. Luo, J.C. Chen, Constr. Build. Mater. 25 (2011) 1830–1835. https://doi.org/10.1016/j.conbuildmat.2010.11.079.

[7] D. L. Presti. Construct. Build. Mater., 49 (2013) 863–881. https://doi.org/10.1016/j.conbuildmat.2013.09.007.

[8] T. Ma, H. Wang, L. He, Y.L. Zhao, X.M. Huang, J. Chen. Mater. Civ. Eng., 29 (2017) 04017036-1-10 https://doi.org/10.1061/(ASCE)MT.1943-5533.0001890.

[9] M. Ameri, A. Mansourian, A.H. Sheikhmotevali, Constr. Build. Mater. 40 (2013) 438–447. https://doi.org/10.1016/j.conbuildmat.2012.09.109.

[10] O.M. Xu, F.P. Xiao, S. Han, S.N. Amirkhanian, Z.J. Wang, Constr. Build. Mater. 112 (2016) 49–58. https://doi.org/10.1016/j.conbuildmat.2016.02.069.

[11] N.Y. Liu, K.Z. Yan, L.Y. You, M. Chen, Constr. Build. Mater. 189 (2018) 460–469. https://doi.org/10.1016/j.conbbuildmat.2018.08.206.

FU *et al*.: NUMERICAL SIMULATION ON THE PROCESSING OF…

Chem. Ind. Chem. Eng. Q. 31 (1) 1−11 (2025)

[12] Z.L. Jiang, C.B. Hu, S.M. Easa, X.Y. Zheng, Y. Zhang, J Appl. Polym. Sci. 134 (2017) 44850. https://doi.org/10.1002/app.44850.

[13] Z. Leng, R.K. Padhan, A. Sreeram, J. Cleaner Prod. 180 (2018) 682–688. https://doi.org/10.1016/j.jclepro.2018.01.171.

[14] X.H. Ding, L.C. Chen, T. Ma, H.X. Ma, L.H. Gu, T. Chen, Y. Ma, Constr. Build. Mater. 203 (2019) 682–688. https://doi.org/10.1016/j.conbuildmat.2019.01.114.

[15] J.Y. Hu, T. Ma, T. Yin, Y. Zhou, J. Cleaner Prod. 333 (2022) 130085. https://doi.org/10.1016/j.jclepro.2021.130085.

[16] Y.M. Li, R Ma, X.R. Wang, P.F. Cheng, Y.J. Chen. Case Stud. 20 (2024) e02820. https://doi.org/10.1016/j.cscm.2023.e02820.

[17] M.M. Phiri, M.J. Phiri, K. Formela, S.P. Hlangothi, Composites, Part B, 204 (2021) 108429. https://doi.org/10.1016/j.compositesb.2020.108429.

[18] L. Guo, C.S. Wang, D.J. Lv, D.H. Ren, T.J. Zhai, C.L. Sun, H.C. Liu, J. Cleaner Prod. 279 (2021) 123266. https://doi.org/10.1016/j.jclepro.2020.123266.

[19] F. Li, X. Zhang, L.B. Wang, R.X. Zhai, Constr. Build. Mater. 354 (2022) 129168. https://doi.org/10.1016/j.conbuildmat.2022.129168.

[20] P.P. Kong, X.H. Chen, G. Xu, W. Wei, Polym. Eng. Sci. 61 (2021) 2567–2575. https://doi.org/10.1002/pen.25783.

[21] X. Xiong, Y.M. Chu, Y. Luo, Y. H. Peng, N. N. Yang, J.M. Yan, X. Y. Chen, F. L. Zou, A. Sreeram. J. Cleaner Prod. 426 (2023) 139222. https://doi.org/10.1016/j.jclepro.2023.139222.

[22] J.R. Wang, Z.Q. Zhang, Z.L. Li, J. Mater. Civ. Eng. 32 (2019) 04019330. https://doi.org/10.1061/(ASCE)MT.1943-5533.0002971.

[23] C. Loderer, M.N. Partl, L.D. Poulikakos, Constr. Build.

Mater. 191 (2018) 1159–1171. https://doi.org/10.1016/j.conbuildmat.2018.10.046.

[24] D. Özçimen, M.Ö. Gülyurt, B. İnan, Chem. Ind. Chem. Eng. Q. 23 (2017) 367–375. https://doi.org/10.2298/CICEQ160306051O.

[25] A. Thakur, R.K. Gupta, V. Udhayabanu, D.R. Peshwe, Y.Y. Mahajan, Philos. Mag. Lett. 103 (2023) 2162617. https://doi.org/10.1080/09500839.2022.2162617.

[26] E. Malek, S. Bagherifard, O. Unal, A. Jam, S. Shao, M. Guagliano, N. Shamsaei, Surf. Coat. Technol. 463 (2023) 129512. https://doi.org/10.1016/j.surfcoat.2023.129512.

[27] F. Liang, J. Fan, Y.H. Guo, M.H. Fan, J.J. Wang, H.Q. Yang, Ind. Eng. Chem. Res. 47 (2008) 8550–8554. https://doi.org/10.1021/ie8003946.

[28] H.T. Kim, H. Shin, I.Y. Jeon, M. Yousaf, J. Baik, H.W. Cheong, N. Park, J.B. Baek, T.H. Kwon, Adv. Mater. 29 (2017) 1702747. https://doi.org/10.1002/adma.201702747.

[29] D.P. Mohapatra, D.M. Kirpalani, Appl. Petrochem. Res. 6 (2016) 107–115. https://doi.org/10.1007/s13203-016-0146-1.

[30] M. Razavifar, J. Qajar, Chem. Eng. Process.153 (2020) 107964. https://doi.org/10.1016/j.cep.2020.107964.

[31] S.M. Mousavi, A. Ramazani, I. Najafi, S.M. Davachi, Petrol. Sci. 9 (2012) 82–88. https://doi.org/10.1007/s12182-012-0186-9.

[32] L.M. Wang, Z.K. Song, C. Gong, Case. Stud. Constr. Mat. 16 (2022) e01012. https://doi.org/10.1016/j.cscm.2022.e01012.

GANG FU[1]

RUIEN YU[1,2]

XIAOLIN YU[1]

XIAOHAN LI[1]

XIAOWEN CHEN[3]

XIAOYAN ZHANG[2]

YANFEI KOU[1]

XIJING ZHU[1]

[1]Shanxi Key Laboratory of Advanced Manufacturing Technology, North University of China, Taiyuan, China

[2]Shanxi Transportation Technology Research & Development Co., Ltd, Taiyuan, China

[3]State Key Laboratory of Special Functional Waterproof Materials, Beijing Oriental Yuhong Waterproof Technology Co., Ltd, Beijing, China

NUMERIČKA SIMULACIJA OBRADE GUMOM MODIFIKOVANOG ASFALTA ULTRAZVUKOM I MEHANIČKIM MEŠANJEM

Na osnovu postojeće modifikovane opreme za proizvodnju asfalta, ultrazvučni uređaj je integrisan u postojeću tehnologiju disperzije mešanja, a softver FLUENT za simulacija strujanja fluida se koristi za kombinovanje dejstva ultrazvuka i mešanja. Mešanje i ultrazvučn efekat, dva oblika kretanja, realizovana su korak po korak, a simulirana su stanja kretanja asfalta modifikovanog gumom u interakciji ultrazvučnog i mešanja, što je dalo novu metodu za istraživanje opreme za proizvodnju asfalta modifikovanog gumom. Rezultati pokazuju da pod dejstvom ultrazvuka u modifikovanom polju strujanja asfalta nakon dodavanja modela kavitacije postoji samo pozitivan pritisak, a maksimalni apsolutni pritisak može da dostigne oko 1200 kPa. Sa povećanjem trajanja ultrazvučnog efekta, količina vazduha ispod glave alata se periodično i redovno menja i postepeno će se povećavati, broj kavitacionih mehurića će nastaviti da raste, a intenzitet kavitacije će se povećati. Proučavan je uticaj viskoziteta asfalta na zapreminski udeo kavitacionih mehurića. Viskoznost sistema od 0,8 Pa·s, pogodniji je za pojavu kavitacije, Proces ultrazvučnog sinergističkog mešanja pogoduje inhibiciji fenomena segregacije. od gumom modifikovanog asfalta..

Ključne reči: ultrazvuk; kavitacija; asfalt modifikovan gumom u mrvicama; mehaničko mešanje; CFD simulacija.

NABILA BOUCHERIT[1]
SALAH HANINI[1]
ABDELLAH IBRIR[2]
MAAMAR LAIDI[1]
MOHAMED ROUBEHIE FISSA[1]

[1]Biomaterials and Transport Phenomena Laboratory (LBMPT), Yahia Fares University, Medea, Algeria

[2]Materials and Environment Laboratory (LME), Faculty of Technology, Yahia Fares University, Medea, Algeria

PREDICTION OF DOXYCYCLINE REMOVAL BY PHOTO-FENTON PROCESS USING AN ARTIFICIAL NEURAL NETWORK - MULTILAYER PERCEPTRON MODEL

Article Highlights
- Hydroxyl radicals transform efficiently doxycycline hyclate from an aqueous solution
- Experimental optimization showing strongly effect of pH, the concentration of DXC, H_2O_2, and Fe^{2+}
- Designed OANN presents a very good correlation between experimental and predicts removal efficiency

Abstract

This paper presents a study on the effectiveness of the Photo-Fenton Process (PF) for removing the doxycycline hyclate (DXC) antibiotic. The experiment showed that the best removal efficiency was achieved (79%) at pH 3 for 2.5 mg/L of DXC, 76.53 mg/L of H_2O_2, and 86.8 mg/L of Fe^{2+}. The degradation mechanism of DXC by hydroxyl radicals was confirmed by FTIR and HPLC. To model the oxidation reaction of DXC by PF, a multilayer perceptron (MLP) based optimized artificial neural network (OANN) was used, taking into account experimental data such as pH and initial concentrations of DXC, H_2O_2, and Fe^{2+}. The OANN predicted removal efficiency results were in close agreement with experimental results, with an RMSE of 0.0661 and an R^2 value of 0.99998. The sensitivity analysis revealed that all studied inputs significantly impacted the transformation of DXC.

Keywords: doxycycline hydrate; modelling; photo-fenton; optimized artificial neural network; removal.

Currently, the production or even the consummation of antibiotics has become more and more increasing, this has caused their presence continuously in liquid effluents and even in soils either as original or in metabolic forms [1]. It has been reported that tetracycline antibiotics are the second class of antibiotics produced and used throughout the world, they were used mainly in veterinary and human therapy as well as feed additives for animals. However,

the existence of tetracycline (TC) in wastewater can influence the quality of surface water, groundwater, soils, aquaculture, animals, and humans [2]. However, TC molecules have a typical structure like naphthalene resisting degradation and metabolic reactions, then, they are released into the environment in their original structure. Therefore, exposure to TC, for example in drinking or irrigation water, can cause potential damage to living organisms and the environment. Moreover, TC can cause microorganisms to develop resistance to drugs by producing antibiotic-resistance genes and inducing human and animal metabolism [3]. It has been revealed that TC can reduce the growing functions of teeth and skeleton of fetuses and children thus estrogenic effects [4]. Also, TC antibiotics pose severe threats to the development and metabolism of plants, by inhibiting biomass accumulation, decreasing pigment content, and increasing reactive oxygen species and antioxidant enzymes [5]. Doxycycline

(DXC) in its hyclate form is a semi-synthetic tetracycline molecule, it has a large activity spectrum against Gram-positive and Gram-negative bacteria which is widely used in human and veterinary practice [1,6]. As a result, DXC can be detected as it is in livestock, fish, vegetables, fruits, and in different sources of water, wastewater, and soil [6]. Recently, Advanced Oxidation Processes (AOPs) have generated hydroxyl radicals which are very reactive and no selective oxidant for a great variety of organic compounds. These radicals can be generated from some oxidizing reactants like hydrogen peroxide or ozone combined with the presence of metallic or semiconductor catalysts within or without energy [7].

The PF oxidation is a metal-catalyzed oxidation reaction occurring in the presence of iron through a chain of radical reactions which allows the generation of hydroxyl radicals (Eq. 1). In addition, the association of hydrogen peroxide/ferrous ions with UV radiation enhances the efficiency of oxidation process especially the rate of degradation of organic pollutants by additional generation of hydroxyl radicals from different reactions [8].

In the Fenton reaction, ferric ions may accumulate and the reaction and the reaction chain do not continue if the ferrous ions are completely consumed [9]. Thus, ferric ions catalyze the decomposition of hydrogen peroxide (Eqs. 2 and 3) [8].

$$H_2O_2 + Fe^{2+} + H^+ \rightarrow HO^{\bullet} + H_2O + Fe^{3+} \tag{1}$$

$$H_2O_2 + Fe^{3+} \rightarrow H^+ + HO_2^{\bullet} + H^+ \tag{2}$$

$$HO_2^{\bullet} + Fe^{3+} \rightarrow H^+ + O_2 + Fe^{2+} \tag{3}$$
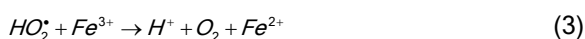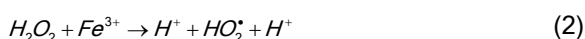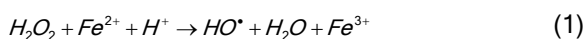
As shown in Eqs. (4) and (5), consumption of hydroxyl radicals may occur which leads to the reduction of Fenton process efficiency [8].

$$HO^{\bullet} + Fe^{2+} \rightarrow Fe^{3+} + HO^- \tag{4}$$

$$HO^{\bullet} + H_2O_2 \rightarrow H_2O + HO_2^{\bullet} \tag{5}$$

In the presence of UV radiation, $HO^{\bullet}$ was formed by the reduction of Fe^{3+} into Fe^{2+} (Eq. 6), decomposition of H_2O_2 into two molecules of $HO^{\bullet}$ (Eq. 7), and photolysis of ferric complexes produced during the reaction chain process (Eq. 8) [7].

$$Fe^{3+} + H_2O + hv \rightarrow Fe^{2+} + HO^{\bullet} + H^+ \tag{6}$$

$$H_2O_2 + hv \rightarrow 2HO^{\bullet} \ (if \ \lambda \leq 400 \ nm) \tag{7}$$

$$Fe(OH)^{2+} + hv \rightarrow Fe^{2+} + HO^{\bullet} \tag{8}$$
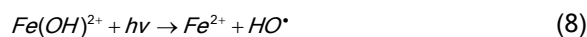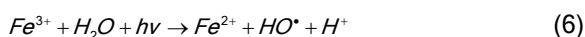
Photo-Fenton process as homogeneous an AOP has been considered a potentially effective process allowing the removal and mineralization of the majority of non-biodegradable and recalcitrant micro-pollutants such as tetracycline molecules [6]. In addition, due to its simplicity, the PF process is recognized by a low cost, fast reaction rate and no amount of sludge can be produced [7]. It has been reported that the oxidative mechanism pathway of DXC by hydroxyl radicals has been proposed by several studies, which can lead to small molecules and/or complete mineralization [1,6]. Likewise, Fenton oxidation, the number, and complexity of the reactions that can take place during PF oxidation, on the one hand, and since the intervention of several parameters in the efficiency of the elimination process, statistical modeling methods are unable to predict or to simulate effectively oxidation by hydroxyl radicals, Artificial neural network (ANN) methods has attracted attention researchers to simulate, model and predict all type of phenomena in various discipline of sciences and engineering. Many studies proved the capacity and rapidity of these methods to solve numerous problems of environmental engineering, such as the adsorption of organic pollutantsm [10], membrane separation [11], and biological treatment [12]. Nevertheless, it has been reported that in the last decade, the application of ANN has been increasingly applied in AOPs especially for dye removal [13], but a few researches have been carried out on the application of ANN in PF processes for the removal of antibiotics compounds [14]. In their work, Talwar *et al.* [15] and Sethi *et.al* [16], studied the transformation of different molecules with therapeutic effects such as amoxicillin, and metronidazole by photocatalytic methods which are more expensive and applied modeling based on the combination of several artificial intelligence methods, this and despite the effectiveness of the methodology applied, makes the procedure. However, the application of neural modeling in the present study is since it is simple and rapid and has proven its effectiveness in several areas. in addition, it has not previously been applied to the transformation of the DXC molecule by the photo-Fenton process.

The present work focuses on assessing the effectiveness of the H_2O_2/Fe^{+2}/solar irradiation system to remove doxycycline hyclate from an aqueous solution by experimental and modeling study. To achieve this objective, four variables were targeted: pH, doxycycline, hydrogen peroxide, and catalysis concentration. The performance of the optimized ANN model was conducted by evaluating the predicted in contrast to experimental removal efficiency. Finally, the

impact and the importance of each input variable on removal efficiency as the output variable was determined.
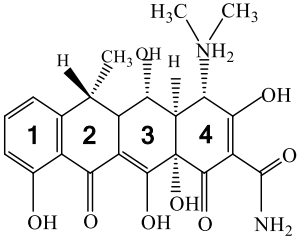
MATERIAL AND METHODS

Materials

Doxycycline hyclate (DXC) was provided by the Antibiotical-Saidal pharmaceutical group (Medea, Algeria). The chemical structure and physico-chemical properties are shown in Table 1. Hydrogen peroxide solution (30%, w/w) and salt of iron in the form of ferrous sulfate heptahydrate ($FeSO_4 \cdot 7H_2O$) were purchased from Sigma-Aldrich Corporation (St. Louis, MO, USA) and all other chemicals were of analytical grade and were used without further purification.

Table 1. Physicochemical properties of doxycycline hyclate.

Chemical structure	Characteristic	Value
	Molecular Weight (g/mol)	1025.87
	Water solubility (293°K, mg/mL)	50
	Appearance	yellow crystalline powder
	Purity (%)	98.5
	λ_{max}(nm)	375
	$pk_{a1}^{a2,a3}$	7.07, 9.13, 3.50

Methods

The PF oxidation is a metal-catalyzed oxidation reaction occurring in the presence of iron through a chain of radical reactions which allows the generation of hydroxyl radicals (Eq. 1). In addition, the association of hydrogen peroxide/ferrous ions with UV radiation enhances the efficiency of oxidation process especially the rate of degradation of organic pollutants by additional generation of hydroxyl radicals from different reactions [8].

Experiments were carried out in a borosilicate reactor (0.1 L) menu with a water jacket maintaining a constant temperature (24 ± 2 °C). The radiation was provided from solar irradiation with light intensity and luminance varying from 450 to 600 W/m^2 and 95 to 100 klx, respectively. A volume of 50 mL of reaction mixture containing an appropriate concentration of DXC and hydrogen peroxide was illuminated by solar radiation under magnetic stirring. After, ferrous ions (as ferrous sulfate heptahydrate) were added and the mixture was stirred magnetically for 30 min (Fig. 1). The pH effect was investigated by using different buffer solutions: 20 mM potassium chloride/HCl buffer (pH 2 and 2.5), 20 mM potassium phthalate/HCl buffer (pH 3, 3.5 and 4), and 20 mM potassium phthalate/NaOH buffer (pH 4.5 and 5). The parameters taken in this study, on which removal of DXC depends, are pH, initial concentration of DXC, H_2O_2, and Fe^{2+} (Table 2).
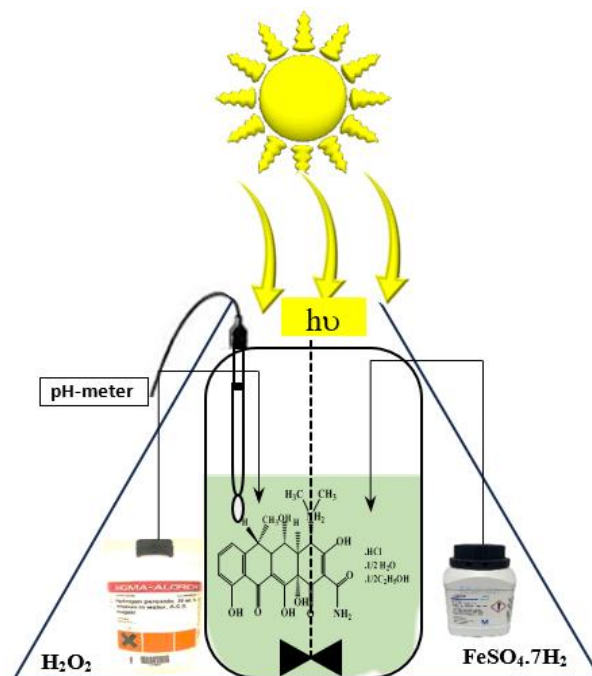
Figure 1. Schematic representation of photo-Fenton reaction of DXC.

In the end, the mixture was centrifuged at 4.000 rpm for 10 min and the supernatant and the precipitates were monitored for spectroscopies, chromatography,

BOUCHERIT *et al*.: PREDICTION OF DOXYCYCLINE REMOVAL …

Chem. Ind. Chem. Eng. Q. 31 (1) 13–21 (2025)

and toxicity analysis. The experiments were conducted in triplicate and their average were reported.

Table 2. Variables and their levels.

Level N°	pH	[DXC]$_0$ (mg/L)	[H$_2$O$_2$]$_0$ (mg/L)	[Fe^{2+}]$_0$ (mg/L)
1	2	0.50	8.5035	2.8
2	2.5	1.50	25.510	19.6
3	3	2.50	42.5175	36.4
4	3.5	3.50	60.0245	53.2
5	4	4.50	76.5315	70
6	4.5	5.50	93.5385	86.8
7	5	6.50	110.5455	103.6

Characterization methods

The DXC concentration was determined with a UV-visible spectrophotometer (Model Perkin-Elmer 550 A) at different wavelengths ranging from 200 to 600 nm. The residual DXC concentration after treatment with PF oxidation was evaluated on the supernatant at the maximum wavelength of DXC (375 nm). The removal efficiency (RE) was calculated as follows (Eq. 9) [17]:

$$Re(\%) = \frac{C_0 - C_t}{C_0} \cdot 100 \qquad (9)$$

where, C_0 and C_t (mg/L) are the initial DXC concentration and its concentration at time (t) respectively.

FTIR spectra of dried DXC and its precipitate degradation products have been recorded for the KBr pellet. FTIR spectra were done in the mid-IR region of 400–4000 cm^{-1} and were collected at the absorbance mode in a Shimadzu 8400 spectrophotometer at 4 cm^{-1} resolution and a number of scans of 128. A High-Performance Liquid Chromatography (Alliance Waters e2695) equipped with a UV-Visible detector (Waters 2489) operated at 280 nm ± 4nm, an automatic sample injector, a 3DR solvent delivery system, a thermos-stated column compartment adjusted at 60 °C and a stationary phase constituted by a Reverse-Phase column (RP18, 4.6 mm x 25 cm), is used to get the elution data of DXC and its extracted degradation products. The elution process was carried out using a mobile phase made up of the reagent cited in Table 3. The flow rate is to 1 mL/min. The injection volume was 20 μL which was conducted with an automatic injector.

Artificial neural network modeling

Artificial neural networks (ANN) are mathematical models, which have similar principles and share basic elements with the nervous system to take actions based on perception rather than reasoning. Modeling consists of implementing a system of neural networks in an artificial mode, to set correspondence for each composing the biological neuron (Figure 2).

Table 3. Mobile phase composition.

Reagent	Monobasic phosphate potassium	Sodium hydroxide	Tetrabutyl-ammonium-hydrogen sulfate	Edetate disodium	Tertiary butyl alcohol
g	2.72	0.74	0.50	0.40	60
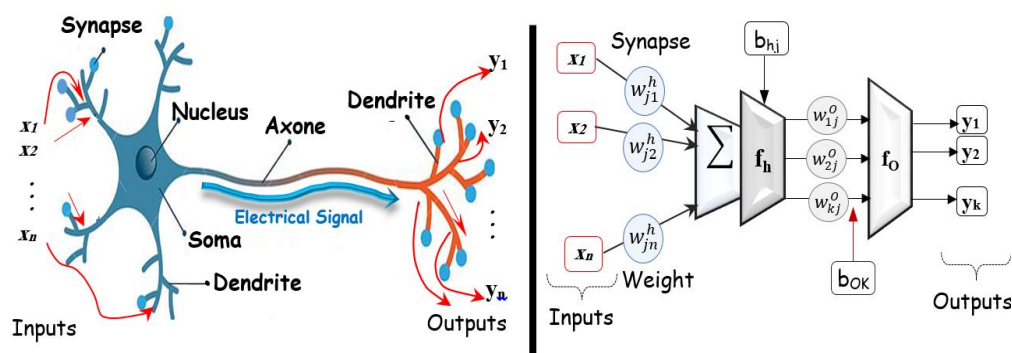
Figure 2. Schematic representation of the similarity between biological neuron and an ANN.

In the present study, the adopted methodology for the removal efficiency prediction of DXC by the neuronal technique can be summarized into four steps: selection of neural model inputs, data collection, data division sets, and data normalization. The input variables for the feed-forward neural network are pH, initial DXC concentration (mg/L), initial H$_2$O$_2$ concentration (mg/L), and initial Fe^{+2} concentration. The output variable selected was removal efficiency. Table 4 contains the statistical analysis of the inputs

and output data which are expressed by minimum, mean, maximum, and standard deviation.

Table 4. Statistical analysis of inputs and output data.

	Min	Mean	Max	STD
pH	2	3.0637	5	0.3256
$[DXC]_0$ (mg/L)	0.5000	2.7614	6.5000	1.0219
$[H_2O_2]_0$ (mg/L)	8.5161	61.1409	110.8700	23.2844
$[Fe^{2+}]_0$ (mg/L)	2.7814	67.0639	103.9130	29.4269
RE (%)	9.7435	63.7960	80.2030	13.2515

The total experimental database was divided into three subsets: training (67%), testing (17%), and validation (16%). Since there is a difference within the input data ranges, a normalization is essential, all input and output data were converted into normalized values in the -1 and +1 range using Eq. (10) expressed as follows:

$$y_n = \frac{2(y - y_{min})}{(y_{max} - y_{min})} - 1 \tag{10}$$

where, y_n is the input or output variable y, and y_{min} and y_{max} are the minimum and maximum values of variable y, respectively.

Figure 3 details the design principle of the ANN model in this study.

To optimize the topology of the network architecture, it was necessary to determine the optimum number of hidden neurons, in which some statistical parameters such as R^2, MSE, RMSE, and MAE, could calculate for the training process.
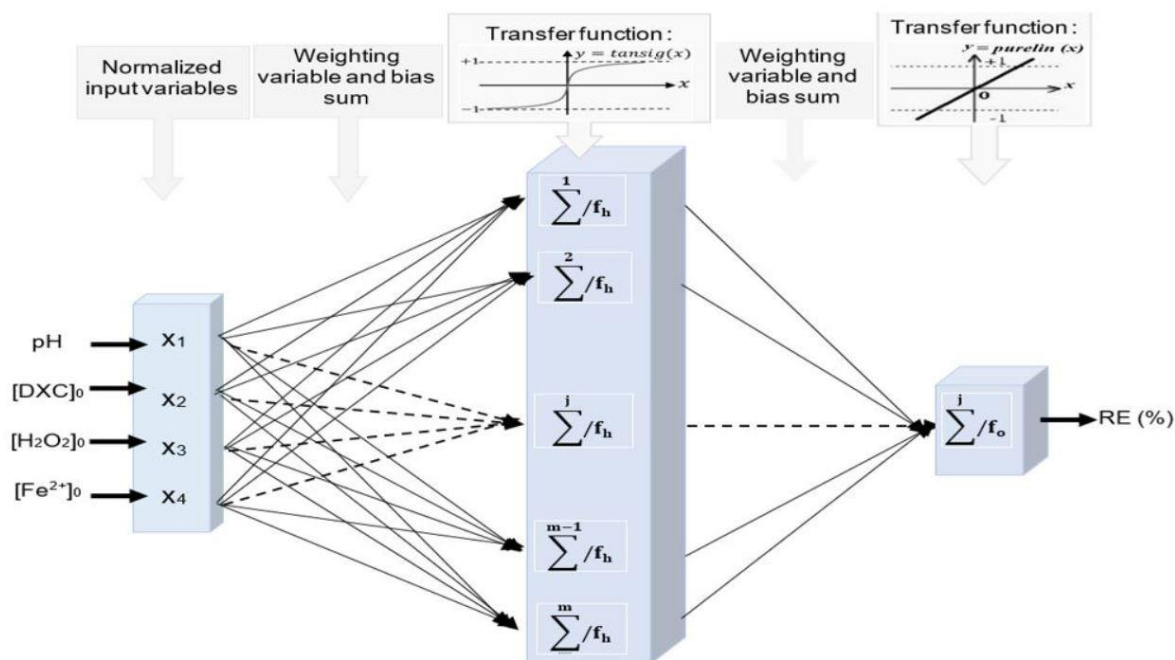
Figure 3. Architecture of the ANN-MLP model.

RESULTS AND DISCUSSION

Effect of pH, DXC, Hydrogen peroxide, and ferrous ions doses

It has been demonstrated that common operating parameters affecting efficiency removal in terms of quality and quantity in all Fenton processes are: pH, organics, oxidant, and catalysis concentrations [7]. The pH of the reaction medium affects strongly the production of hydroxyl radicals. However, the photolysis process of hydrogen peroxide is independent of the pH condition. Therefore, it has been reported that PF oxidation can remove organic pollutants in neutral and acidic mediums [8]. Therefore, according to Figure 4, at high acidity (pH < 3), the removal efficiency of DXC is very low (about 40%), this can be explained by the slowing down of the Fenton reaction due to the stability of hydrogen peroxide at acidic pH which reacts with protons to form oxonium ions (Eq. 11). Moreover, the excess of H^+ could acting as scavenger of hydroxyl radicals as shown in Eq.(12) [8].

$$H_2O_2 + H^+ \rightarrow H_3O_2^+ \tag{11}$$

$$HO^\bullet + H^+ + e^- \rightarrow H_2O \tag{12}$$

Therefore, at low acidity (pH ≥ 4), the process of photo-oxidation using ferrous ions favors the formation of hydroxyl ions as hydroxyl radicals (Eq.13) which precipitate with iron ions under complex species. Also, the auto decomposition of hydrogen peroxide is

accelerated at higher pH, this must reduce the activity of the Fenton reagent [18].

$$Fe^{2+} + HO^\bullet \rightarrow Fe^{3+} + HO^- \qquad (13)$$

At pH 3, it was observed that the maximum of the RE of DXC was achieved (67.074%), for which the hydroxy-ferric complexes are more soluble and the $Fe(OH)^{2+}$ ions are more photoactive [18]. Therefore, another chief systematic parameter assessing the performance of FP treatment is the micropollutant concentration in the contaminated effluent. The influence of this parameter was studied for DXC ranging from 0.5 to 6.5 mg/L, at pH 3 and for doses of H_2O_2 and Fe^{2+} of 60.0245 mg/L and 86.8 mg/L, respectively. It is shown in Figure 4 that an oxidation potential was observed under these conditions. Nevertheless, the curve allure shows clearly that for DXC concentrations varying from 0.5 to 2.5 mg/L, Whereas, it has been reported that removal efficiency by PF oxidation, increases with an increase in H_2O_2 dose until optimum concentration [8]. However, results depicted in Figure 4 showed that from a concentration of H_2O_2 of 76.53 mg/L up to 110.54 mg/L, the RE decreases slightly. First, the amount of H_2O_2 was consumed following the ratios of Fe^{2+}/H_2O_2 and H_2O_2/UV reactions. This led to the remarkable removal of organic pollutants by the hydroxyl radicals thus formed. Therefore, as reported in the literature, in the PF process, the excessive H_2O_2 improves the scavenging of $HO^\bullet$ which strongly reduces removal efficiency [7]. In our case, this phenomenon was limited by the photolysis reaction of hydrogen peroxide. Also, regarding Figure 3, the results indicate that the DXC removal has a slower character without ferrous dosage (i.e) H_2O_2/UV process (RE = 17.87%), whereas, the PF process occurs rather faster for ferrous doses of 2.8 mg/L (RE = 43.22%). Moreover, since the ferrous dosages increase from 2.8 to 36.54mg/L, the RE achieves 70.95% which is due to the increasing generation of hydroxyl radicals from the Fenton reaction plus the chemical reduction of hydroxyl-ferric. It has been reported that an increase in ferrous dosage in PF oxidation changes the final pH of the solution from 3.5 to 4.4, thus leading to the formation of iron oxyhydroxide which precipitates and then reduces penetration of light throughout the solution [19].

UV-visible spectra, FTIR, and HPLC analysis of the DXC treated by PF process

As indicated in Figure 5a, the spectrum of DXC contains three main absorption bands, two were located in the UV region at 245 and 275 nm, and the third in the visible region at 375 nm. For the treated solution spectrum, it was shown that the three absorption bands were strongly reduced after PF treatment. This suggests that the chromophore and the auxhochrome groups were converted as well as related auxochrome groups to an aromatic ring [20]. this is likely due to the formation of new aromatic intermediates or other products. 15, 43. However, since •OH is involved in a non-selective reaction by acting on the breakdown of functional groups and hydroxylation of the aromatic structure of tetracyclines, which consequently results in the formation of smaller organic molecules [21]. Pulicharla *et al.* [21] proposed a reaction mechanism of chlortetracycline (TC molecule) by Fenton oxidation. They suggested that hydroxyl radicals are disposed to act on carbon-dimethyl amino and carbon-carboxyl amide groups.
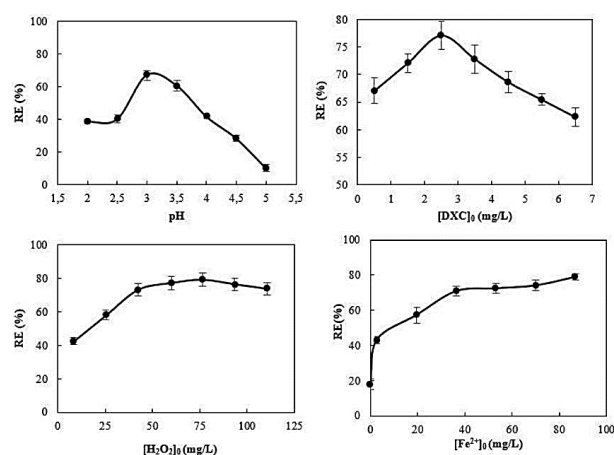
Figure 4. Effect of pH and concentration of DXC, H_2O_2, and Fe^{2+} on RE by PFP.
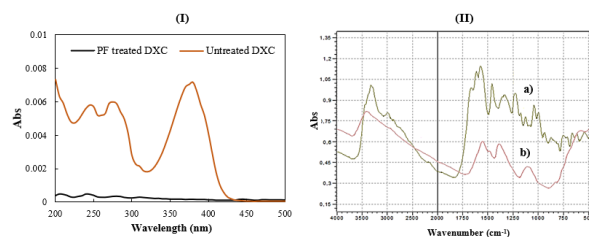
Figure 5. (I) UV-visible spectra of CTC before and after photo-Fenton treatment, and (II) FTIR of a) CTC, and b) its transformed products.

As a result, the formation of tricyclic and bicyclic aromatic intermediate compounds leads to smaller organic molecules. Hence, Bolobajev *et al.* [6] have depicted a complete mineralization of DXC by auto-degradation involving $Fe^{3+}/H_2O_2/UV$-C which is very promising by reduction of ferric ions to ferrous ions as well as DXC- Fe^{3+} complex formation leading to a reductive release of Fe(II) while ensuring the generation of $HO^\bullet$ by photolysis and photo-reduction.

Besides, as shown in Figure 5b, for FTIR spectra

of the original DXC sample and its degradation products, the transformation of the parent molecule by PF oxidation was achieved. The FTIR spectrum of the metabolite product as precipitate showed a significant reduction in the number and band absorption compared to the untreated molecule spectrum. The absence of the different characteristics of stretching bands confirms that the functional groups may be transformed by hydroxyl radicals. New position bands of -C=C- of the aromatic ring group appeared at 1450 and 1550 cm⁻¹, this may be due to a bathochromic effect of new substituted groups. In addition, a transformation of DXC by hydroxyl radicals generated by PF reaction was performed by its HPLC chromatograms. The chromatogram of the DXC original solution (Figure 6a) revealed a single peak having a retention time equal to 22.15 min. Nevertheless, the disappearance of the peak corresponding to the DXC molecule can be seen in the chromatogram of extracted degradation products (Figure 6b), whereas a new peak takes place at a retention time equal to 4.941 min. This must confirm the transformation of functional polar groups of DXC molecules by hydroxyl radicals as well as the formation of new molecules.
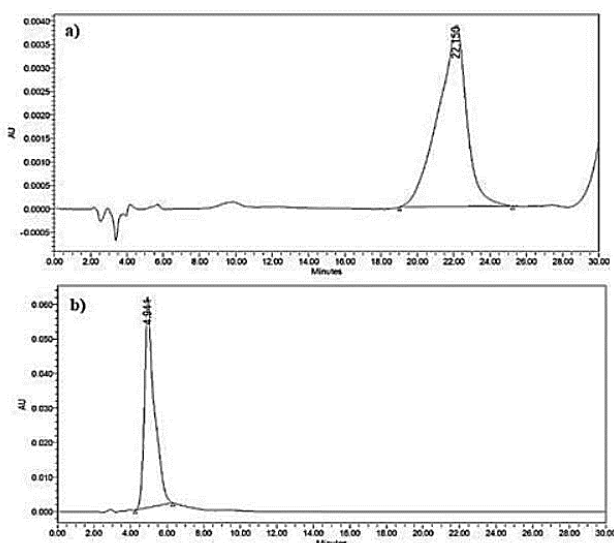
Figure 6. HPLC chromatograms of DXC aqueous solution (a) before PF treatment and (b) after PF treatment.

ANN modeling

To obtain the best combination of components for an ANN-MLP architecture for the prediction of removal efficiency of DXC by PF process, three-layered have been used: input layer, one hidden layer using tangent sigmoid (*tansig*) function as a transfer function, and output layer using linear (*purelin*) function as transfer function (Figure S1, Supplementary). From Table S1, it was observed that the suitable network architecture was taken for 18 neurons in the hidden layer with

150000 iterations.

The dispersed diagrams are revealed in Figure S2 (Supplementary). It has been observed that the plotting of the predicted RE using experimental results is very satisfactory. The values of MSE and R^2 for the training phase were found to be $2.9759.10^{-5}$ and 0.99998, respectively, which indicated that the predicted outputs were very agreed with the corresponding experimental. For the phases of testing and validation, it also indicated that the developed neural model reproduces effectively all used data.

The structure of the model which gives the lowest MSE consists of one hidden layer (*tansig*) with 18 neurons and (*purelin*) as a transfer function at the output layer. The developed model showed an excellent performance with a determination coefficient (R^2) of 0.997 and MSE of $3.76.10^{-4}$. Elmolla *et al*. [22] have developed an ANN model to predict the performance of FP for the removal of amoxicillin, ampicillin, and cloxacillin. The configuration of the backpropagation neural network giving the smallest mean square error (MSE) was a three-layer ANN with tangent sigmoid transfer function (tansig) at hidden layer with 14 neurons, linear transfer function (purelin) at the output layer and Levenberg-Marquardt backpropagation training algorithm (LMA) with a determination coefficient (R²) of 0.997 and MSE of $3.76.10^{-4}$

Global sensitivity analysis

In the present study, the weight method was carried out to perform the effect of each input variable on the output variable. An equation using a partitioning of connection weights (Eq. 14) can be used, [23]:

$$I_j = \frac{\sum_{m=1}^{m=N_h}\left(\left(\frac{\left[w_{jm}^{ih}\right]}{\sum_{k=1}^{Ni}abs\left(w_{km}^{ih}\right)}\right)\cdot abs\left(w_{mn}^{h0}\right)\right)}{\sum_{k=1}^{k=Ni}\left(\sum_{m=1}^{m=Nh}\left(\frac{\left[\left(w_{km}^{ih}\right)\right]}{\sum_{k=1}^{Ni}\left[\left(w_{km}^{ih}\right)\right]}\right)\cdot\left(\left[\left(w_{mn}^{h0}\right)\right]\right)\right)} \tag{14}$$

where I_j is the relative sensitivity of the jth input variable to the output parameter; N_i and N_h represent the number of input and hidden neurons, respectively; "W" are connection weights. The exponent i, h and o refer to the input, hidden, and output layers, respectively, and the clues k, m and n refer to the input, hidden, and output layers, respectively.

As indicated in Figure S3, all variables have strong effects on the removal efficiency of DXC. Therefore, initial DXC and catalysis concentrations

19

were depicted to be the significant influential parameter with a relative influence of 27% then pH (24%), as well as hydrogen peroxide initial dosage (22%). Some anterior research carried out on the removal of organic molecules by the PF process reported different values of the relative importance of input variables, this may depend on operational conditions and variables that the researcher has taken into account [21,23].

To facilitate the computing of the output variable (RE) knowing only the selected inputs (pH, $[DXC]_0$, $[H_2O_2]_0$, and $[Fe^{2+}]_0$) through the best-established ANN architecture (weights and biases), a graphical interface (Figure S4) was developed via a MATLAB program.

CONCLUSION

The removal efficiency of doxycycline hyclate by homogeneous photocatalysis $H_2O_2/Fe^{+2}/UV$ reached a maximum value of 79% at pH 3, 2.5 mg/L of DXC, 76.5315 mg/L of H_2O_2 and 86.8 mg/L of Fe^{2+}. Spectroscopy and chromatography analysis confirmed the potential capacity of the photo-Fenton process to transform doxycycline molecule on small fragment metabolite. Therefore, a three-layered feed-forward back propagation ANN was developed to predict removal efficiency using experimental data. The structure of the OANN-MLP that yielded the best statistical parameters: MSE equal to $2.9759.10^{-5}$ and R^2 equal to 0.99998, consisted of one hidden layer with a *tansig* function using 18 neurons and *purelin* function as the output layer function. Sensitivity analysis showed that initial concentrations of doxycycline and ferrous ions have the most effect on removal efficiency (27%). Finally, the results of interpolation and extrapolation confirmed that the ANN model could effectively reproduce experimental data and predict the performance of the process in the domain of the studied input variables.

ACKNOWLEDGMENT

NOMENCLATURE

ANN	Artificial Neuronal Network
AOP	Advanced Oxidation Process
C_0	Initial DXC concentration, mg/L
C_t	DXC concentration at a time t, mg/L
DXC	Doxycycline hyclate
FTIR	Fourier Transform Infrared
HPLC	High-Performance Liquid Chromatography
I_j	Relative sensitivity of the jth input variable to the output parameter
M_i	Molecular weight of each molecule, such as doxycycline hyclate, hydrogen peroxide, and iron
MAE	Absolute mean error
MSE	Mean squared error
NRMSE	Root of the normalized mean squared error
N_i and N_h	Number of neurons in the input and hidden layers, respectively
PF	Photo-Fenton
RE	Removal efficiency, %
TC	Tetracycline
RMSE	Root mean squared error
R^2	Coefficient of determination
y_{norm}	Normalized value
y	Experimental data
y_{max}	Maximum experimental value
y_{min}	Minimum experimental value
W	Connection weights

REFERENCES

[1]   A. A. Borghi, M. F. Silva, S. Al Arni, A. Converti, and M. S. A. Palma, J. Chem. 2015 (2015) 1–9. https://doi.org/10.1155/2015/492030.

[2]   D. Xu Y. Gao, Z. Lin, W. Gao, H. Zhang, K. Karnowo, X. Hu, H. Sun, S. Shatir, S. Hassan, S. Zhang, Front. Chem. 7 (2020) 1–18. https://doi.org/10.3389/fchem.2019.00943.

[3]   J. Scaria, K. V. Anupama, P. V. Nidheesh, Sci. Total Environ. 771 (2021) 145291. https://doi.org/10.1016/j.scitotenv.2021.

[4]   R. Daghrir, P. Drogui, Environ. Chem. Lett. 11 (2013) 151–156. https://doi.org/10.1007/s10311-012-0390-2.

[5]   T. Han, Y. Liang, Z. Wu, L. Zhang, Z. Liu, Q. Li, X. Chen, W. Guo, L. Jiang, F. Pan, S. Ge, Z. Mi, Z. Liu, H. Huang, X. Li, J. Zhou, Y. Li, J. Wang, Z. Zhang, Y. Tang, M. Wu, J. Hazard. Mater. 380 (2019) 120885. https://doi.org/10.1016/j.jhazmat.2019.120885.

[6]   J. Bolobajev, M. Trapido, and A. Goi, Chemosphere 153 (2016) 20–23. http://doi.org/10.1016/j.chemosphere.2016.03.042.

[7]   M. Hui Zhang, H. Dong, L. Zhao, D. X. Wang, D. Meng, Sci. Total Environ. 670 (2019) 11–21. https://doi.org/10.1016/j.scitotenv.2019.03.180.

[8]   P. V. Nidheesh, R. Gandhimathi, and S. T. Ramesh, Environ. Sci. Pollut. Res. 20 (2013) 2099–2132. https://doi.org/10.1007/s11356-012-1385-z.

[9]   S. M. Aramyan, , Int. J. Environ. Sci. Nat. Resour. 2 (2017) 1–18. ISSN: 2572-1119.

[10] Y. Mesellem, A. A. El Hadj, M. Laidi, S. Hanini, M. Hentabli, Neural Comput. Appl 2 (2021). https://doi.org/10.1007/s00521-021-05890-2.

[11] A. Adda, S. Hanini, S. Bezari, M. Laidi, M. Abbas, Environ. Eng. Res. 27 (2021). https://doi.org/10.4491/eer.2020.383.

[12] P. Kundu, A. Debsarkar, S. Mukherjee, S. Kumar, Environ. Technol. (United Kingdom). 35 (2014) 1296–1306. https://doi.org/10.1080/09593330.2013.866698.

[13] A. Giwa, A. Yusuf, H.A. Balogun, N.S. Sambudi, M.R. Bilad, I. Adeyemi, S. Chakraborty, S. Curcio, Process Saf. Environ. Prot. 146 (2021) 220–256. https://doi.org/10.1016/j.psep.2020.08.015.

[14] O. B. Ayodele, H. S. Auta, N. Md Nor, Ind. Eng. Chem.

Res. 51 (2012) 1611–1619.
https://doi.org/10.1021/ie302390b.

[15] S. Talwar, A. K. Verma, V. K. Sangal, J. Environ.
Manage., 250, July, (2019),
https://doi.org/10.1016/j.jenvman.2019.109428.

[16] S. Sethi, A. Dhir, V. Arora, React. Kinet. Mech. Catal.,
136, 1, (2023) 549–565, https://doi.org/10.1007/s11144-023-02360-9.

[17] N. Boucherit, M. Abouseoud, L. Adour, Nov. Biotechnol.
Chim. 17 (2018) 160–171. https://doi.org/10.2478/nbec-2018-0017.

[18] A. Babuponnusami, K. Muthukumar, J. Environ. Chem.
Eng. 2 (2014) 220–226.
http://doi.org/10.1016/j.jece.2013.10.011.

[19] L.G. Devi, K.E. Rajashekhar, K.S. Anantha Raju, S.G.
Kumar, Desalination 270 (2011) 31–39.

http://doi.org/10.1016/j.desal.2010.11.017.

[20] J. Jeong, W. Song, W. J. Cooper, J. Jung, J. Greaves,
Chemosphere 78 (2010) 535–540.
http://doi.org/10.1016/j.chemosphere.2009.11.024.

[21] R. Pulicharla S.K. Brar, T. Rouissi, S. Auger, P.
Drogui, M. Verma, R.Y. Surampalli, Ultrason. Sonochem.
34 (2017) 332–342.
http://doi.org/10.1016/j.ultsonch.2016.05.042.

[22] E. S. Elmolla, M. Chaudhuri, and M. M. Eltoukhy, J.
Hazard. Mater. 179 (2010) 127–134.
http://doi.org/10.1016/j.jhazmat.2010.02.068.

[23] M. Laidi and S. Hanini, Int. J. Refrig. 36 (2013) 247–257.
http://doi.org/10.1016/j.ijrefrig.2012.09.016.

NABILA BOUCHERIT[1]
SALAH HANINI[1]
ABDELLAH IBRIR[2]
MAAMAR LAIDI[1]
MOHAMED ROUBEHIE FISSA[1]

[1]Biomaterials and Transport
Phenomena Laboratory
(LBMPT), Yahia Fares
University, Medea, Algeria

[2]Materials and Environment
Laboratory (LME), Faculty of
Technology, Yahia Fares
University, Medea, Algeria

PREDVIĐANJE UKLANJANJA DOKSICIKLINA FOTO-FENTON PROCESOM KORIŠĆENJEM VEŠTAČKE NEURONSKE MREŽE - VIŠESLOJNI PERCEPTRONSKI MODEL

Ovaj rad predstavlja studiju efikasnosti foto-Fentonovog procesa (PF) za uklanjanje antibiotika doksiciklin-hiklata (DXC). Eksperiment je pokazao da je najbolja postignuta efikasnost uklanjanja (79%) pri pH 3 za 2,5 mg/L DKSC, 76,53 mg/L H_2O_2 i 86,8 mg/L Fe^{2+}. Mehanizam degradacije DKSC hidroksilnim radikalima je potvrđen metodama FTIR i 543.544.5. Za modelovanje reakcije oksidacije DXC pomoću PF, korišćena je optimizovana veštačka neuronska mreža (OANN) zasnovana na višeslojnom perceptronu, uzimajući u obzir eksperimentalne podatke, kao što su pH i početne koncentracije DXC, H_2O_2 i Fe^{2+}. OANN je predvidela rezultate efikasnosti uklanjanja u saglasnosti sa eksperimentalnim rezultatima, sa RMSE od 0,0661 i R^2 vrednošću od 1,000. Analiza osetljivosti je otkrila da su svi proučavani ulazi značajno uticali na transformaciju DXC-a.

Ključne reči: doksiciklin-hidrat; modeliranje; foto-Fenton; optimizovana veštačka neuronska mreža; uklanjanje.

NAUČNI RAD

SURESHKUMAR
PETCHIMUTHU[1]

SATHIYA MOORTHY
RAJENDRAN[2]

[1]Department of Mechanical
Engineering, Government
College of Engineering,
Tirunelveli, India

[2]Department of Mechanical
Engineering, Anna University
Regional Campus, Coimbatore,
India

SCIENTIFIC PAPER

EXPERIMENTAL STUDY OF SOLAR AIR HEATER WITH C-SHAPED RIBS COATED WITH ZEOLITE

Article Highlights
- Improve the performance of an SAH using C-ribs with zeolite coating on the absorber plate
- A high rib height promotes increased turbulence and mixing of air flowing through the SAH duct
- Smaller holes can exaggerate heat transfer and enhance the cross-flow effect
- Zeolite coatings, serve to enhance the thermal performance by desorption and adsorption processes

Abstract

A study was conducted to determine the heat transmission rate and friction properties of a solar air heater's (SAH) absorber by including a c-shaped rib, with and without perforations, and the efficiency of this absorber with and without zeolite coating was investigated. This research is carried out by varying Reynolds numbers (Re) ranges between 3000 to 18000, the height of the C-shaped rib (e) ranges between 2 mm to 4 mm, and the embedded hole diameter in the C-shaped rib ranges between 1 mm to 3 mm. The impact of rib height, hole diameter, and zeolite coating on thermal efficiency and Nusselt number is compared to a flat channel under the same flow environments. A strong secondary flow is created by the free shear layer reattaching more often at higher rib heights, and a smaller hole can exaggerate heat transfer and enhance the cross-flow effect. The thermal efficiency and Nusselt number of the solar air heater with c-ribs (Rib height = 4 mm and hole diameter = 1 mm) and zeolite coating on the absorber increased by 29.7% and 62.2% over the flat absorber. Ribs 4 mm high can increase duct friction by up to 3.1 times compared to a smooth duct.

Keywords: C-shaped ribs; perforations; zeolite coating; thermal performance; friction factor.

Solar air heaters are a fundamental part of solar energy utilization systems. They are designed to absorb incoming solar light and convert it into thermal energy at the absorber plate. The heated absorber plate transfers thermal energy to the air passing through the duct via convection. The thermal energy stored in the hot absorber plate is transferred to the air because of the temperature disparity. This process heats the air as it passes through the SAH. These SAH systems are used in various applications for heating purposes, including space heating, preheating air for combustion processes, drying crops, desalination (evaporating seawater to produce fresh water), and water heating. The efficiency of flat SAHs is low because there is not enough convective heat transfer between the fluid and the absorber. Consequently, the temperature of the absorber rises, and more heat emission to the atmosphere is higher. The existence of a viscous sub-layer is most often due to poor heat transfer; this layer can be eliminated by roughening the absorber. Various techniques, including the incorporation of fins, artificial roughness, and packed beds within ducts, have been proposed as methods to enhance thermal performance. Implementing

roughened surfaces on the absorber plate, such as ribbed or corrugated surfaces, disrupts laminar airflow and promotes turbulence. This improves the transfer of heat from the absorber to the air. Applying selective coatings to the absorber plate maximizes solar absorption while minimizing thermal radiation losses, improving overall efficiency.

Yadav et al. [1] tested the impact of a circular rib positioned in an angular arc approach and discovered that heat transmission and friction were greater than the flat one. Lanjewar et al. [2], investigating the influence of W-shaped ribs as an artificial element, found that thermo-hydraulic performance was extreme at a slant of attack of 60°. Pandey et al. [3] explored the impact of relative roughness height, arc angle, pitch, width, and gap distance on Nusselt number (Nu), and friction (f) using multiple-arc-shaped ribs fixed over an absorber. The author found that Nu = 5.85 and f = 4.96 were superior to flat channels. Saini et al. [4] probed the impact of ribs with dimple forms over the Nusselt number and friction factor. Unlike flat absorbers, ribs considerably improved Nu and friction qualities. Varun et al. [5] researched the impact of inclined and transverse ribs above the absorber. At a relative roughness pitch of 8, a higher thermal efficiency was reached. Kumar et al. [6] experimented with the impact of separate W-shaped ribs and discovered that the Nusselt number and friction factor of 1.67 and 1.82, respectively, were attained at an angle of attack of 60°. Sahu and Prasad [7] theoretically investigated arc-shaped wire protrusions over the absorber. They reported that the roughness height of 0.0422 improved the exergetic efficiency by 56% compared to the flat absorber.

Jin et al. [8] numerically analyzed the impact of an artificial roughness of many V-shaped ribs over the absorber. They stated that V-shaped ribs create streamwise helical vortex flows that augment the performance of SAHs. Yadav and Bhagoria [9] revealed by a numerical study that square-separated transverse rib along relative roughness, pitch, and height gave a better thermo-hydraulic performance.

Aharwal et al. [10] researched the impact of gap width and the position of a slanted continuous rib on heat transfer and the friction factor. The optimal width of 1.0 and the position of 0.25 provided better thermo hydraulic performance. Sahu and Bhagoria [11] explored the effect of the heat transmission coefficient in 90°-broken ribs and found that the thermal efficiency ranged from 51% to 83.5%. Hans et al. [12] studied the outcome of several V-ribs on the absorber of a SAH in the following ranges: Re from 2000 to 20000, e/D from 0.019 to 0.043, P/e from 6 to12, a from 30° to 75°, and W/w from 1 to 10. They found that the heat transfer and

friction were six- and five-fold greater compared with the flat absorber. Ghritlahre et al. [13] examined the thermal performance and heat transfer of an arc-shaped roughened SAH with two different airflow orientations: apex up and apex down. The experiments were conducted using different mass flow rates, spanning from 0.007 kg/s to 0.022 kg/s. The roughness parameters taken into study included "relative roughness pitch, relative roughness height, rib roughness, and arc angle". The heat transfer in the apex-up configuration was 33.2% more efficient than the apex-down arrangement. These results suggest that the rib roughness absorber with the apex-up airflow with wire is more efficient than the apex down airflow of the SAH.

Agrawal et al. [14] empirically studied the impact of double arc reverse formed along a consistent gap and discovered a Nusselt number of 2.85 and a friction factor of 2.42, both of which were higher than those of a flat absorber. Singh et al. [15] examined the effect of several arc ribs on thermal performance. They discovered a huge increment of Nusselt number (5.07) and friction factor (3.71) compared to the flat one.

Kumar et al. [16] experimentally researched the impact of nanomaterial interfering with a black-paint covering on an absorber. They concluded that the entropy formation rises with increasing the flow rate. Exergy effectiveness for BP-2 was 4.27% greater than that for BP-1. Jelonek et al. [17] studied the effectiveness of a new sand-plastered and sand-packed (SCSF) polycarbonate sheet of a solar air collector (SAC). It was discovered that the SAC with storing offered 39% and 20% greater efficiency than the other two. After an extensive survey, it could be inferred that researchers have worked on varying the geometric parameters like Rib roughness, height, pitch, and coating over the absorber for better thermal performance of SAHs.

In light of the foregoing, the present study was conducted to determine Nusselt number and friction characteristics over the heated surface using a C-shaped rib with and without holes embedded in it to generate vortices as a roughness element on the absorber surface. The C-shaped rib configuration can induce strong vortices and turbulence in the boundary layer flow. This enhanced turbulence promotes better mixing and heat transfer amid the fluid and the solid surface, leading to improved convective heat transfer coefficients. Compared to other rib configurations, such as rectangular or trapezoidal ribs, the C-shaped rib may offer the advantage of a lower pressure drop. The streamlined shape of the C rib could help minimize flow resistance while still effectively enhancing heat transfer. The experiment was also carried out by adding

a zeolite coating to the absorber plate. Researchers have looked at a wide variety of roughness element forms and sizes, but none have made an effort to test the effects of the current geometry and coating on heat convection.

MATERIAL AND METHODS

Materials

The effects of several C-shaped ribs on heat transfer and frictional properties of SAH have been studied in the experiment. Fig. 1 provides a graphical depiction of the experiment. The air duct is split into three distinct areas: entrance, testing, and exit. The entire duct is 1750 mm long, with a testing section length of 1000 mm having a corresponding 80 mm hydraulic diameter. The lengths of the entering and exiting segments are 500 mm and 250 mm, respectively. To determine proper entry and exit dimensions, ASHRAE standard 93-77 was used as a reference. According to it, the minimum inlet and outlet lengths for the zig-zag flow regime should be $5\sqrt{WH}$ and $2.5\sqrt{WH}$, respectively. Improved airflow across the absorber's surface was achieved by inserting guide vanes at the inlet. Wood was chosen as the duct's primary construction material because it was affordable, abundant, and good at insulating. A GI sheet absorber plate of 3 mm thickness was made. The upper surface of the absorber was artificially roughened using riveted C-shaped ribs. The absorber plate was made as the duct bottom wall, and the glass wool was used to insulate the sidewalls.

To measure the input and output air temperatures, thermocouples have been installed. Calibrated K-type thermocouples with digital displays, showing output in degrees Celsius with an accuracy of 0.1 °C, were employed to determine the air and absorber plate temperatures across multiple locations. A standard thermometer was used to calibrate the thermocouples. The position of the twelve thermocouples installed at regular intervals to gauge the average temperature of the absorber is shown in Fig. 2a. A calibrated orifice meter coupled with a U-tube manometer was included for determining the airflow rate. A Pitot tube was utilized for the orifice plate calibration. The inlet flow rate was regulated by a regulating valve at the entry. The pressure downfall in the test area was measured with a digital micromanometer. Rib placements above the absorber are shown in Fig. 2b.

Methods

Before the commencement of the experiment, the parts and instruments were tested for functionality. Under steady-state conditions, the requisite heat
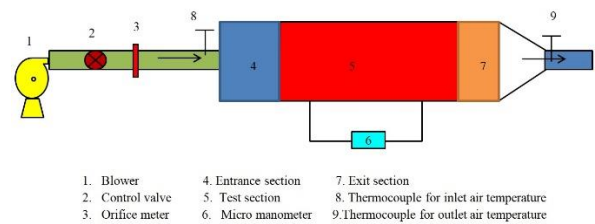
Figure 1. The experiment setup.

1. Blower   4. Entrance section   7. Exit section
2. Control valve   5. Test section   8. Thermocouple for inlet air temperature
3. Orifice meter   6. Micro manometer   9. Thermocouple for outlet air temperature
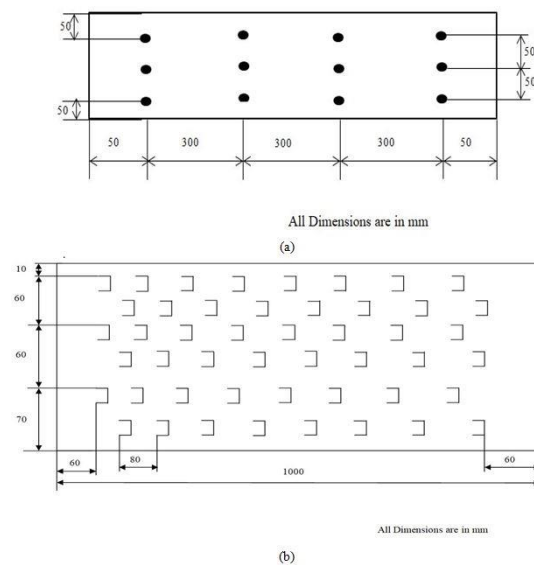
Figure 2. (a) Thermocouples fixed over the test section; (b) Rib positions over the absorber plate.

transfer investigations were carried out. The airflow rate ranged between 0.0064 kg/s and 0.0386 kg/s with four in-between values to represent all possible variations of the Reynolds number from 3,000 to 18,000 respectively.

The average solar intensity (I) was 800 W/m² at Bodinayakanur, Tamil Nadu, India, in May 2023. Since the working fluid was air, density, specific heat, thermal conductivity, and dynamic viscosity are 1.225 kg/m³, 1006 J/kg K, 0.0262 W/m K, 1.81×10⁻⁵ kg/m s, respectively.

The following variables were assessed during experimentation: air temperature at entry, air temperature at exit, mean temperature of the absorber plate, pressure drop across the test section.

Data reduction

The airflow rate, the heat transfer to the air, the Nusselt number, the heat transfer coefficient, and the friction factor were quantified with available data from the present study.
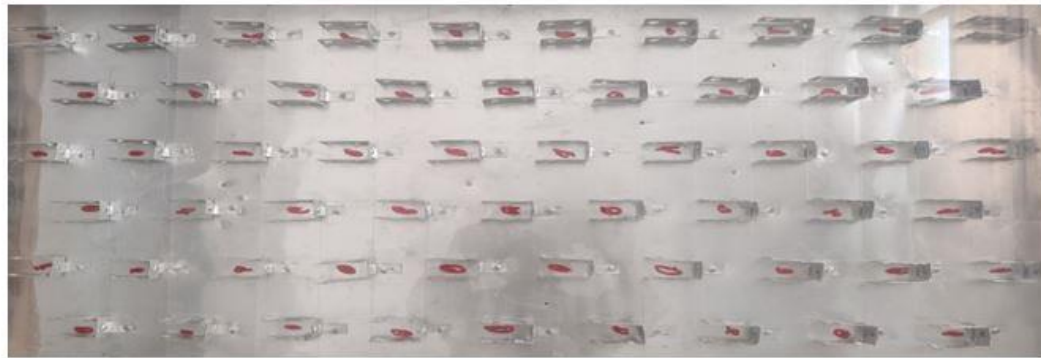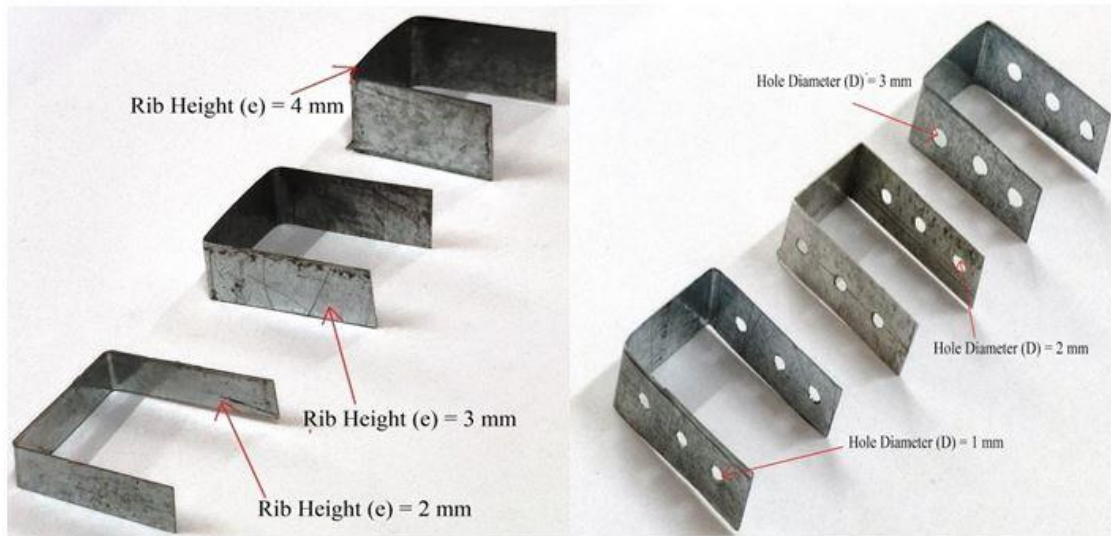
Figure 3. (a) Pictorial view of e = 4 mm, D = 1 mm and zeolite coating; (b) Enlarged view of rib heights; (c) Enlarged view of a rib height (e) = 4 mm and hole diameters of 1, 2 and 3 mm.

The necessary parameters: the mass flow rate, heat transfer, thermal efficiency, and heat transfer coefficient were evaluated as per the highlighted references deceased [18] using Eqs. (1–4), respectively:

$$m = \rho A V \qquad (1)$$

$$Q = m C_p \left(T_0 - T_i \right) \qquad (2)$$

$$\eta = \frac{Q}{I A_c} \qquad (3)$$

$$h = \frac{Q}{A_c \left(T_p - T_f \right)} \qquad (4)$$

where $A = \frac{\pi}{4} d^2$, $T_f = \frac{(T_i + T_o)}{2}$,

$T_p = \frac{(T_1 + T_2 + T_3 + T_4 + T_5 + T_6 + T_7 + T_8 + T_9 + T_{10} + T_{11} + T_{12})}{12}$, and A_c is the length of the absorber × width of the absorber.

26

The Nusselt number and friction factor for the roughened absorber are defined by Eqs. (5) and (6), respectively:

$$Nu = \frac{h D_h}{k} \qquad (5)$$

$$f = \frac{D_h \Delta P}{2 L V^2 \rho} \qquad (6)$$

Validity test

The experimentally obtained Nusselt number and friction factor values in the flat were compared with the value computed by the Dittus-Boelter and Modified Blasius equations, i.e., Eqs. (7) and (8), respectively.

$$Nu_s = 0.023 \, Re^{0.8} \, Pr^{0.4} \qquad (7)$$

$$f_s = 0.085 \, Re^{-0.25} \qquad (8)$$
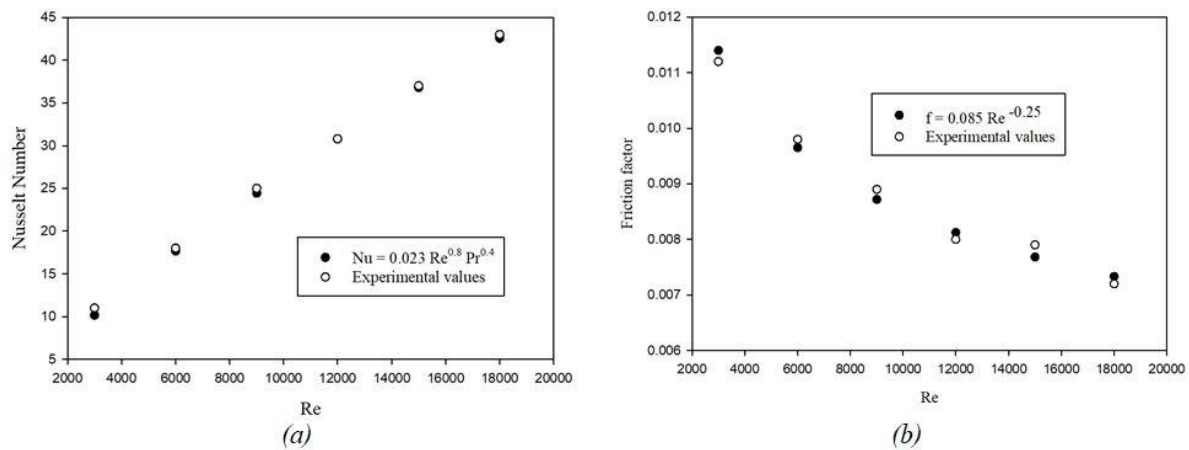
Figure 4. (a) Validation of smooth plate for Nu; (b)Validation of smooth plate for f.

Figs. 4a and 4b graphically represent the experimental and mathematically established Nu and f-values, respectively. The mean deviation of Nu and friction factor values were 2.7% and 2.6%, respectively, confirming a high conformity degree between the predicted and the experimental values and thus, validating the setup of the experiment.

Uncertainty analysis

The uncertainty analysis is a useful and efficient tool for developing and planning experiments. Eq. (9) is used to determine the uncertainty measurement:

$$W_R = \sqrt{\left[\left(\frac{\partial R}{\partial x_1}w_1\right)^2 + \left(\frac{\partial R}{\partial x_2}w_2\right)^2 + \ldots + \left(\frac{\partial R}{\partial x_n}w_n\right)^2\right]} \quad (9)$$

where, $X_1, X_2 \ldots X_n$ are the independent variables, and $W_1, W_2 \ldots W_n$ are the uncertainties of the independent variables

Thermal efficiency, Nu, and friction factor uncertainties are 3.20%, 3.32%, and 3.26%, respectively, which are within acceptable ranges. The following uncertainties are associated with the measurements of the mass flow rate, temperature, radiation, pressure drop, duct height, and absorber plate length are ± 0.001 m³/hr, ± 0.1 °C, ± 1 W/m², ± 0.098 Pa, ± 0.1 mm, and ± 0.6 mm, respectively.

RESULTS AND DISCUSSION

The significance of the rib height, hole diameter, and zeolite coating for the heat transmission and friction qualities of a roughened absorber were investigated.

Heat transfer properties

This part of the study focused on examining the thermal characteristics and performance of the SAH system, aiming to a detailed analysis of the heat transfer processes occurred and their impact on the overall system efficiency.

Effect of Reynolds number

As the Reynolds number goes up, the Nusselt number consistently rises because the viscous layer near the surface gets thinner, allowing for more heat transfer. On the other hand, the friction factor consistently falls with increasing the Reynolds number. In smooth ducts with fully developed flow, this decrease is due to less resistance from the thinned viscous sublayer. However, it also means a larger pressure drop along the duct, requiring more pumping power. Adding roughness to the absorber plate disrupts the smooth flow, creating more turbulence and causing a higher friction factor compared to a smooth plate.

Effect of rib height

The effect of rib height (e) on the thermal efficiency and Nusselt number for 3,000 < Re < 18,000 is depicted in Figs. 5a and 5b. The thermal efficiency of the SAH is directly proportional to the flow rate at the entry. As the mass flow rate rises, the thermal efficiency increases because more heat is removed by the working fluid. As the rib height increases, the Nusselt number and thermal efficiency increase due to a secondary flow created by the free shear layer at a higher rib height. A high rib height promotes increased turbulence and mixing of air passing through the SAH duct. Turbulence enhances heat transfer by disrupting laminar flow and promoting convective heat exchange between the hot absorber plate and the air. Taller ribs provide a larger surface area for the heat transfer between the absorber and the airflow. This increased surface area allows for greater contact between the

27

heated absorber and the air, facilitating more efficient heat transfer. In contrast, a low rib height may result in less turbulence and mixing, leading to reduced heat transfer enhancement compared to higher rib heights. Shorter ribs offer less surface area for heat transfer, potentially limiting the effectiveness of convective heat exchange within the SAH duct. Lower rib heights typically result in lower pressure drop and energy losses than higher rib heights. However, the lower rib height reduces the heat transfer efficiency. In addition, by including a C-shaped rib, the local wall turbulence is induced in the heat transmission region. The thermal resistance falls significantly as the heat transfer

improves. The main flow impinges on the surface as the rib height increases, increasing the heat transfer rate for all Re values. A reduction in heat transfer from the surface of the absorber is observed if the rib height is beyond 4 mm because the free shear layer cannot rejoin. The reduced rib height allows reconnected air to travel further before colliding with subsequent ribs, enabling the regrowth of a viscous sub-layer on a localized region of the heater's surface. The regrowth of the boundary layer causes a decrease in the Nu number, causing an adverse effect on the heat transfer from the absorber.
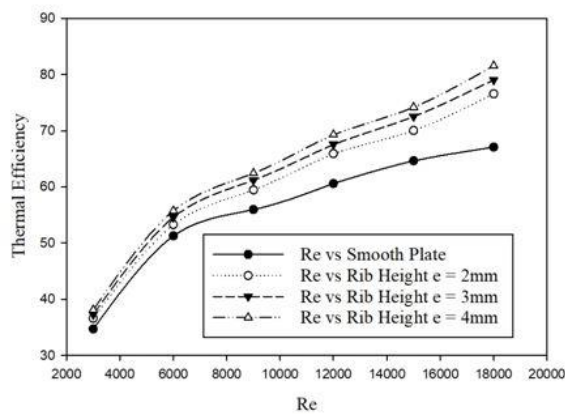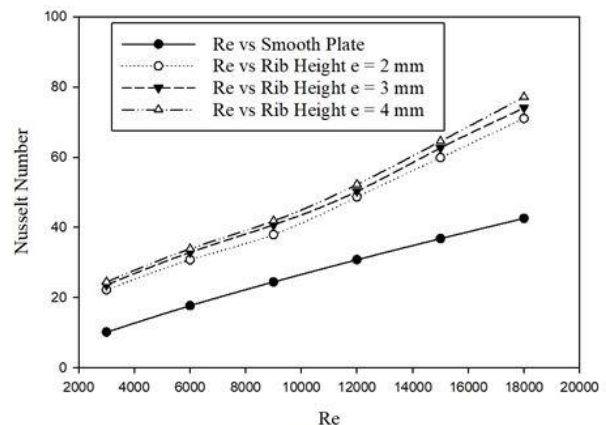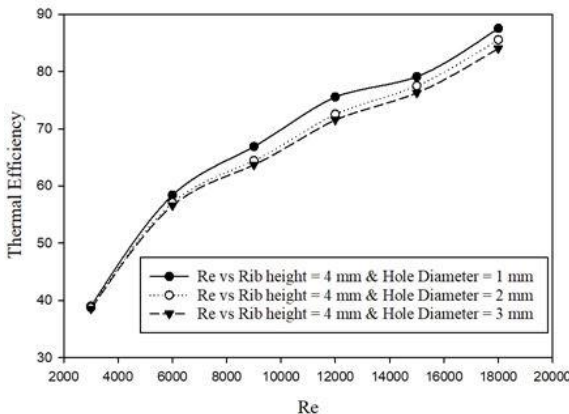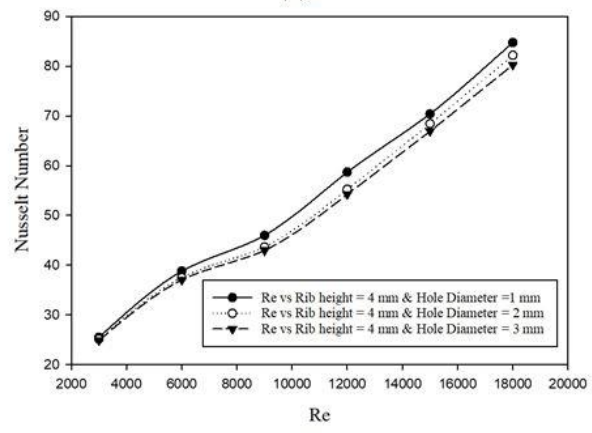
Figure 5. (a) Thermal efficiency vs Re for rib height; (b) Nu vs Re for rib height; (c) Thermal efficiency vs Re for hole diameter; (d) Nu vs Re for hole diameter.

Effect of hole diameter

Figs. 5c and 5d show how the thermal efficiency and Nusselt number are changed as a consequence of the hole diameter for the Re number range applied. As the hole diameter increases, thermal efficiency decreases. A smaller opening can increase the cross-flow effect and heat transfer rate. The C-shaped configuration with a 1 mm hole diameter has the highest exit temperature because the air has to go through a smaller hole before it moves out, so it stays in the test part for a longer duration. Additionally, it generates

several small vortices in the rib region, which in turn increases the turbulence responsible for better thermal efficiency and higher Nusselt number. In addition, smaller hole diameters provide a larger surface area for heat transfer between the absorber and the airflow, which facilitates a more effective convective heat exchange and enhances the heat transfer efficiency within the SAH duct. Larger holes do not contribute to enhanced heat transmission because of the sluggish flow regime, and higher hole diameters offer less surface area for heat transfer, potentially limiting the

convective heat exchange and reducing the heat transfer efficiency compared to the systems with smaller hole diameters.

Effect of zeolite coating

Figs. 6a and 6b illustrate the variation in the thermal efficiency and Nusselt number of the zeolite-coated absorber for different Re number values. The rib height of 4 mm and the embedded hole diameter of 1 mm with a zeolite coating enable a better heat transfer rate. Desorption and adsorption techniques are used by the zeolite for storing and releasing heat. In the context of heat storage, adsorption refers to the process where molecules of a gas or vapor adhere to the surface of the zeolite. When a zeolite material is exposed to heat, it can adsorb molecules of a specific gas or vapor, typically water vapor or other volatile organic compounds, into its porous structure. This adsorption process is exothermic, meaning it releases heat energy as the molecules are attracted to the surface of the zeolite. Desorption is the reverse process of adsorption. When the zeolite material is subjected to a decrease in temperature or a decrease in pressure,

the adsorbed molecules are released from the surface of the zeolite. This desorption process is endothermic, meaning it requires energy input to break the bonds between the molecules and the zeolite surface. The energy required for desorption is typically supplied in the form of heat, which can be provided by solar energy in solarly air-heated systems. Zeolite naturally has an exothermic characteristic, making it an excellent solar collector for use in thermal applications. Zeolite has around 20% to 50% intra-crystalline voids.

A zeolite coating over the absorber collects the heat from sunlight. Wet air is passed via the air heater to extract and utilize the heat stored in the zeolite-coated absorber. This enables the zeolites to dry the air by adsorbing the water from it. The air warms up as a result of the exothermic adsorption. A strong secondary flow is created by the free shear layer reattaching more often at higher rib heights, and a smaller hole can exaggerate heat transfer and enhance the cross-flow effect. Larger holes do not participate in the enhancement of heat transmission due to the stagnant flow regime. The heat transmission is improved as a result of the smaller holes.
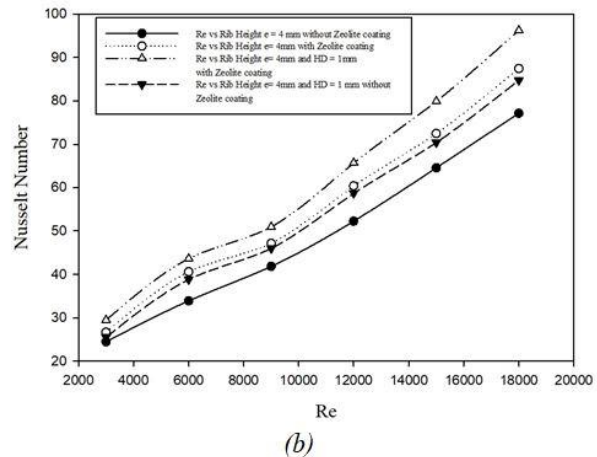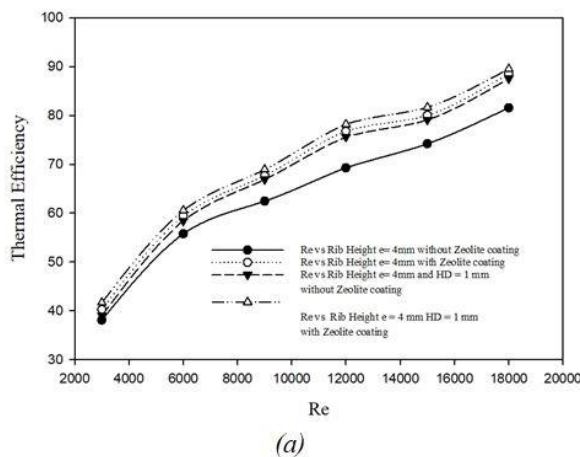
Figure 6. (a)Thermal efficiency vs Re for zeolite coating; (b) Nu vs Re for zeolite coating.

Friction factor characteristics

Fig. 7 shows the impact of hole diameter and rib height on the friction factor for 3000 < Re > 18000. Blasius correlation is used in computing the friction factor for a flat passage. It manifests that the friction factors drop with a rise in the Re number due to the thinning of the viscous sublayer; the Re number increases due to a rise in the mean flow velocity when the friction factor decreases.

As the Re number increases, the pressure in the test region decreases. The friction factor varies inversely to the mean square of the fluid velocity and is directly related to the pressure. Consequently, a rise in the mean fluid velocity predominates over a rise in the

pressure downfall. The friction factor declines in tandem with increasing the Re number. The friction factor is larger with the 4 mm rib height compared to that with an embedded hole. As the roughness height rises, so does the friction factor. As rib height increases, the flow becomes more turbulent, causing an increase in the viscous drag over the absorber and ultimately the friction factor rises. Rise in turbulence is not very incisive at lesser rib heights. The holes in the ribs cause an increase in the ratio of the open regions. The higher the ratio of the open region, the lower the pressure within the SAH, as the friction factor is significantly reduced due to a decrease in pressure loss compared to ribs without perforations.
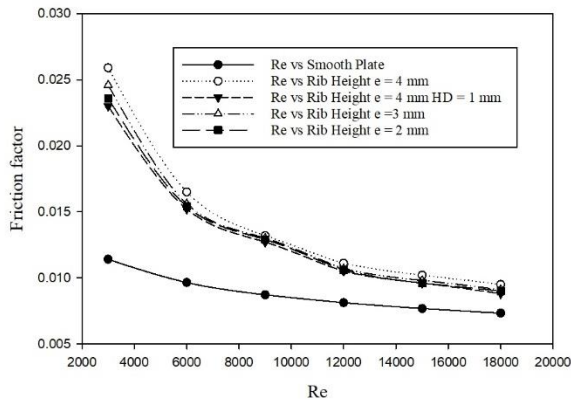
Figure 7. Friction factor vs Re.

Comparison of C-shaped, V-shaped, and circular ribs

Compared to V-shaped and circular ribs, C-ribs offer potentially superior heat transfer due to their open face facilitating better air contact with the collector plate and more efficient heat transfer from the absorber to the air. Additionally, C-shaped ribs might have a lower pressure drop because of the larger flow passage area they create. On the other hand, V-shaped and circular ribs generally have moderate heat transfer and pressure drop characteristics. These are used for space heating in winter sessions. C-shaped ribs can enhance heat transfer, potentially allowing for a smaller collector size to meet heating needs, which can be beneficial for space-constrained rooftops.

CONCLUSION

These inferences can be made based on the findings of this experimental study. As the Re number increases, the thermal performance rises and the friction falls. The friction and thermal properties of a C-rib are higher when compared to a flat absorber. This is because roughness changes the flow properties, leading to flow separation, the creation of secondary flows, and reattachments.The thermal efficiency and Nu number of the SAH with C-ribs (rib height = 4 mm and hole diameter = 1 mm) and the zeolite coating on the absorber increased by 29.7% and 62.2%, respectively, over the flat absorber. A strong secondary flow is created by the free shear layer reattaching more often at higher rib heights, and a smaller hole can exaggerate heat transfer and enhance the cross-flow effect. Desorption and adsorption techniques are used by the zeolite for storing and releasing heat due to the inherent exothermic property of zeolite, which makes it suitable for efficiently harvesting solar energy for heating applications. 4 mm high ribs can increase duct friction by up to 3.1 times compared to a smooth duct. In the presence of roughness, the flow becomes more

turbulent, causing an increase in the viscous drag over the absorber compared to the smooth configuration.

NOMENCLATURE

A_c	Area of collector plate (m^2)
C_p	Specific heat of air at constant pressure (J/kgK)
D	Hole diameter (mm)
D_h	Hydraulic diameter (mm)
f	Friction factor
I	Incident radiation (W/m^2)
m	Mass flow rate(kg/s)
Nu	Nusselt number
p	longitudinal pitch
P	Pressure (Pa)
Pr	Prandtlnumber
q	Heat gain (W)
Re	Reynolds number
T_i	Temperature at the entrance (K)
T_o	Temperature at the exit (K)
ΔT	Difference in temperature (K)
v	Mean flow velocity (m/s)
Greek symbols	
ρ	Specific mass (kg/m^3)
μ	Absolute viscosity of the working fluid (kg/m s)
η	Thermal efficiency
Subscripts	
h	hydraulic
i	inlet
o	outlet
p	plate
Abbreviations	
SAC	Solar air collector
SAH	Solar air heater
SCSF	Sand coated and sand filled

REFERENCES

[1]   S. Yadav, M.Kaushal, Varun, Siddhartha, Exp. Therm. Fluid Sci. 44 (2013) 34–41. https://doi.org/10.1016/j.expthermflusci.2012.05.011.

[2]   A. Lanjewar, J.L. Bhagoria, R. Sarviya, Exp. Therm. Fluid Sci. 35 (6) (2011) 986–995. https://doi.org/10.1016/j.expthermflusci.2011.01.019.

[3]   N. K. Pandey, V.K. Bajpai, Varun, Sol. Energy 134 (2016) 314–326. https://doi.org/10.1016/j.solener.2016.05.007.

[4]   R.P. Saini, J. Verma, Energy 33 (8) (2008) 1277–1287. https://doi.org/10.1016/j.energy.2008.02.017.

[5]   Varun, R.P. Saini, S.K. Singal, Renewable Energy 33 (6) (2008) 1398–1405. https://doi.org/10.1016/j.renene.2007.07.013.

[6]   A. Kumar, J.L. Bhagoria, R.M. Sarviya, Energy Convers. Manage. 50 (8) (2009) 2106–2117. https://doi.org/10.1016/j.enconman.2009.01.025.

[7]   M.K. Sahu, R.K. Prasad, Renewable Energy 96 (2016) 233–243. https://doi.org/10.1016/j.renene.2016.04.083.

[8]   D. Jin, M. Zhang, P. Wang, S. Xu, Energy 89 (2015) 178–190. https://doi.org/10.1016/j.energy.2015.07.069.

[9]   A.S. Yadav, J.L. Bhagoria, Int. J. Therm. Sci. 79 (2014) 111–131. https://doi.org/10.1016/j.ijthermalsci.2014.01.008.

[10] K.R. Aharwal, B.K. Gandhi, J.S. Saini, Renewable Energy 33 (4) (2008) 585–596. https://doi.org/10.1016/j.renene.2007.03.023.

[11] M.M. Sahu, J.L. Bhagoria, Renewable Energy 30 (13) (2005) 2057–2073.

https://doi.org/10.1016/j.renene.2004.10.016.

[12]   V.S. Hans, R.P. Saini, J.S. Saini, Sol. Energy 84 (6) (2010) 898–911. https://doi.org/10.1016/j.solener.2010.02.004.

[13]   H.K. Ghritlahre, P.K. Sahu, S. Chand, Sol. Energy 199 (2020) 173–182. https://doi.org/10.1016/j.solener.2020.01.068.

[14]   Y. Agrawal, J.L. Bhagoria, V.S. Pagey, Mater. Today Proc. 47 (2021) 6067–6073. https://doi.org/10.1016/j.matpr.2021.04.623.

[15]   A.P. Singh, Varun, Siddhartha, Exp. Therm. Fluid Sci. 54 (2014) 117–126.

https://doi.org/10.1016/j.expthermflusci.2014.02.004.

[16]   R. Kumar, S.K. Verma, M. Singh, Mater. Today Proc. 44 (2021) 961–967. https://doi.org/10.1016/j.matpr.2020.11.006.

[17]   Z. Jelonek, A. Drobniak, M. Mastalerz, I. Jelonek, Sci. Total Environ. (2020) 141267. https://doi.org/10.1016/j.energy.2022.125507.

[18]   B. Bhushan, R. Singh, Sol. Energy 85 (5) (2011) 1109–1118. https://doi.org/10.1016/j.solener.2011.03.007.

SURESHKUMAR PETCHIMUTHU[1]

SATHIYA MOORTHY RAJENDRAN[2]

[1]Department of Mechanical Engineering, Government College of Engineering, Tirunelveli, India

[2]Department of Mechanical Engineering, Anna University Regional Campus, Coimbatore, India

EKSPERIMENTALNO PROUČAVANJE SOLARNOG GREJAČA VAZDUHA SA REBRIMA C OBLIKA OBLOŽENIM ZEOLITOM

U ovoj studija istraživane su brzina prenosa toplote i frikciona svojstva apsorbera sa solarnim grejačem vazduha sa C-rebrima, sa i bez perforacija, kao i efikasnost ovog apsorbera sa i bez zeolitne prevlake. Ovo istraživanje je sprovedeno u opsegu Rejnoldsovog broj (Re) od 3.000 do 18.000, sa C-rebrima, visine 2 mm i 4 mm, sa otvorom prečnika od 1 mm do 3 mm. Uticaj visine rebra, prečnika otvora i zeolitne prevlake na termičku efikasnost i Nuseltov broj se poredi sa ravnim kanalom pri istim protocima. Snažan sekundarni protok se stvara tako što se sloj slobodnog smicanja češće ponovno odvaja na većim visinama rebara, a manja rupa može uvećati prenos toplote i poboljšati efekat unakrsnog strujanja. Toplotna efikasnost i Nuseltov broj solarnog grejača vazduha sa C-rebrima (visina rebra = 4 mm i prečnik otvora = 1 mm) i zeolitnom prevlakom na apsorberu povećani su za 29,7% i 62,2% u odnosu na ravni apsorber. Rebra visine 4 mm mogu povećati trenje u kanalu do 3,1 puta u poređenju sa glatkim kanalom.

Ključne reči: C-rebra; perforacije; zeolitni prevlaka; toplotne performance; faktor trenja.

NAUČNI RAD

TOMÁS PESSOA LONDE CAMARGOS[1]

ANDRÉA OLIVEIRA SOUZA DA COSTA[1,2]

ESLY FERREIRA COSTA JUNIOR[1,2]

[1]Graduate Program in Mechanical Engineering, Federal University of Minas Gerais, Belo Horizonte – Minas Gerais, Brazil

[2]Graduate Program in Chemical Engineering, Federal University of Minas Gerais, Belo Horizonte – Minas Gerais, Brazil

ENERGY AND EXERGY DIAGNOSTICS OF AN INDUSTRIAL ANNULAR SHAFT LIMEKILN WORKING WITH PRODUCER GAS AS RENEWABLE BIOFUEL

Article Highlights
- Performance results for a limekiln operating with renewable biofuel were presented
- The new results exposed come from energy and exergy diagnostics of the limekiln
- Energy and exergy efficiencies of the limekiln were 54.6 and 42.2%, respectively
- Energy and exergy global efficiencies of the calcination process were 42.0 and 23.6%, respectively
- Results showed that producer gas as renewable biofuel can be competitive

Abstract

Quicklime, a globally significant commodity used in various industrial applications, is produced in limekilns requiring substantial energy, traditionally, from fossil fuels. However, due to escalating emission constraints and depletion of fossil fuel deposits, the quicklime industry explores alternative fuels, like biomass. The literature lacks feasibility diagnostic studies on limekilns using alternative biomass fuels. Thus, this article aims to conduct energy and exergy diagnostics on an industrial limekiln using producer gas derived from eucalyptus wood as a renewable biofuel. Employing industrial data and thermodynamics principles, the equipment was characterized, and results were compared with literature findings for similar limekilns using fossil fuels. The Specific Energy Consumption (SEN) for the producer gas-operated limekiln was 4.8 GJ/t_{quicklime}, with energy (η_{en}) and exergy (η_{ex}) efficiencies of 54.6% and 42.2%. Overall energy ($\eta_{en-overall}$) and exergy ($\eta_{ex-overall}$) efficiencies were 42.0% and 23.6%, respectively, lower than literature values. $SEN_{overall}$ was 7.6 GJ/t_{quicklime}, higher than the literature results. Identified enhancements for both renewable and fossil fuel-powered limekilns involve recovering energy and exergy, including heat recovery from exhaust gases, minimizing thermal losses, and optimizing operational variables. These findings offer valuable insights for researchers exploring renewable biofuel adoption, like producer gas derived from eucalyptus wood, as alternatives to conventional fossil fuels in limekilns.

Keywords: energy, exergy, limekiln, quicklime, biomass, biofuel.

Quicklime is a solid substance with $CaO_{(s)}$ as its main constituent, and it holds global significance due to its various essential applications as a chemical compo-

und. These applications include its use in mortar and cement production, water treatment, air pollution control, glass manufacturing, whitewashing acidic soils, casting steps, and as a chemical absorbent [1]. Moreover, the literature has explored innovative applications and properties of quicklime, such as its use for adsorbent development [2], novel composite material development [3], and the water transfer mechanism of quicklime-modified centrifugal dewatering clay [4]. Among the top five global quicklime producers in 2019 are China, India, USA,

Russia, and Brazil. Brazil ranks fifth in this list and produced approximately 8.1 million metric tons of quicklime in 2019 [5].

Limestone, predominantly composed of $CaCO_{3(s)}$, is utilized as the raw material for the manufacture of quicklime. In this process, either horizontal or vertical limekilns are employed, where temperatures around 900–1000 °C, are reached by the limestone, leading to the thermal decomposition of $CaCO_{3(s)}$ into $CaO_{(s)}$ and $CO_{2(g)}$. The heat necessary for the calcination reaction in limekilns is traditionally generated through the combustion of fossil fuels [6].

The most significant factor influencing quicklime production cost is fuel consumption, which accounts for approximately 50% of the total manufacturing cost [7]. In addition to cost considerations, quicklime production stands out as one of the industrial processes with the highest emissions of $CO_{2(g)}$ [8]. Specifically, during limestone calcination, 785 kg of $CO_{2(g)}$ are emitted per ton of $CaCO_{3(s)}$, and an additional 200–400 kg of $CO_{2(g)}$ are emitted during fuel combustion. This results in a total emission of around 1000–1200 kg of $CO_{2(g)}$ per ton of produced quicklime [7]. As the $CO_{2(g)}$ produced during $CaCO_{3(s)}$ calcination remains constant, the total emitted $CO_{2(g)}$ depends primarily on the fuel consumption efficiency within the limekiln. [7].

For these reasons, studies aiming to improve the calcination process have been undertaken by authors from various countries across the globe, such as Australia [9], China [10,11], Germany [12], India [13] and Indonesia [14]. However, for Brazil, the fifth largest quicklime producer in the world, there is a gap in the literature regarding studies involving energy and exergy analyses of limekilns operating with renewable biofuels.

The energy efficiency of limekilns can be defined as the ratio between the thermal energy required for the calcination reaction and the energy released by the fuel. Vertical limekilns exhibit higher efficiency (approximately 65–77%) compared to rotary ones (about 40–52%) [15]. Moreover, the Vertical Regenerative Parallel Flow type shows the highest efficiency (around 80–90%), despite its recent technological maturity [6]. These energy analyses have inherent limitations since they are considered solely the first law of thermodynamics [16].

Therefore, exergy analyses can overcome these limitations by incorporating both the first and second laws of thermodynamics. Thus, exergy analyses contribute significantly to the diagnostics of thermodynamic processes, providing a broader understanding of a process and its sustainability, and being able to identify specific parameters to improve

the equipment performance, such as irreversibility points, exergy losses, and fuel-saving points [16].

There are studies in the literature in which energy and exergy analyses of limekilns operating with traditional fossil fuels were performed [7,16]. However, works addressing energy and exergy analyses of limekilns operating with renewable biofuels, such as the present study, were not found in the literature. The current authors have recently conducted experimental analyses involving energy and exergy assessments of other types of equipment, including compressed air energy storage systems [17], kraft biomass boilers [18], clinker rotary kilns [19], and specific chemical exergy predictions for biological molecules [20].

In thermal energy production, the burning of fossil fuels corresponds to one of the main sources of greenhouse gas emissions, mainly $CO_{2(g)}$, which can lead to climate change. Additionally, the depletion of fossil fuel deposits can also imply limitations in the future regarding their uses as energy sources [21]. However, in this scenario, the limekilns are heavily dependent on the employment of solid fossil fuels, oil, and natural gas to meet the equipment's energy demand. These three fossil fuels together represent an employment share of around 90% of the types of fuels used in limekilns [22]. Of these fossil fuels, natural gas is the option that results in the lowest greenhouse gas emissions. Nevertheless, natural gas has a high cost compared to other fossil fuels employed in limekilns.

For these reasons, the lime sector has sought to use other fuel types that meet the increasing limitations on atmospheric emissions, greenhouse gases, product quality, and reduction of quicklime production costs. Favorably, with the deployment of renewable biomass fuels, these requirements aforementioned can be satisfactorily met, which makes biomass an attractive solution for use as biofuel in limekilns. Despite this, the utilization of biomass still represents a small portion of around 2% of the fuels utilized in limekilns [22].

Given the preceding points, it can be perceived that there is a lack of literature regarding energy and exergy diagnostic studies of limekilns operating with biofuels. It is in this regard that the current work aims to contribute to the scientific community. Hence, the present paper aims to conduct energy and exergy diagnostics of a vertical annular shaft limekiln operating with producer gas as a renewable biofuel. To attain this objective, technical visits were made to a calcination industry in the state of Minas Gerais, Brazil. In this company, it was investigated *in situ* how its calcination process is realized, and the employment of producer gas was verified as a renewable biofuel derived from the gasification of eucalyptus wood used as raw

CAMARGOS *et al*.: ENERGY AND EXERGY DIAGNOSTICS OF…

Chem. Ind. Chem. Eng. Q. 31 (1) 33−49 (2025)

material. Operational data of the calcination process were collected in the aforementioned industry. The applied methodology employed to undertake the diagnostics of the annular shaft limekiln was based on the first and second laws of thermodynamics and mass, energy, and exergy balances of the equipment. Thus, through the proposed diagnostics, investigations were conducted to assess the energy and exergy efficiencies of the limekiln and the calcination process overall, identify points of exergy loss, analyze potential points for exergy recovery, evaluate destroyed exergy, and examine the energy and exergy content of the equipment flows. The results obtained in this study for the limekiln performing with renewable biofuel were compared with literature results for similar vertical annular shaft limekilns operating with traditional fossil fuels. The Specific Energy Consumption (SEN) obtained from the limekiln operating with producer gas was 4.8 GJ per ton of quicklime produced, with energy (η_{en}) and exergy (η_{en}) efficiencies of 54.6% and 42.2%, respectively. The overall energy ($\eta_{en-overall}$) and exergy ($\eta_{ex-overall}$) efficiencies of the calcination process were 42.0% and 23.6%, respectively. The $SEN_{overall}$ of the calcination process was 7.6 GJ per ton of quicklime produced. It was verified that the usage of producer gas as a biofuel derived from eucalyptus wood is technically feasible, sustainable, and can be a solution to the conventional fossil fuels employed in limekilns. Noteworthy enhancements for both renewable and fossil fuel-powered limekilns encompass the recuperation of energy and exergy. This includes mainly heat recovery from exhaust gases, reduction of thermal losses, and optimization of operational parameters. The performance of the calcination process can be improved through the aforementioned suggestions, leading to potential fuel savings and the subsequent reduction in costs and pollutant gas emissions. In addition to the aforementioned contributions, it is expected that this work can also reduce the lack of energy and exergy diagnostics for limekilns operating in Brazil, the fifth-largest global quicklime producer.

MATERIAL AND METHODS

In this section, the approach utilized for conducting the present study is presented, concerning the characterization of the calcination process, identification of its temperature measurement points, formulation of assumed hypotheses, descriptions of the collected data, and properties of the constituent species of the system.

Limekiln characterization

Technical visits were conducted to a calcination company in Minas Gerais, Brazil, where an on-site examination of a vertical annular shaft limekiln was carried out for its operational characterization.

Fig. 1 depicts the aforementioned annular shaft limekiln, with the control volume (CV) encompassing the equipment in continuous operation. It was considered that the equipment operates in a steady state, with constant inlet and outlet conditions, and without mass accumulation. This assumption is proper and commonly considered by the literature for limekilns similar to the one investigated herein [6,16]. The vertical annular shaft limekiln has a cylindrical shape, height of 22 m, diameter of 3.2 m, and wall thickness of 0.4 m. The inner wall of the limekiln is coated with refractory material.

As shown in Fig. 1, eight mass flows i (m_i) cross the CV, where i represents the substance contained in the flow and is denoted in the subscript as $ls, lm, ls-ub, pg, a, pc, CO_{2\,(g)}-cr$ e sw, representing limestone, quicklime, unburned limestone, producer gas, combustion air, combustion products, $CO_{2(g)}$ released in limestone calcination, and solid waste, respectively. This same nomenclature was also used throughout the current paper to describe a substance contained in a certain flow.

Therefore, as depicted in Fig. 1, a mass flow of limestone (m_{ls}) is introduced at the top of the limekiln, while a mass flow of produced quicklime (m_{lm}) exits simultaneously from the bottom. Due to gravity, limestone (m_{ls}) moves downward and when it reaches the decarbonization temperature in the Calcination Zone it reacts forming CaO$_{(s)}$ and CO$_{2(g)}$. At the bottom of the limekiln, a mass flow of unburnt limestone (m_{ls-ub}) exits, which consist of limestone that does not undergo calcination. A mass flow of producer gas (m_{pg}), the renewable biofuel, is introduced into the Calcining Zone along with a mass flow of combustion air (m_a). In the Calcination Zone, the producer gas distribution system is assembled to feed the biofuel (m_{pg}) through burners, providing the heat of combustion axially and radially in the combustion chamber. In this same region, the combustion air (m_a) is introduced with the assistance of air blowers. In the Cooling Zone, in practice, air is also introduced, which comes into contact with the quicklime in this region, cooling it. As a result, this heated air flows upward in countercurrent with the quicklime bed. This ascending heated air not only aids in biofuel combustion but also preheats the limestone at the top of the limekiln. The cooling air was assumed to be a portion of the combustion air (m_a). From the Preheating Zone, with the aid of an exhauster, a single flow is released: the mass flow of combustion products (m_{pc}) arising from
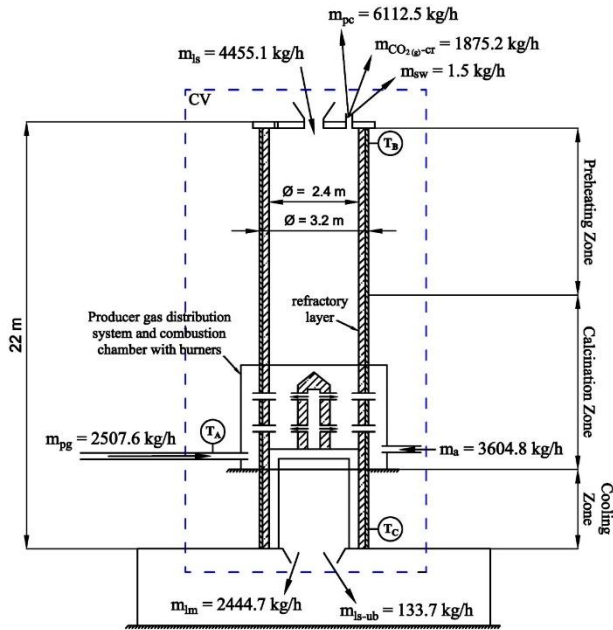
Figure 1. Vertical limekiln.

the burn of the producer gas; the mass flow of $CO_{2(g)}$ ($m_{CO_{2\,(g)}-cr}$) produced from the limestone calcination, and the mass flow of solid waste (m_{sw}) resulting from limestone attrition.

For operational control of the limekiln, the monitoring of three temperatures is performed at specific points as indicated in Fig. 1: temperature A (T_A) is measured at the supply of producer gas; temperature B (T_B) is measured at the limekiln top, and temperature C (T_C) is controlled at the outlet of the quicklime and unburnt limestone flows at the bottom of the equipment.

Data collection

Table 1 presents the collected data provided by the company regarding its calcination process during regular working periods, concerning the quantities of component flows, operational temperatures, and chemical composition of limestone and quicklime. Literature data for the chemical composition of producer gas and eucalyptus wood are also provided to complement the system characterization. Additionally, the data for the specific heat polynomials used in the energy and exergy diagnostics are included. To convert masses of chemical species (m) to their corresponding moles (n), the tabulated molar masses (MM) provided by [23] were utilized.

Temperature characterization

The temperatures (T_i) of the mass flows $i(m_i)$ that cross the limekiln's CV described in Fig. 1 are stated in this subsection. For the mass flow of producer gas (m_{pg}) it

was considered that its temperature (T_{pg}) corresponds to $T_A = 387.2$ °C. Regarding the mass flows of products of combustion (m_{pc}), $CO_{2(g)}$ from calcination ($m_{CO_{2(g)}-cr}$) and solid wastes (m_{sw}) the temperatures T_{pc}, $T_{CO_{2(g)}-cr}$ and T_{sw} were respectively considered, at $T_B = 198.2$ °C. For the mass flows of quicklime (m_{lm}) and unburnt limestone (m_{ls-ub}), the temperatures T_{lm} and T_{ls-ub} were respectively considered, as being $T_C = 60.0$ °C. For the mass flows of limestone (m_{ls}) and combustion air (m_a) the temperatures T_{ls} and T_a were respectively defined, as being at ambient temperature $T_{env} = 25.0$ °C.

Characterization of standard heats of reaction

The chemical species $CaCO_{3(s)}$ and $CaCO_3 \cdot MgCO_{3(s)}$ that constitute the limestone entering the limekiln undergo calcination according to Eqs. (1) and (2), respectively. The standard heats of reaction at 298 K of $CaCO_{3(s)}$ ($\Delta h^\circ_{R-CaCO_{3(s)}}$) and $CaCO_3 \cdot MgCO_{3(s)}$ ($\Delta h^\circ_{R-CaCO_3 \cdot MgCO_{3(s)}}$) were characterized using standard heats of formation (Δh°_{298}) tabulated and reported by literature [24–27]. The chemical species $SiO_{2(s)}$, $Al_2O_{3(s)}$, and $Fe_2O_{3(s)}$ that constitute the limestone are inert.

$$CaCO_{3(s)} \rightarrow CaO_{(s)} + CO_{2(g)}, \tag{1}$$
$$\Delta h^0_{R-CaCO_{3(s)}} = 178491 \; kJ/kmol$$

$$CaCO_{3(s)}MgCO_{3(s)} \rightarrow CaO_{(s)} + MgO_{(s)} + 2CO_{2(g)}, \tag{2}$$
$$\Delta h^0_{R-CaCO_{3(s)}MgCO_{3(s)}} = 302762 \; kJ/kmol$$
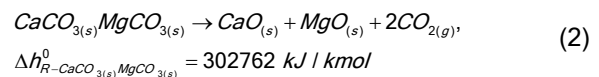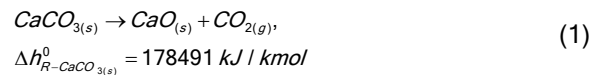
For the producer gas, its constituent chemical species $CH_{4(g)}$, $CO_{(g)}$, and $H_{2(g)}$ undergo combustion according to the chemical reactions expressed by Eqs. (3–5), respectively. The heats of the combustion reaction of $CH_{4(g)}$ ($\Delta h^\circ_{R-CH_{4(g)}}$), $CO_{(g)}$ ($\Delta h^\circ_{R-CO_{(g)}}$), and $H_{2(g)}$ ($\Delta h^\circ_{R-H_{2(g)}}$) were also characterized by employing the Δh°_{298} tabulated and provided by literature [24–27]. The other chemical species that constitute the producer gas, which are $CO_{2(g)}$, and $N_{2(g)}$, do not undergo combustion.

$$CH_{4(g)} + 2O_{2(g)} \rightarrow 2H_2O_{(g)} + CO_{2(g)}, \tag{3}$$
$$\Delta h^0_{R-CH_{4(g)}} = -802625 \; kJ/kmol$$

$$CO_{(g)} + 1/2O_{2(g)} \rightarrow CO_{2(g)}, \tag{4}$$
$$\Delta h^0_{R-CO_{(g)}} = -282984 \; kJ/kmol$$

$$H_{2(g)} + 1/2O_{2(g)} \rightarrow H_2O_{(g)}, \tag{5}$$
$$\Delta h^0_{R-H_{2(g)}} = -241818 \; kJ/kmol$$
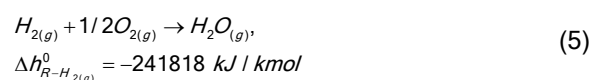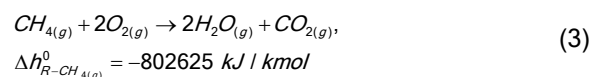
Table 1. Data from the calcination process for the visited company.

COLLECTED DATA			
Flows	Value (kg/h)	Temperature	Value (°C)
Limestone (m_{ls})	4455.1	Temperature A (T_A)	387.2
Quicklime (m_{lm})	2444.7	Temperature B (T_B)	198.2
Unburnt limestone (m_{ls-ub})	133.7	Temperature C (T_C)	60.0
Solid waste (m_{sw})	1.5		
$CO_{2(g)}$ from calcination (m_{CO_2-cr})	1875.2		
Eucalyptus wood (m_{ew})	5147.2		

CHEMICAL COMPOSITION DATA					
Limestone				Quicklime	
Species	Value	Reference	Species	Value	Reference
$CaCO_{3(s)}$	93.35%wt		$CaO_{(s)}$	95.10%wt	
$CaCO_3 \cdot MgCO_{3(s)}$	4.94%wt		$MgO_{(s)}$	1.90%wt	
$SiO_{2(s)}$	1.55%wt	This work	$SiO_{2(s)}$	2.73%wt	This work
$Al_2O_{3(s)}$	0.09%wt		$Al_2O_{3(s)}$	0.15%wt	
$Fe_2O_{3(s)}$	0.07%wt		$Fe_2O_{3(s)}$	0.12%wt	
Producer gas			Eucalyptus wood		
Species	Value	Reference	Species	Value	Reference
$N_{2(g)}$	50.00%vol		C	45.19%wt	
$CO_{(g)}$	14.00%vol		O	48.89%wt	
$H_{2(g)}$	9.00%vol	[37]	H	5.82%wt	[38]
$CO_{2(g)}$	20.00%vol		N	0.10%wt	
$CH_{4(g)}$	7.00%vol		Ash (A)	0.10%wt	
MM_{pg}	28.03 kg/kmol	[39]	LHV_{ew}	18.27 MJ/kg	[40]
LHV_{pg}	2.94 MJ/m³				

SPECIFIC HEAT POLYNOMIAL COEFFICIENTS							
Species	A	B	C	D	E	Validity (K)	Equation
$CaCO_{3(s)}$	12.572	0.002637	0	-312000	-	298-1200	6
$CaCO_3 \cdot MgCO_{3(s)}$	141.5	0.1359	2175000		-	298-650	7
$SiO_{2(s)}$	4.871	0.005365	0	-100100	-	298-847	6
$Al_2O_{3(s)}$	102.4290	38.7498	-15.9109	2.6282	-3.0076	298-2327	6
$Fe_2O_{3(s)}$	11.812	0.009697	0	-197600	-	298-960	6
$CaO_{(s)}$	6.104	0.000443	0	-104700	-	298-2000	6
$MgO_{(s)}$	47.2600	5.6816	-0.8727	0.1043	-1.0540	298-3105	8
$CH_{4(g)}$	1.702	0.009081	-0.000002164	0	-	298-1500	6
$CO_{(g)}$	3.376	0.000557	0	-3100	-	298-2500	6
$H_{2(g)}$	3.249	0.000422	0	8300	-	298-3000	6
$CO_{2(g)}$	5.457	0.001045	0	-115700	-	298-2000	6
$O_{2(g)}$	3.639	0.000506	0	-22700	-	298-2000	6
$N_{2(g)}$	3.28	0.000593	0	4000	-	298-2000	6
$H_2O_{(g)}$	3.47	0.00145	0	12100	-	298-2000	6

Characterization of chemical species constituting the mass flows

Each mass flow i (m_i) that crosses the limekiln's CV, is a mixture of solids or gases constituted by chemical species j. The species j constituting the mass flows of limestone (m_{ls}), quicklime (m_{lm}) and producer gas (m_{pg}) were mentioned in their chemical compositions presented in Table 1. The mass flow of combustion air is composed of the molar proportion of 21% $O_{2(g)}$ and 79% $N_{2(g)}$ since the air inserted is atmospheric. The species j that constitute m_{ls}, also compose the mass flows of unburnt limestone (m_{ls-ub}) and solid waste (m_{sw}) arising from limestone friction. The mass flow of combustion products consists of $CO_{2(g)}$; $O_{2(g)}$; $N_{2(g)}$ and $H_2O_{(g)}$, according to the reactions described in Eqs. (3–5) and considering air excess commonly employed in limekilns.

Specific heat

For the specific heats (Cp_j) of chemical species j constituents of the mass flows (m_i) that cross the limekiln's CV, the characteristic polynomials as a temperature function, characterized by Eqs. (6-8), were considered according to the references indicated [24–26]. The coefficients of these equations for each chemical species are presented in Table 1, as well as their temperature validity ranges and corresponding equations. The mass flow temperatures i (T_i) must be utilized in Kelvin. In Eqs. (7) and (8), the Cp_j output unit is kJ/(kmol·K). In Eq. (6), the Cp_j/R ratio is used by the reference to make the equation dimensionless, and the Cp_j the output unit is the same as the universal gas constant (R) employed in this work, which was 8.31446 kJ/(kmol·K).

$$C_{pj}/R \rightarrow A + BT_i + CT_i^2 + DT_i^3 \qquad (6)\ [24]$$

$$C_{pj} \rightarrow A + BT_i - CT_i^{-2},\ kJ/(kmol \cdot K) \qquad (7)\ [25]$$

$$C_{pj} \rightarrow A + Bt_i + Ct_i^2 + Dt_i^3 + Et_i^{-2},\ kJ/(kmol \cdot K)$$
$$t_i = T_i/1000 \qquad (8)\ [26]$$

CAMARGOS *et al.*: ENERGY AND EXERGY DIAGNOSTICS OF…

Chem. Ind. Chem. Eng. Q. 31 (1) 33–49 (2025)

MATHEMATICAL DESCRIPTION

The data, characterizations, and considerations previously provided were utilized in the mathematical description described separately in the following. Although the procedure employed is for a vertical annular shaft limekiln operating with producer gas as a renewable biofuel, in general, it can be replicated for other types of renewable biofuels and limekilns.

Mass Balance

The limekiln's CV was schematically illustrated in Fig. 2a with the mass flows i (m_i) involved. Limekilns are commonly and properly analyzed in the literature as operating in a steady state, as the equipment works continuously with constant inlet and outlet conditions [6, 16]. So, in Eq. (9), applying the mass conservation principle and considering steady state, it is implied that the sum of input mass flows i (m_{in-CV}) is equivalent to the sum of output mass flows i (m_{out-CV}) in kg/h:
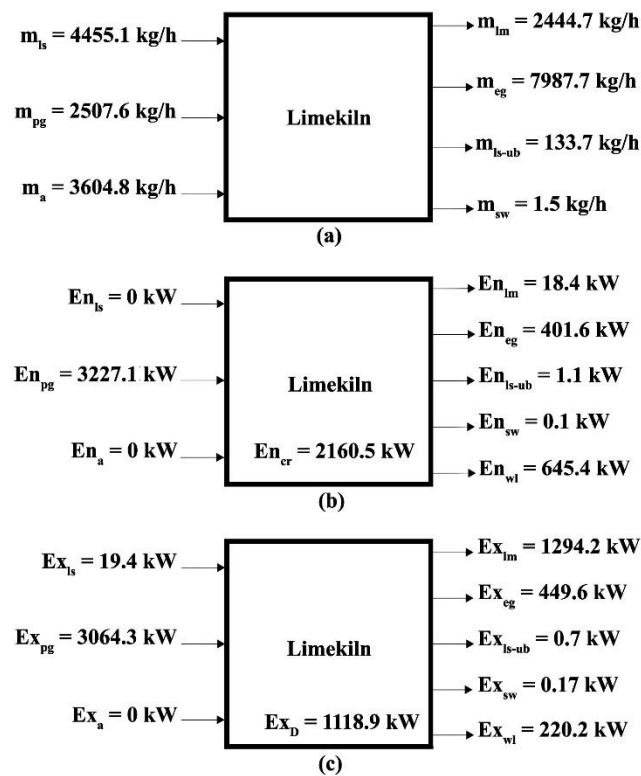
Figure 2. (a) Mass balance; (b) Energy Balance; (c) Exergy balance.

$$\sum m_{in-CV} = \sum m_{out-CV} \tag{9}$$

no mass is accumulated in the CV; therefore, substituting the mass flows (m_i) of the CV in Eq. (9) results in:

$$m_{ls} + m_{pg} + m_a = m_{lm} + m_{eg} + m_{ls-ub} + m_{sw} \tag{10}$$

where the mass flows correspond to limestone (m_{ls}), producer gas (m_{pg}), combustion air (m_a), quicklime (m_{lm}), exhaust gases (m_{eg}), unburnt limestone (m_{ls-ub}) and solid waste (m_{sw}).

The mass flow of exhaust gases (m_{eg}) is characterized by the sum of the mass flows of combustion products (m_{pc}) and $CO_{2(g)}$ generated in calcination ($m_{CO_{2(g)}-cr}$), thus:

$$m_{eg} = m_{pc} + m_{CO_{2(g)}-cr} \tag{11}$$

Each mass flow i (m_i) in Eq. (10) is a mixture of solids or gases composed by the sum of the masses of constituent chemical species j (m_j) characterized in the previous chapter, as follows:

$$m_i = \sum_{j=1}^{p} m_j \tag{12}$$

The evaluation of the combustion air quantity for the producer gas was performed using stoichiometry and considering an excess of air. Thus, initially, based on the combustion reactions of the producer gas characterized by Eqs. (3–5), the stoichiometric number of moles of oxygen ($n_{O_{2(g)}-ST}$) was determined as:

$$n_{O_{2(g)}-ST} = \left(n_{CH_{4(g)}-pg} \cdot 2 + \frac{n_{CO_{(g)}-pg}}{2} + \frac{n_{H_{2(g)}-pg}}{2} \right) \tag{13}$$

in which $n_{CH_{4(g)}-pg}$, $n_{CO_{(g)}-pg}$ and $n_{H_{2(g)}-pg}$ are the mole numbers of the species indicated in the subscripts present in the producer gas, whose percentages for each component were provided in Table 1 and can be expressed in terms of the mole number of the producer gas (n_{pg}) as follows:

$$n_{CH_{4(g)}-pg} = 0.07 n_{pg} \tag{14}$$

$$n_{CO_{(g)}-pg} = 0.14 n_{pg} \tag{15}$$

$$n_{H_{2(g)}-pg} = 0.09 n_{pg} \tag{16}$$

By substituting Eqs. (14–16) into Eq. (13), the expression for $n_{O_{2(g)}-ST}$ becomes:

$$n_{O_{2(g)}-ST} = \left(0.07 n_{pg} \cdot 2 + \frac{0.14 n_{pg}}{2} + \frac{0.09 n_{pg}}{2} \right) \tag{17}$$

And after simplifying, $n_{O_{2(g)}-ST}$ is equivalent to:

$$n_{O_{2(g)}-ST} = 0.255 n_{pg} \tag{18}$$

The air introduced into the limekiln is atmospheric, and it was considered to have a molar composition of 21% $O_{2(g)}$ and 79% $N_{2(g)}$. Therefore, taking this composition into account, the number of mols of stoichiometric air (n_{a-ST}) was evaluated as follows:

$$n_{O_{a-ST}} = \frac{0.255 n_{pg}}{0.21} \tag{19}$$

However, to ensure the complete burning of fuel, it is common to use an air excess. Typical values of excess combustion air employed in limekilns, similar to the one investigated herein, are 5 to 25% [28], 10% [7], and 15 and 32% [16]. The visited company was unable to provide us with the data regarding the quantity of air fed into the limekiln. Thus, based on the characteristics of the limekiln of the industry visited and the literature data aforementioned for analogous limekilns, in this work the excess combustion air was estimated to be 15% of the stoichiometric air. So, the number of moles of air (n_a) fed into the limekiln, considering the 15% excess air, was evaluated as follows:

$$n_a = 1.15 n_{a-ST} \tag{20}$$

Substituting Eq. (19) into Eq. (20) and simplifying, n_a becomes:

$$n_a = 1.15 \frac{0.255 n_{pg}}{0.21} = 1.397 n_{pg} \tag{21}$$

Using the relation $n = m/MM$, Eq. (21) becomes as follows:

$$\frac{m_a}{M \cdot M_a} = 1.397 \frac{m_{pg}}{M \cdot M_{pg}} \tag{22}$$

where the molar mass of atmospheric air (MM_a) of 28.85 kg/kmol and the molar mass of the producer gas of 28.03 kg/kmol given in Table 1 were employed. Therefore, inputting these MM values in Eq. (22), it becomes:

$$m_a = 1.438 \cdot m_{pg} \tag{23}$$

Energy balance

Fig. 2b shows the limekiln's CV with the energy flows i (En_i) involved. In this CV, considering steady state, the sum of input energies $i(En_{in-CV})$ is equivalent to the sum of output energies i (En_{out-CV}) plus the energy required for calcination (En_{cr}), to satisfy the energy conservation principle, as expressed in Eq. (24):

$$\sum En_{in-CV} = \sum En_{out-CV} + En_{cr} \tag{24}$$

and substituting the energy flows (En_i) in Eq. (24) results in:

$$En_{ls} + En_{pg} + En_a = En_{lm} + En_{eg} + En_{ls-ub} + E_{sw} + E_{wl} + En_{cr} \tag{25}$$

in which the energy flows in kW correspond to limestone (En_{ls}), producer gas (En_{pg}), combustion air (En_a), quicklime (En_{lm}), exhaust gases (En_{eg}), calcination (En_{cr}), unburnt limestone (En_{ls-ub}), solid waste (En_{sw}) and wall loss (En_{wl}).

The energy flow of exhaust gases (En_{eg}) is characterized by the sum of the energy flows of combustion products (En_{pc}) and $CO_{2(g)}$ generated in calcination ($En_{CO_{2(g)}-cr}$), as follows:

$$En_{eg} = En_{pc} + En_{CO_{2(g)}-cr} \tag{26}$$

To determine the energy flows i (En_i) corresponding to En_{ls}, En_a, En_{lm}, En_{ls-ub}, $En_{CO_{2(g)}-cr}$, En_{pc} and En_{sw}, in Eq. (27) was used, considering the constituent chemical species j in each flow. The specific heats (Cp_j) of the species and mass flow temperatures (T_i) were presented in Table 1. The reference state temperature (T_0) considered was 298 K. The species molar flows (n_j) was determined through the molar mass conversion mentioned previously.

$$En_i = \sum_{j=1}^{p} \left(\int_{T_0}^{T_i} Cp_j \cdot dT \right) \cdot n_j \tag{27}$$

The calcination reaction energy (En_{cr}) is equivalent to the heats of the reaction of $CaCO_{3(s)}$ ($\Delta h_{R-CaCO_{3(s)}}^{\circ}$) and $CaCO_3 \cdot MgCO_{3(s)}$ ($\Delta h_{R-CaCO_3 \cdot MgCO_{3(s)}}^{\circ}$), defined respectively in Eqs. (1) and (2), multiplied by the molar flows of these chemical species present in the limestone, as follows:

$$En_{cr} = \left(\Delta_{R-CaCO_{3(s)}}^{0} \cdot n_{CaCO_{3(s)}} \right) + \left(\Delta_{R-CaCO_{3(s)}MgCO_{3(s)}}^{0} \cdot n_{CaCO_{3(s)}MgCO_{3(s)}} \right) \tag{28}$$

Values of thermal energy flow lost through the limekiln walls (En_{wl}) are mentioned in the literature as being 4.6 and 9.1% [16], and 9.67 and 14.69% [6] of the available energy. Hence, because of the characteristics of the limekiln investigated herein, En_{wl} was considered to be 20% of the energy provided by the producer gas (En_{pg}), thus:

$$En_{wl} = 0.2 En_{pg} \tag{29}$$

Similar ways to estimate En_{wl} was also performed [7].

CAMARGOS *et al.*: ENERGY AND EXERGY DIAGNOSTICS OF…

Chem. Ind. Chem. Eng. Q. 31 (1) 33–49 (2025)

The energy flow of producer gas (En_{pg}) was calculated through the sum of the heats of combustion of the species j (Δh_{R-j}°) that undergo combustion plus their integrals of Cp_j as a temperature function, and each multiplied by the respective molar flows (n_j), as follows:

$$
\begin{aligned}
En_{pg} = & \left(\Delta_{R-CH_4(g)}^0 + \int_{660.30}^{298.15} Cp_{CH_4(g)} \cdot dT \right) \cdot n_{CH_4(g)} + \\
& \left(\Delta_{R-CO(g)}^0 + \int_{660.30}^{298.15} Cp_{CO(g)} \cdot dT \right) \cdot n_{CO(g)} + \\
& \left(\Delta_{R-H_2(g)}^0 + \int_{660.30}^{298.15} Cp_{H_2(g)} \cdot dT \right) \cdot n_{H_2(g)} + \\
& \left(\Delta_{R-CO_2(g)}^0 + \int_{660.30}^{298.15} Cp_{CO_2(g)} \cdot dT \right) \cdot n_{CO_2(g)} + \\
& \left(\Delta_{R-N_2(g)}^0 + \int_{660.30}^{298.15} Cp_{N_2(g)} \cdot dT \right) \cdot n_{N_2(g)}
\end{aligned}
\tag{30}
$$

In Eq. (30), values for $\Delta h_{R-CH_{4(g)}}^{\circ}$, $\Delta h_{R-CO_{(g)}}^{\circ}$ and $\Delta h_{R-H_{2(g)}}^{\circ}$ were given in Eqs. (3–5), respectively; the species Cp_j polynomials for integral calculation were provided in Table 1; the molar flows of producer gas species (n_j) can be converted to species mass flows (m_j) utilizing MM_j values, and then m_j can be put as a function of the mass flow of producer gas (m_{pg}) employing its chemical composition supplied in Table 1. So, by doing this procedure and then simplifying, Eq. (30) can be transformed into an equation of En_{pg} as a function of m_{pg}, as follows:

$$
En_{pg} = 1.2869 m_{pg}
\tag{31}
$$

The energy flow of combustion products (En_{pc}) was determined through the Eq. (27) principle, for its constituent j species, in this way:

$$
\begin{aligned}
En_{pc} = & \left(\int_{298.0}^{471.4} Cp_{H_2O(g)} \cdot dT \right) \cdot n_{H_2O(g)} + \left(\int_{298.0}^{471.4} Cp_{CO_2(g)} \cdot dT \right) \cdot n_{CO_2(g)} + \\
& \left(\int_{298.0}^{471.4} Cp_{O_2(g)} \cdot dT \right) \cdot n_{O_2(g)} + \left(\int_{298.0}^{471.4} Cp_{N_2(g)} \cdot dT \right) \cdot n_{N_2(g)}
\end{aligned}
\tag{32}
$$

In Eq. (32), Cp_j polynomials were also given in Table 1; through stoichiometry of the combustion reactions described in Eqs. (3–5), the species molar flows of combustion products can be represented as a function of molar flows of producer gas reacting species and combustion air; and then these reacting species molar flows of producer gas and combustion air can be converted to mass flows m_{pg} and m_a employing the chemical compositions given in Table 1, air molar

proportion considered and MM values. Therefore, by doing this procedure in Eq. (32) and then simplifying it, En_{pc} can be put in terms of m_{pg} and m_a, as follows:

$$
En_{pc} = 0.06822 m_{pg} + 0.04014 m_a
\tag{33}
$$

Equation system

A system can be defined by a set of eight equations, Eqs. (10), (11), (23), (25), (26), (29), (31), and (33), having the following eight variables as output data: m_{pg}, m_a, m_{pc}, m_{eg}, En_{pg}, En_{eg}, En_{pc} e En_{wl}, and the remaining variables as input data previously calculated. To solve this equation system, the Solver add-in was employed in Excel software with GRG Nonlinear solution method, multiple starting points, and convergence of $1 \cdot 10^{-10}$. Overall solutions were found.

With all mass and energy flows determined, it was then possible to calculate the exergy balance variables described in the following section.

Exergy balance

The limekiln's CV is presented in Fig. 2c with representation of the exergy flows i (Ex_i) involved. Through an exergy balance, and considering a steady state, the sum of input exergy flows i (Ex_{in-CV}) is equivalent to the sum of output exergy flows i (Ex_{out-CV}), plus the destroyed exergy flow (Ex_D), thus [16,29]:

$$
\sum Ex_{in-CV} = \sum Ex_{out-CV} + Ex_D
\tag{34}
$$

therefore, replacing the exergy flows results in:

$$
Ex_{ls} + Ex_{pg} + Ex_a = Ex_{lm} + Ex_{eg} + Ex_{ls-ub} + Ex_{sw} + Ex_{wl} + Ex_D
\tag{35}
$$

where the exergy flows in kW correspond to limestone (Ex_{ls}), producer gas (Ex_{pg}), combustion air (Ex_a), quicklime (Ex_{lm}), exhaust gases (Ex_{eg}), unburnt limestone (Ex_{ls-ub}), solid waste (Ex_{sw}), wall loss (Ex_{wl}) and destroyed exergy (Ex_D).

In Eq. (35), each exergy flow i (Ex_i) for solid and gas flows corresponds to the sum of their fractions of physical ($Ex_{ph;i}$) and chemical ($Ex_{ch;i}$) exergies i, thus:

$$
Ex_i = Ex_{pi;i} + Ex_{ch;i}
\tag{36}
$$

The physical exergy ($Ex_{ph;i}$) for a flow i of solids or gases was calculated through the sum of physical exergies of constituent chemical species j of that flow,

as follows [29]:

$$Ex_{pi;i} = \sum_{j=1}^{p} \left[(h_j - h_0) - T_0 (s_j - s_0) \right] \cdot n_j \tag{37}$$

in which h_j and s_j are the specific enthalpy and entropy of the chemical species j evaluated at the flow conditions, h_0 and s_0 are the specific enthalpy and entropy of the chemical species j at the dead state, n_j is the molar flow of the chemical species j, and T_0 is the temperature at dead state, which was considered 298 K and 101.325 kPa. In Eq. (37), enthalpy and entropy variations were calculated with Eqs. (38) and (39), respectively, considering specific heat varying with temperature [29]:

$$(h_j - h_0) = \int_{T_0}^{T_i} Cp_j \, dT \tag{38}$$

$$(s_j - s_0) = \int_{T_0}^{T_i} \frac{Cp_j}{T} dT - R \ln \frac{p_i}{p_0} \tag{39}$$

In Eq. (39), the pressure term is assessed solely for gases, and not for liquids and solids. Nevertheless, the system is open and is at reference state pressure (P_0), and the pressure of the flows i (P_i) are equal to P_0. So, the pressure term is negligible for gases since $P_i = P_0$ [29].

The chemical exergies $(Ex_{ch;i})$ for solid flows i were determined as follows [30]:

$$Ex_{ch;i} = \sum_{j=1}^{p} ex_{ch;j} \cdot n_j \tag{40}$$

where the specific chemical exergies $(ex_{ch;j})$ of substances j are tabulated [31].

To determine chemical exergies $(Ex_{ch;i})$ of flows i composed of a mixture of gases j, the following equation was employed [30]:

$$Ex_{ch;i} = \left(\sum_{j=1}^{p} x_j ex_{ch;j} + RT_0 \sum_{j=1}^{p} x_j \ln x_j \right) \cdot n_j \tag{41}$$

in which x_j, R and n_i are, respectively, the mole fraction of chemical species j in the mixture, universal gas constant, and molar flow of the gas mixture i.

The wall heat loss exergy flow (Ex_{wl}) can be estimated to be 0.09 kW/(kg$_{quicklime}$/h) [16].

Energy and exergy efficiencies and specific energy consumption

In calcination companies, the energy efficiency of a limekiln (η_{en}) is conventionally determined by dividing the energy necessary for calcination (En_{cr}) by the product of fuel consumption and the lower calorific value of the fuel [32]. Therefore, considering the producer gas, the energy efficiency of the limekiln was calculated as follows:

$$\eta_{en} = \frac{En_{cr}}{V_{pg} LHV_{pg}} \tag{42}$$

where V_{pg} and LHV_{pg} are the volumetric consumption and lower calorific value of the producer gas, respectively.

On the other hand, when considering the gasification of eucalyptus wood into producer gas, the overall energy efficiency $(\eta_{en-overall})$ of the calcination process was assessed based on the energy provided by the eucalyptus wood:

$$\eta_{en-overall} = \frac{En_{cr}}{m_{ew} LHV_{ew}} \tag{43}$$

in which m_{ew} and LHV_{ew} are the mass flow and lower calorific value of the eucalyptus wood, respectively.

The exergy efficiency of the limekiln (η_{ex}) was determined as follows [16]:

$$\eta_{ex} = \frac{Ex_{ch;lm}}{Ex_{pg}} \tag{44}$$

where $Ex_{ch,lm}$ is the chemical exergy of the quicklime and Ex_{pg} is the exergy of producer gas consumed by the limekiln.

Similar to the approach employed for the overall energy efficiency, the overall exergy efficiency $(\eta_{ex-overall})$ of the calcination process was calculated as follows:

$$\eta_{ex-overall} = \frac{Ex_{ch;lm}}{Ex_{ew}} \tag{45}$$

in which Ex_{ew} is the exergy flow of eucalyptus wood consumed in the calcination process. The physical exergy part of the eucalyptus wood $(Ex_{ph;ew})$ is negligible as it is at dead state temperature, and the fraction of chemical exergy of the eucalyptus wood $(Ex_{ch;ew})$ was determined based on its chemical composition, specifically for dry biomass, in kW [33]:

$$Ex_{ch;ew} = \left(\begin{array}{l} 1812.5 + 295.606C + \\ 587.354H + 17.506O + 17.735N - 31.8A \end{array} \right) \cdot m_{ew} \tag{46}$$

where C, H, O, N, and A are the percentages of carbon,

hydrogen, oxygen, nitrogen, and ash, respectively, that constitute the eucalyptus wood.

The specific energy consumption of the limekiln (SEN), which characterizes the amount of fuel energy consumed per ton of produced quicklime (m_{lm}), was determined as follows [6]:

$$SEN = \frac{v_{pg}LHV_{pg}}{m_{lm}} \qquad (47)$$

And the overall specific energy consumption ($SEN_{overall}$) of the calcination process was assessed, taking into account the energy consumption from eucalyptus wood, in this way:

$$SEN_{overall} = \frac{m_{ew}LHV_{ew}}{m_{lm}} \qquad (48)$$

RESULTS AND DISCUSSIONS

In this chapter, the outcomes of mass, energy, and exergy balances obtained for the investigated limekiln's CV, referred to as "Kiln 1", which operates with producer gas as a renewable biofuel derived from eucalyptus wood gasification, are presented and discussed.

These results obtained for Kiln 1 were primarily compared with findings from two similar vertical annular shaft limekilns that operate using non-renewable fossil fuels. These two limekilns, designated as Kiln 2 and Kiln 3, were investigated by [16] and [34], respectively, and utilize oil and lignite dust as non-renewable fossil fuels. Moreover, other literature data for analogous vertical annular shaft limekilns were also compared with the Kiln 1 investigated herein, in which case the citations were provided accurately.

Literature data were presented as provided by the references, and with temperatures standardized in degrees Celsius. The operational data of limekilns of the same type vary even among literature data. This occurs due to, for example, differences in local temperature, control systems, chemical compositions of limestone, quicklime, and the fuel, and substance flow rates. Thus, the comparisons made in this work were generally made in specific terms and are similar to those made in the literature [6,16], and were not intended to affirm that one fuel is better than another in terms of energy or exergy. The comparisons were made in this work to verify that the methodology used is feasible and capable of providing operational data from a company using locally available sustainable biofuel as a substitute for traditional fossil fuels.

Mass balance results

Table 2 shows the results of mass flows and by percentage of constituent chemical species for Kiln 1. It can be seen that the sum of input mass flows in Kiln 1 (m_{in-CV}) is equivalent to the sum of output mass flows (m_{out-CV}), according to the mass conservation principle presented in Eq. (9).

From Table 2, it is noted that Kiln 1 operates with a proportion of 0.767 kg of CO_2 from calcination per kg of quicklime produced. This same parameter is commonly reported in the literature for the characterization of calcination processes, with typical values of 0.751 [35], 0.786 [6], and 0.783–0.786 [36] kg of CO_2 per kg of quicklime produced. These data are in accordance with the result achieved for Kiln 1.

Considering the total amount of CO_2 emitted, including the calcination and fuel combustion, Kiln 1 works with an emission ratio of 1.427 kg of CO_2 per kg of quicklime produced. This parameter is also traditionally reported in the literature as a specification of calcination processes. This result for the total quantity of CO_2 emitted per kg of quicklime produced attained in Kiln 1, is also in consonance with literature results with values of 1.092 [35], 1.113–1.129 [36], 1.221–1.401 [6] kg of CO_2 per kg of quicklime produced. These emission ratios were not reported for Kilns 2 and 3 by the literature.

As previously mentioned, note that limekiln specifications can vary from one literature source to another. This occurs, for example, due to differences in local temperatures, control systems, limekiln design, chemical compositions of the limestone, quicklime, and the fuel, and substances flow rates.

Energy balance results

In Table 3, the results of energy flows and in terms of chemical species percentage for Kiln 1 were presented. As indicated in Eq. (24), it is noted that the sum of energy flows entering CV (En_{in-CV}) is equivalent to the sum of energy flows leaving CV (En_{out-CV}) plus the energy required for calcination (En_{cr}), thus satisfying the energy conservation principle.

Note that of the total input energy flow provided by the producer gas, this is mostly distributed to the limestone calcination (En_{cr}). This was expected because limestone calcination is an industrial process that requires a large amount of energy [16].

The exhaust gases, which include En_{pc} and $En_{CO_{2(g)}-cr}$, have a considerable energy content released into the atmosphere, and are therefore wasted. Hence, the heat from the exhaust gases of Kiln 1 could be recovered. This could be achieved with the implementation of a recirculation system directing the gases into the limekiln. Doing so would preheat the

Table 2. Kiln 1 mass balance results.

Input		Output	
Mass flow (kg/h)	Chemical species mass (%)	Mass flow (kg/h)	Chemical species mass (%)
$m_{ls} = 4455.1$	$m_{CaCO_{3(s)}} = 0.9335 \cdot m_{ls}$ $m_{CaCO_3 \cdot MgCO_{3(s)}} = 0.0494 \cdot m_{ls}$ $m_{SiO_{2(s)}} = 0.0155 \cdot m_{ls}$ $m_{Al_2O_{2(s)}} = 0.0009 \cdot m_{ls}$ $m_{Fe_2O_{2(s)}} = 0.0007 \cdot m_{ls}$	$m_{pc} = 6112.5$	$m_{H_2O_{(g)}} = 0.0607 \cdot m_{pc}$ $m_{CO_{2(g)}} = 0.2641 \cdot m_{pc}$ $m_{O_{2(g)}} = 0.0179 \cdot m_{pc}$ $m_{N_{2(g)}} = 0.6573 \cdot m_{pc}$
$m_a = 3604.8$	$m_{O_{2(g)}} = 0.2329 \cdot m_a$ $m_{N_{2(g)}} = 0.7671 \cdot m_a$	$m_{CO_{2(g)}-cr} = 1875.2$	-
$m_{pg} = 2507.6$	$m_{N_{2(g)}} = 0.4996 \cdot m_{pg}$ $m_{CO_{(g)}} = 0.1399 \cdot m_{pg}$ $m_{H_{2(g)}} = 0.0065 \cdot m_{pg}$ $m_{CO_{2(g)}} = 0.3140 \cdot m_{pg}$ $m_{CH_{4(g)}} = 0.0401 \cdot m_{pg}$	$m_{sw} = 1.5$	$m_{CaCO_{3(s)}} = 0.0717 \cdot m_{sw}$ $m_{CaCO_3 \cdot MgCO_{3(s)}} = 0.5645 \cdot m_{sw}$ $m_{SiO_{2(s)}} = 0.1581 \cdot m_{sw}$ $m_{Al_2O_{2(s)}} = 0.1457 \cdot m_{sw}$ $m_{Fe_2O_{2(s)}} = 0.0599 \cdot m_{sw}$
		$m_{lm} = 2444.7$	$m_{CaO_{(s)}} = 0.9510 \cdot m_{lm}$ $m_{MgO_{(s)}} = 0.0190 \cdot m_{lm}$ $m_{SiO_{2(s)}} = 0.0273 \cdot m_{lm}$ $m_{Al_2O_{2(s)}} = 0.0015 \cdot m_{lm}$ $m_{Fe_2O_{2(s)}} = 0.0012 \cdot m_{lm}$
		$m_{ls-ub} = 133.7$	$m_{CaCO_{3(s)}} = 0.9335 \cdot m_{ls-ub}$ $m_{CaCO_3 \cdot MgCO_{3(s)}} = 0.0494 \cdot m_{ls-ub}$ $m_{SiO_{2(s)}} = 0.0155 \cdot m_{ls-ub}$ $m_{Al_2O_{2(s)}} = 0.0009 \cdot m_{ls-ub}$ $m_{Fe_2O_{2(s)}} = 0.0007 \cdot m_{ls-ub}$
$m_{in-CV} = 10567.5$		$m_{out-CV} = 10567.5$	

Table 3. Kiln 1 energy balance results.

Input		Output	
Energy flow (kW)	Chemical species energy (%)	Energy flow (kW)	Chemical species energy (%)
$En_{ls} = 0$	$En_{CaCO_{3(s)}} = 0$ $En_{CaCO_3 \cdot MgCO_{3(s)}} = 0$ $En_{SiO_{2(s)}} = 0$ $En_{Fe_2O_{2(s)}} = 0$ $En_{Al_2O_{2(s)}} = 0$	$En_{pc} = 315.8$	$En_{H_2O_{(g)}} = 0.1073 \cdot En_{pc}$ $En_{CO_{2(g)}} = 0.2340 \cdot En_{pc}$ $En_{O_{2(g)}} = 0.0159 \cdot En_{pc}$ $En_{N_{2(g)}} = 0.6427 \cdot En_{pc}$
$En_a = 0$	$En_{O_{2(g)}} = 0$ $En_{N_{2(g)}} = 0$	$En_{CO_{2(g)}-cr} = 85.8$	-
$En_{pg} = 3227.1$	$En_{N_{2(g)}} = 0.0415 \cdot En_{pg}$ $En_{CO_{(g)}} = 0.3168 \cdot En_{pg}$ $En_{H_{2(g)}} = 0.1752 \cdot En_{pg}$ $En_{CO_{2(g)}} = 0.0249 \cdot En_{pg}$ $En_{CH_{4(g)}} = 0.4415 \cdot En_{pg}$	$En_{sw} = 0.1$	$En_{CaCO_{3(s)}} = 0.0662 \cdot En_{sw}$ $En_{CaCO_3 \cdot MgCO_{3(s)}} = 0.6265 \cdot En_{sw}$ $En_{SiO_{2(s)}} = 0.1332 \cdot En_{sw}$ $En_{Al_2O_{2(s)}} = 0.1310 \cdot En_{sw}$ $En_{Fe_2O_{2(s)}} = 0.0431 \cdot En_{sw}$
		$En_{lm} = 18.4$	$En_{CaO_{(s)}} = 0.9468 \cdot En_{lm}$ $En_{MgO_{(s)}} = 0.0234 \cdot En_{lm}$ $En_{SiO_{2(s)}} = 0.0272 \cdot En_{lm}$ $En_{Al_2O_{2(s)}} = 0.0016 \cdot En_{lm}$ $En_{Fe_2O_{2(s)}} = 0.0010 \cdot En_{lm}$
		$En_{ls-ub} = 1.1$	$En_{CaCO_{3(s)}} = 0.9209 \cdot En_{ls-ub}$ $En_{CaCO_3 \cdot MgCO_{3(s)}} = 0.0639 \cdot En_{ls-ub}$ $En_{SiO_{2(s)}} = 0.0138 \cdot En_{ls-ub}$ $En_{Al_2O_{2(s)}} = 0.0008 \cdot En_{ls-ub}$ $En_{Fe_2O_{2(s)}} = 0.0005 \cdot En_{ls-ub}$
		$En_{wl} = 645.4$	-
		$En_{cr} = 2160.5^*$	$\Delta H^{\circ}_{R-CaCO_{3(s)}} = 0.9535 \cdot En_{cr}$ $\Delta H^{\circ}_{R-CaCO_3 \cdot MgCO_{3(s)}} = 0.0465 \cdot En_{cr}$
$En_{in-CV} = 3227.1$		$En_{out-CV} + En_{cr} = 3227.1$	

limestone entering the equipment at ambient temperature, contributing to its calcination. Consequently, this could reduce the consumption of producer gas. This gas recirculation technology is commonly used in the lime sector [15], however the visited company lacks this equipment.

In Fig. 3, a Sankey diagram comparison of energy flow results for Kilns 1, 2, and 3 was made. It is perceived that the limestone and combustion air energy input flows in Kiln 1 were considered insignificant, as both flows are at ambient temperature. Similarly, in Kilns 2 and 3 the limestone and combustion air input energies represent insignificant fractions, with a maximum of 1.1% for combustion air energy in Kiln 3.

The fuel energy flow corresponds to the majority fraction of the sum of energies entering the three limekilns. In Kiln 1, the producer gas energy corresponds to 100%, being, therefore, in accordance with the fossil fuels percentages, oil, and lignite dust, used in Kilns 2 and 3, respectively, 98.2 and 98.4%.

Regarding the output flows, the energy of exhaust gases is 12.4% of the sum of input energies in Kiln 1, while for Kilns 2 and 3 it is equivalent to 29.3% and 23.2%, respectively. It can be noted that the higher the output temperature of the exhaust gases, the greater the energy wasted in this flow. This is evidenced because the Kiln 2 operates with the highest output temperature (455.0 °C) and fraction of exhaust gases energy (29.3%), while the Kiln 1 investigated herein works with the lowest values of these parameters, 198.2 °C and 12.4%, respectively.

In Kiln 1, the quicklime energy corresponds to 0.6%, being similar to 0.6% in Kiln 3, while in Kiln 2 it represents 4.8%. It is observed that in Kiln 2, the quicklime leaves the equipment at a considerably higher temperature (277.0 °C) compared to Kilns 1 (60.0 °C) and 3 (35.0 °C), which results in a significant waste of 4.8% of the energy supplied.

The wall loss energy corresponds to 20.0% in Kiln 1, being higher than in Kiln 2 (9.1%) and Kiln 3 (4.6%). In Kiln 1, the solid waste and unburnt limestone energies have the lowest energy fractions, being 0.002% and 0.03%, respectively. These two results are also consistent with Kilns 2 and 3, as they were disregarded.

As in Kiln 1, in Kilns 2 and 3 the energy content of the exhaust gases could be recovered through the gas recirculation system mentioned in this section. The heat recovered from the exhaust gases can contribute to limestone calcination and reduce fuel consumption and manufacturing cost. In this way, according to Eq. (42), the energy efficiency (η_{en}) can be increased. Another

option to further improve the energy efficiency of the limekilns would be to apply an operational control method to find optimal operational values of variables such as the exhaust gas and quicklime output temperatures. This type of operational control method was also employed by [32] for operational variables of a vertical industrial limekiln, achieving reductions in fuel and raw material consumption and environmental impacts, in addition to improving the quality of the quicklime.

In the Sankey diagrams shown in Fig. 3, it can be seen that the energy required for calcination corresponds to the largest portion of the total input energy, being 66.9% in Kiln 1, similar to Kiln 3 with 71.6%, while in Kiln 2 it was 56.8%. The suitability of the methodology applied in this work can be perceived through the consistency of the results achieved for Kiln 1 investigated herein with those of Kilns 2 and 3 in the literature.
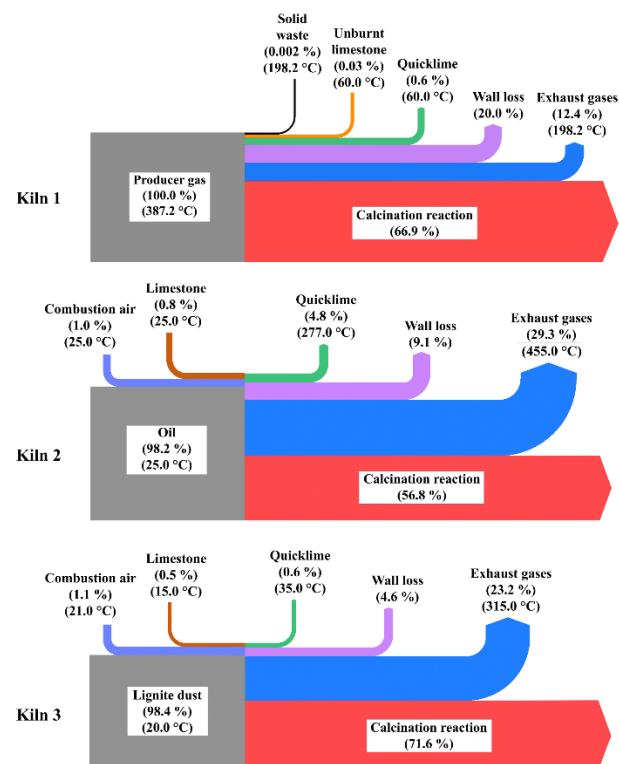
Figure 3. Energy Sankey diagrams for the kilns.

Exergy balance results

Table 4 shows the results achieved for exergy flows of the CV of Kiln 1, and the contributions of physical and chemical exergies in each flow. The temperatures and percentages of the exergy of each flow were also presented in relation to the total exergy entering the equipment. It can be seen that Eq. (34) is being satisfied because the sum of exergy flows entering CV (Ex_{in-CV}) corresponds to the sum of exergy flows leaving it (Ex_{out-CV}) plus the destroyed

Table 4. Kiln 1 exergy balance results.

	Input					Output				
Flow	T (°C)	Ex_{ph} (kW)	Ex_{ch} (kW)	Ex (kW)	%total	Flow	T (°C)	Ex_{ph} (kW)	Ex_{ch} (kW)	Ex (kW)	%total
Ex_{ls}	25.0	0	19.4	19.4	0.6	Ex_{lm}	60.0	1.0	1293.2	1294.2	42.0
Ex_a	25.0	0	0	0	0	Ex_{eg}	198.2	86.1	363.5	449.6	14.6
Ex_{pg}	387.2	107.2	2957.1	3064.3	99.4	Ex_{wl}	-	-	-	220.2	7.1
						Ex_{sw}	198.2	0.02	0.15	0.17	0.01
						Ex_{ls-ub}	60.0	0.1	0.6	0.7	0.02
						$Ex_D{}^a$				1118.9	36.3
Ex_{in-CV}	-	107.2	2976.6	3083.8	100.0	$Ex_{out-CV} + Ex_D$		87.2	1657.4	3083.8	100.0

exergy flow (Ex_D).

Fig. 4 shows a Sankey Diagram comparison of the results of exergy flows obtained in Kilns 1, 2, and 3. The temperature and percentages of physical and chemical exergies in each flow were also presented. Eq. (34) is being satisfied in all limekilns, where the exergies that enter these, are equivalent to the exergies that leave plus the destroyed exergy.

Analyzing Table 4 and Fig. 4, it is noted that the highest physical exergy content, which is recoverable, is related to the exhaust gas output flow in the three limekilns. The amount of physical exergy of quicklime is low compared to its chemical exergy in the three kilns. This reinforces the importance of implementing a gas recirculation system and the application of the operational control method for optimal values of variables, such as the exhaust gas output temperature. The recovery of physical exergy from exhaust gases and quicklime can support limestone calcination and reduce fuel consumption, and according to Eq. (44), increase the exergy efficiency (η_{ex}) of limekilns.

As shown in Fig. 4, the limestone exergy flow has no physical exergy fraction in all kilns, as this flow is at dead state temperature. Therefore, the limestone chemical exergy portion corresponds to its total exergy, being 0.6%, 5.6%, and 6.1% of the sum of input exergies, in Kilns 1, 2, and 3, respectively.

The combustion air exergy represents the smallest contribution of the sum of input exergies in all limekilns. In Kiln 1, the physical and chemical exergies of combustion air were disregarded because the air is atmospheric under dead state conditions. Similarly, the combustion air physical exergy is negligible in Kiln 3 and zero in Kiln 2. In Kilns 2 and 3, combustion air exergies have contributions of 1.7% and 3.3%, respectively.

The fuel exergy flow corresponds to the largest contribution of the sum of input exergies in all limekilns. In Kiln 1, the producer gas exergy, the renewable biofuel, has a contribution of 99.4%, comprised mostly of 96.5% of chemical exergy. Similarly, the fossil fuel exergies in Kilns 2 and 3 are equivalent to 92.7% and 90.6%, respectively, being composed solely of chemical exergy.

As seen in Fig. 4, for output flows, the quicklime exergy is mainly comprised of chemical exergy and has contributions of 42.0%, 38.1%, and 41.0% in Kilns 1, 2, and 3, respectively, in relation to total input exergy.

The exhaust gas exergies correspond to similar percentages of 14.6%, 14.3%, and 11.2% in Kilns 1, 2, and 3 respectively. In Kilns 2 and 3, the exhaust gas exergies have contributions of 45.6% and 45.9% of chemical exergy, respectively, and 54.4% and 54.1% of physical exergy, respectively. Conversely, the exhaust gas exergy in Kiln 1 has a 19.1% contribution of physical exergy and 80.9% of chemical exergy. Kiln 1 operates with exhaust gases at considerably a lower temperature (198.2 °C) compared to Kiln 2 (455.0 °C) and 3 (315.0 °C), so, understandably, Kiln 1 has a lower contribution of physical exergy.

The wall loss exergies have similar percentages of 7.1%>, and 1.3% in Kilns 1, 2, and 3, respectively. The unburnt limestone and solid waste exergies in Kiln 1 have insignificant contributions of 0.02% and 0.01%, respectively, and in Kilns 2 and 3 they were disregarded.

Through the exergy balance expressed in Eq. (34), the sum of output exergies from Kilns 1, 2, and 3 has similar percentages of respectively 63.7%, 58.5%, and 53.5% of the sum of input exergies. Consequently, the destroyed exergy corresponds to the remaining fraction of total input exergy, being 36.3%, 41.5% and 46.5% in Kilns 1, 2, and 3, respectively. The destroyed exergy is inherent to the characteristic irreversibilities of real thermodynamic processes according to the second law of thermodynamics. Examples of sources of irreversibilities in limekilns are the chemical reactions of combustion and calcination, and heat transfer processes in the equipment [16]. As can be seen, the destroyed exergy in Kiln 1 investigated herein was 5.2% and 10.2% lower than in Kilns 2 and 3 of the literature, respectively.

In Fig. 4, it is perceived that the total input exergy in Kiln 1 is distributed in the following descending order: quicklime exergy (42.0%), destroyed exergy (36.3%), exhaust gases (14.6%), wall loss (7.1%), unburnt

limestone (0.02%) and solid waste (0.01%). Similarly, it can be seen that in Kilns 2 and 3 the total input exergy was mostly distributed in destroyed exergy, which is followed by quicklime, exhaust gases, and wall loss exergies, these three in the same decreasing order obtained in Kiln 1. The correspondence of the results attained for Kiln 1 with Kilns 2 and 3 in the literature, indicates the suitability of the applied analysis methodology for scrutinizing the limekilns.
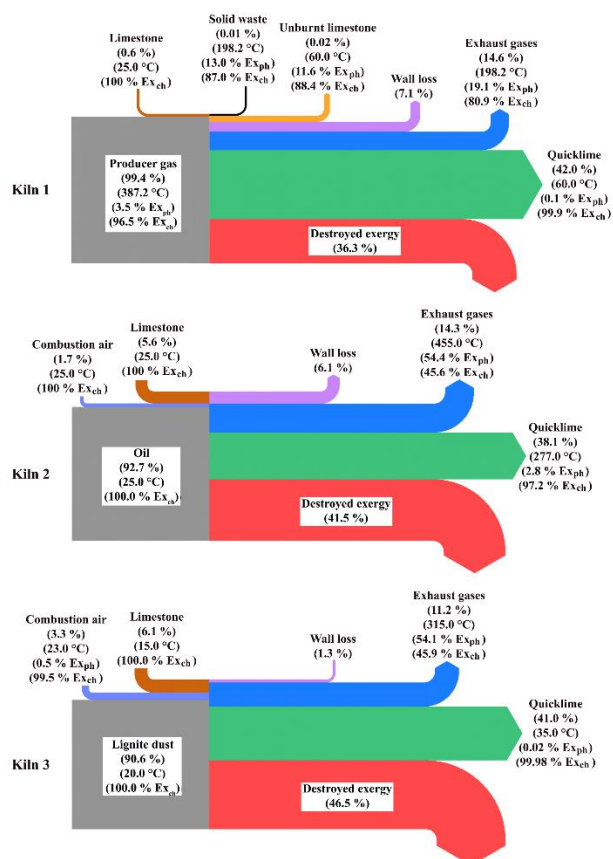
Figure 4. Exergy Sankey diagrams for the kilns.

Efficiencies and SEN results

This section presents the results achieved in the present work and also some found in the literature for similar vertical limekilns. The specific energy (SEN) found in the present study for the Kiln 1 was 4.8 GJ of producer gas energy consumed per ton of quicklime produced, in agreement with the literature SEN values of 4.0–4.8 [15], 4.4 [34], 4.7 [16], and 5.45–5.82 GJ/t [6]. The SEN value of Kiln 1 is in agreement with those of Kilns 2 (4.7 GJ/t) and 3 (4.4 GJ/t), studied by [16] and [34] respectively.

And considering the overall calcination process, the overall specific energy ($SEN_{overall}$) achieved was 7.6 GJ of eucalyptus wood energy consumed per ton of quicklime produced, which is higher than the literature SEN values aforementioned. According to Eqs. (47) and (48), lower SEN values are desirable, as less fuel

energy is consumed to produce quicklime.

Considering the producer gas energy consumption, the energy efficiency (η_{en}) evaluated with Eq. (42) for Kiln 1 was 54.6%, which complies with the η_{en} found for similar limekilns operating with fossil fuels studied in the literature, with values of: 54.68–58.33 [6], 57.8 (Kiln 2) [16], 72.8 (Kiln 3) [34], and 65–77% [15].

Considering the eucalyptus wood energy consumption, the overall energy efficiency ($\eta_{en-overall}$) assessed with Eq. (43 was 42.0%, which is lower than the η_{en} aforementioned by the literature.

When considering the exergy consumption of producer gas, the exergy efficiency (η_{ex}) determined using Eq. (44) for Kiln 1 was 42.2%. This value aligns with η_{ex} values reported in the literature for similar limekilns performing with fossil fuels, such as 40.0 [7], 40.0 (Kiln 2) [16], and 45.3% (Kiln 3) [34].

And considering the eucalyptus wood exergy consumption, the overall exergy efficiency ($\eta_{ex-overall}$), calculated using Eq. (45), was 23.6%, being lower than the η_{ex} mentioned in the literature cited previously.

The efficiency of Kiln 1 using producer gas as a biofuel does not present an advantage compared to the efficiency of limekilns employing traditional fossil fuels. However, the authors emphasize that it was possible to propose a diagnostic of a calcination process of a company where an environmentally friendly biofuel is used with efficiencies close to those of limekilns employing conventional fossil fuels. Additionally, the company reported that the use of sustainable biofuel in its calcination process is due to its low cost compared to fossil fuels, environmental friendliness, and compliance with atmospheric emission limits without impacting the quality of quicklime. The company could not provide us with information regarding the cost of the renewable biofuel used.

In summary, as detailed previously, to enhance the values of SEN, energy efficiency, and exergy efficiency of Kiln 1, which operates with producer gas derived from eucalyptus wood gasification, as well as of other limekilns using fossil fuels, it is essential to emphasize the significance of recovering energy and exergy from exhaust gases and heat wall loss of the equipment. This can be achieved through the implementation of a gas recirculation system, a technique already employed in the quicklime industry. Furthermore, by employing operational control methods for limekiln variables, parameters such as exhaust gas and quicklime output temperatures can be adjusted to optimal values, further enhancing energy and exergy efficiencies, as well as SEN of the limekilns. Additionally, the kinetic energy of the exhaust gases

could be converted into electric energy through the implementation of a turbine-generator system. Thus, this electric energy could be utilized to power the electric equipment of the calcination process, including panels and air blowers.

CONCLUSION

This work conducts energy and exergy diagnostics of a vertical industrial limekiln, which uses producer gas as renewable biofuel produced from eucalyptus wood gasification. Industrial data, coupled with some literature data for equipment characterization, were utilized in these diagnostics. The obtained results were compared with those from similar limekilns using fossil fuels. The Specific Energy Consumption (SEN) for the producer gas-operated limekiln was 4.8 GJ/t$_{quicklime}$, along with energy (η_{en}) and exergy (η_{ex}) efficiencies of 54.6% and 42.2%, respectively. These results align with those found in the literature for analogous limekilns utilizing fossil fuels. In overall terms, the overall energy ($\eta_{en-overall}$) and exergy ($\eta_{ex-overall}$) efficiencies were 42.0% and 23.6% respectively, being lower than literature values. The $SEN_{overall}$ (7.6 GJ/t$_{quicklime}$) was higher than the literature results. To enhance the performance of both renewable biofuel-operated and fossil fuel-operated limekilns, potential areas for energy and exergy recovery were identified. These include mainly recovering heat from exhaust gases, reducing thermal losses through limekiln walls, and deploying operational control methods to adjust variables such as exhaust gas and quicklime temperatures. These findings provide valuable insights for researchers exploring the adoption of renewable biofuels like eucalyptus wood-derived producer gas as alternatives to conventional fossil fuels in limekilns.

ACKNOWLEDGMENT

REFERENCES

[1]   L. Navone, K. Moffitt, K.A. Hansen, J. Blinco, A. Payne, R. Speight, Waste Manage. 102 (2020) 149–160. https://doi.org/10.1016/j.wasman.2019.10.026.

[2]   Y. Liu, H. Shen, J. Zhang, W. Li, J. Liu, B. Liu, S. Zhang, Constr. Build. Mater. 395 (2023) 132292.

[3]   C. Shi, Y. Yang, Mater. 16 (2023) 4026. https://doi.org/10.3390/ma16114026.

[4]   B. Li, F. Min, N. Zhang, J. Ma, Z. Li, Z. Yao, L. Zhang, Constr. Build. Mater. 408 (2023) 133492. https://doi.org/10.1016/j.conbuildmat.2023.133492.

[5]   Statista (2023), Lime production by country in 2022, https://www.statista.com/statistics/657049/production-of-lime-worldwide/ [accessed 20 October 2023].

[6]   V. Alcántara, Y. Cadavid, M. Sánchez, C. Uribe, C. Echeverri-Uribe, J. Morales, J. Obando, A. Amell, Appl. Therm. Eng. 128 (2018) 393–401. https://doi.org/10.1016/j.applthermaleng.2017.09.018.

[7]   A.S. Gutiérrez, C. Vandecasteele, Energy 36 (2011) 2820–2827. https://doi.org/10.1016/j.energy.2011.02.023.

[8]   A. Wolter, W. Fuchs, ZKG Int. 60 (2007) 45–50. https://www.researchgate.net/publication/288154779_Specific_CO2_emissions_and_the_applications_of_lime_burning_kilns.

[9]   E. Smadi, A. Chinnici, B. Dally, G.J. Nathan, Chem. Eng. J. 475 (2023) 146165. https://doi.org/10.1016/j.cej.2023.146165.

[10]   W. Rong, B. Li, F. Qi, S.C.P. Cheung, Appl. Therm. Eng. 119 (2017) 629–638. https://doi.org/10.1016/j.applthermaleng.2017.03.090.

[11]   S. Duan, B. Li, W. Rong, Mater. 15 (2022) 4024. https://doi.org/10.3390/ma15114024.

[12]   M. Greco-Coppi, C. Hofmann, D. Walter, J. Ströhle, B. Epple, Mitig. Adapt. Strateg. Glob. Chang. 28 (2023) 30. https://doi.org/10.1007/s11027-023-10064-7.

[13]   S.A. Jagnade, S.K. Nayak, J.M. Korath, N.N. Viswanathan, P.B. Abhale, Miner. Process. Extr. Metall. 132 (2023) 141–155 https://doi.org/10.1080/25726641.2023.2217403.

[14]   T.S. Febriatna, P.S. Darmanto, F.B. Juangsa, Clean Energy. 7 (2023) 313–327. https://doi.org/10.1093/ce/zkac072.

[15]   H. Piringer, Energy Procedia 120 (2017) 75–95. https://doi.org/10.1016/j.egypro.2017.07.156.

[16]   A.S. Gutiérrez, J.B.C. Martínez, C. Vandecasteele, Appl. Therm. Eng. 51 (2013) 273–280. https://doi.org/10.1016/j.applthermaleng.2012.07.013.

[17]   T.P.L. Camargos, D.L.F. Pottie, R.A.M. Ferreira, T.A.C. Maia, M.P. Porto, Energy 165 (2018) 630–638. https://doi.org/10.1016/j.energy.2018.09.109.

[18]   V.F. Ramos, O.S. Pinheiro, E.F. da Costa Junior, A.O.S. da Costa, Energy 183 (2019) 946–957. https://doi.org/10.1016/j.energy.2019.07.001.

[19]   T.F. Anacleto, A.E.G. O. Silva, S.R. da Silva, E.F. da Costa Junior, A.O.S. da Costa, Braz. J. Chem. Eng. 38 (2021) 197–214. https://doi.org/10.1007/s43153-020-00084-0.

[20]   S.R. da Silva, G. Bonanato, E.F. da Costa Junior, B. Sarrouh, A.O.S. da Costa, Chem. Eng. Sci. 235 (2021) 116462. https://doi.org/10.1016/j.ces.2021.116462.

[21]   M. Höök, X. Tang, Energy Policy 52 (2013) 797–809. https://doi.org/10.1016/j.enpol.2012.10.046.

[22]   European Lime Association (EuLA), Eula Environmental Data Spreadsheet on 2011, Brussels, Belgium (2012).

[23]   WebQC (2023), Chemical Portal, https://www.webqc.org/ [accessed 20 October 2023].

[24]   J.M. Smith, H.C. Van Ness, M.M. Abbott, Introduction to Chemical Engineering Thermodynamics., McGraw Hill (2022). ISBN: 9781260721478.

[25]   C.G. Maier, K.K. Kelley, J. Am. Chem. Soc. 54 (1932) 3243–3246. https://doi.org/10.1021/ja01347a029.

[26]   National Institute of Standards and Technology (2023), Webbook, https://webbook.nist.gov/ [accessed 20 October 2023].

[27]   J.A. Dean, Lange's Handbook of Chemistry, McGraw-Hill, New York (1999). ISBN: 9780070163843.

[28]   H. Shahin, S. Hassanpour, A. Saboonchi, Energy Convers. Manage. 114 (2016) 110–121. https://doi.org/10.1016/j.enconman.2016.02.017.

[29]   Y.A. Cengel, M.A. Boles, Thermodynamics: An Engineering Approach, The McGraw-Hill Companies, New York (2019). ISBN: 9781259822674.

[30]   M.J. Moran, H.N. Shapiro, D.D. Boettner, M.B. Bailey, Fundamentals of engineering thermodynamics, John Wiley & Sons (2018). ISBN: 9781119391388.

[31]   D.R. Morris, J. Szargut, Energy 11 (1986) 733–755. https://doi.org/10.1016/0360-5442(86)90013-7.

[32]   P.A. Ochoa George, A.S. Gutiérrez, J.B. Cogollos Martínez, C. Vandecasteele, J. Cleaner Prod. 18 (2010) 1171–1176. https://doi.org/10.1016/j.jclepro.2010.03.019.

[33]   G. Song, L. Shen, J. Xiao, Ind. Eng. Chem. Res. 50 (2011) 9758–9766. https://doi.org/10.1021/ie200534n.

[34]   H. Piringer, W. Werner, ZKG Int. 61 (2008) 46–52. https://www.researchgate.net/publication/285806720_Conversion_of_large-diameter_single_shaft_kilns_to_lignite_dust_firing_successfully_concluded.

[35]   L. Shen, T. Gao, J. Zhao, L. Wang, L. Wang, L. Liu, F. Chen, J. Xue, Renewable Sustainable Energy Rev. 34 (2014) 337–349. https://doi.org/10.1016/j.rser.2014.03.025.

[36]   B. Jiang, D. Xia, B. Yu, R. Xiong, W. Ao, P. Zhang, L. Cong, J. Cleaner Prod. 240 (2019) 118147. https://doi.org/10.1016/j.jclepro.2019.118147.

[37]   N. Couto, A. Rouboa, V. Silva, E. Monteiro, K. Bouziane, Energy Procedia 36 (2013) 596–606. https://doi.org/10.1016/j.egypro.2013.07.068.

[38]   B.L.C. Pereira, A. de C.O. Carneiro, A.M.M.L. Carvalho, J.L. Colodette, A.C. Oliveira, M.P.F. Fontes, BioResources 8 (2013) 4574–4592. https://doi.org/10.15376/biores.8.3.4574-4592.

[39]   K. Sasujit, N. Homdoung, N. Tippayawong, Energy Eng. 119 (2022) 2149–2167. https://doi.org/10.32604/ee.2022.022069.

[40]   T. de P. Protásio, M.V. Scatolino, A.C.C. de Araújo, A.F.C.F. de Oliveira, I.C.R. de Figueiredo, M.R. de Assis, P.F. Trugilho, Bioenergy Res. 12 (2019) 626–641. https://doi.org/10.1007/s12155-019-10004-x.

CAMARGOS *et al.*: ENERGY AND EXERGY DIAGNOSTICS OF…

Chem. Ind. Chem. Eng. Q. 31 (1) 33−49 (2025)

TOMÁS PESSOA LONDE CAMARGOS[1]

ANDRÉA OLIVEIRA SOUZA DA COSTA[1,2]

ESLY FERREIRA COSTA JUNIOR[1,2]

[1]Graduate Program in Mechanical Engineering, Federal University of Minas Gerais, Belo Horizonte – Minas Gerais, Brazil

[2]Graduate Program in Chemical Engineering, Federal University of Minas Gerais, Belo Horizonte – Minas Gerais, Brazil

NAUČNI RAD

ENERGETSKA I EKSERGETSKA DIJAGNOSTIKA INDUSTRIJSKE ŠAHTNE PEĆI ZA PEČENJE KREČA NA PROIZVODNI GAS KAO OBNOVLJIVIM BIOGORIVOM

Živi kreč, globalno značajna roba koja se koristi u različitim industrijskim aplikacijama, proizvodi se u krečnim pećima koje zahtevaju značajnu energiju, tradicionalno, iz fosilnih goriva. Međutim, zbog rastućih ograničenja emisija i iscrpljivanja naslaga fosilnih goriva, industrija živog kreča istražuje alternativna goriva, kao što je biomasa. U literaturi nedostaju dijagnostičke studije izvodljivosti za krečne peći koje koriste alternativna goriva iz biomase. Stoga, ovaj rad ima za cilj da sprovede energetsku i eksergijsku dijagnostiku industrijske krečne peći koje koristi proizvodni gas dobijen iz drveta eukaliptusa kao obnovljivo biogorivo. Koristeći industrijske podatke i principe termodinamike, korišćena oprema je okarakterisana, a rezultati su upoređeni sa literaturnim nalazima za slične krečne peći koje koriste fosilna goriva. Specifična potrošnja energije za krečnu peć na proizvodni gas je bila 4,8 GJ/t kreča, sa energetskom i eksergijskom efikasnošću od 54,6% i 42,2%. Ukupna energetska i eksergijska efikasnost su bile za 42,0% i 23,6%, redom, niže od literaturnih vrednosti. Ukupna specifična potrošnja energije je bila 7,6 GJ/t kreča i većaše literaturnih vrednosti. Identifikovana poboljšanja za krečne peći na obnovljiva i fosilna goriva uključuju povraćaj energije i eksergija, uključujući povraćaj toplote iz izduvnih gasova, minimiziranje toplotnih gubitaka i optimizaciju operativnih varijabli. Ovi nalazi nude dragocene uvide za istraživače koji istražuju usvajanje obnovljivih biogoriva, kao što je proizvodni gas dobijen iz drveta eukaliptusa, kao alternativa konvencionalnim fosilnim gorivima u krečnim pećima.

Ključne reči: energija, eksergija, krečna peć, živi kreč, biomasa, biogorivo.

49

JASMINA VITAS
ALEKSANDAR JOKIĆ
NATAŠA LUKIĆ
STEFAN VUKMANOVIĆ
RADOMIR MALBAŠA

University of Novi Sad, Faculty
of Technology Novi Sad, Novi
Sad, Serbia

SCIENTIFIC PAPER

MATHEMATICAL MODELING AS A TOOL IN KOMBUCHA BEVERAGES' BIOACTIVE QUALITY CONTROL

Article Highlights

- The total flavonoids content and sensory mark of kombucha beverages were determined
- The influence of temperature, time, and sugars content on flavonoids and sensoric was modeled
- A response surface model to predict the total flavonoids content in the kombucha beverage was created

Abstract

This study examined the application of mathematical models on total flavonoids content and sensory marks of kombucha beverages on winery effluent. Process parameters were as follows: 0, 3, 6, and 9 days of fermentation time; 20, 25, and 30 °C of fermentation temperature and 3, 5, and 7% of initial total reducing sugars. Total flavonoids and sensory marks were determined spectrophotometrically and by a descriptive test and a five-point category scale, respectively. Total flavonoid content decreased during the applied kombucha fermentation process, which lasted for 9 days. On average, the total sensory mark suggested that consumed kombucha products are obtained after 3 days of fermentation, regardless of the fermentation temperature or sugars content. To produce a kombucha beverage with the highest bioactive quality, response surface methodology proposed the following process parameters: 3 days of fermentation, 7% of initial total sugars, and 30 °C process temperature.

Keywords: winery effluent; total flavonoids; kombucha; sensory characteristics; response surface methodology.

Black tea kombucha, a traditional beverage with a sweet and acidic taste, is obtained after kombucha culture fermentation of black tea decoct, sweetened with sucrose. The applied culture is composed of bacteria (mainly acetic acid bacteria) and several yeast species. Kombucha inoculum can metabolically transform a variety of substrates into alternative kombucha beverages. The applied fermentation media include various herbal teas, milk, beer, wine, fruit juices, different types of food industry by-products etc. [1]. In this investigation, black tea kombucha was used as the starter inoculum in the production of winery effluent-based kombucha. Black tea was selected since it relates to traditional kombucha production.

The main constituents of kombucha beverages chemical composition are different organic acids, mainly acetic, sugars, such as sucrose, glucose, and fructose, water-soluble vitamins, ethanol, catalase, invertase, microelements, but various types of polyphenolic compounds as well [1,2].

Flavonoid biosynthesis begins with L-phenylalanine. In the reaction of nonoxidative deamination catalysed by phenylalanine ammonia-lyase, cinnamic acid is produced. This reaction leads to the carbon transfer from the shikimate route to the various parts of the general phenylpropanoid metabolism. A flavan nucleus, which is composed of 15 carbon atoms organized in C6-C3-C6, i.e. A, B, and C

rings represents the main structure of flavonoids [3]. Flavonoids possess health-promoting potential, but they have an impact on sensory characteristics, as well. These compounds are responsible for the bitter taste and tactile sensation of astringency of different types of beverages. Besides flavonoids, the astringency is caused by the presence of organic acids, too. Bitter taste and astringency are usually regarded as unpleasant. Flavonoids have an impact on the color of the product, as well [3]. Flavonoids are known for their pronounced antioxidant activity and ability to prevent and suppress different chronic diseases [4]. It is very well known that sensory properties are the main product characteristics that influence its consumption. Flavonoids are a result of secondary plant metabolism and therefore they are often studied as a part of the chemical composition of kombucha beverages produced using herb-based fermentation media [5–7].

To improve the kombucha fermentation process, perform a scale-up of this process, determine the influence of process parameters on the composition of the final product or to predict the textural characteristics of kombucha fermented milk products, as well as to optimize process conditions to obtain kombucha products with the best antioxidant features, different mathematical models were applied [8–12].

Different mathematical techniques may be used to examine the impact of numerous operational factors, as well as their interactions, on the efficiency of the fermentation process. For example, response surface methodology (RSM) and other experimental designs (e.g., Box-Behnken, Plackett-Burman, Taguchi design, etc.) can be remarkable instruments for maximizing the intended process and describing the individual and combined influence of the independent variables [9]. In kombucha fermentation, numerous studies were conducted to optimize the production. Response surfaces were used to scale up black tea batch fermentation by kombucha [13]. RSM and neural networks were successfully used for modeling of antioxidant characteristics of kombucha-fermented milk beverages with peppermint [12]. Using the Response Surface Methodology (RSM), the effect of fermentation time, sugar concentration, and herbal tea type on the antibacterial activity of Kombucha beverages were analyzed [14].

The aim of this paper was the application of mathematical models to the total flavonoids content and the sensory mark of winery effluent-based kombucha products in favour to determine the production variables that will lead to the kombucha beverage with the highest bioactive quality and to propose a way of quality control of this type of products.

MATERIAL AND METHODS

Initial medium, fermentation media, and process parameters

The initial medium was filtrated and then sterilized winery effluent obtained in the white wine production, after must flotation using gelatin. The plate filter press and the qualitative filter paper were applied for the filtration process. Sterilization was done in an autoclave (121 °C, 20 min). Fermentation media were prepared by the dilution of the initial medium (16.36% of total reducing sugars, 370.22 mg/L of total nitrogen, and 250.00 mg/L of total phosphorus [15]) with boiled tap water to three different sugar levels (3, 5, and 7% of total reducing sugars). The fermentation process was done at three different temperatures (20, 25, and 30 °C) and the samples were collected at the start of the fermentation (day 0), after 3, 6, and 9 days.

Kombucha inoculum

The Kombucha inoculum used in this investigation for the production of novel kombucha products was obtained by three passages of the traditional kombucha inoculum [16,17] on the winery effluent with 7% of total reducing sugars, during 6 days, at 25 °C. Traditional kombucha inoculum was sourced from a local household of a kombucha consumer from the northern region of Serbia. The liquid part of the obtained inoculum was added in the amount of 10% (v/v) to the appropriate fermentation media. Winery effluent was fermented in sterilized glass beakers covered with sterile cheesecloth, in the incubator.

Total flavonoids analysis

Total flavonoids determination was performed using the spectrophotometric method by Markham, with some modifications [18]. Samples in the amount of 7 mL were mixed with 0.3 mL of 5% sodium nitrite solution. After 5 min, 0.3 mL of 10% aluminum chloride hexahydrate was added. After 6 min, 1 mol/L sodium hydroxide in the amount of 1 mL and 1.4 mL of distilled water were added to the mixture. The blank sample was prepared by replacing the sample with distilled water. Absorbance was measured at 510 nm, using the LLG-uni SPEC 2 LLG LABWARE spectrophotometer. Rutin was used as a calibration standard and results were given as rutin equivalents per mL of the sample (µg RE/mL).

Sensory characteristics analysis

Sensory characteristics determination was performed according to [19]. A five-point category scale (5 - the highest and 1 - the lowest) and a descriptive test were applied. Appearance, color, odor, and taste were examined. The qualified evaluators (4 persons)

together with untrained consumers (3 persons) performed the sensory analysis.

Statistical analysis

Response surface methodology (RSM) on Design Expert v10.0.1 (Stat Ease Inc., Minneapolis, USA) was used in this study for regression and graphical analyses of the data. RSM has been discussed in detail elsewhere [12, 20]). Model diagnostics, as well as the optimization capabilities in Design-Expert software, were used to optimize the bioactive quality control of kombucha production, through the mathematical modeling of total flavonoids content. Experimental results are selected for Box-Behnken to evaluate the applicability of RSM as a statistical tool for total flavonoid content. ANOVA was used to assess model adequacy. The design has 15 experiments, with three replications in the center point. In this design, treatment combinations are located in the middle of the process space's edges and the center. In comparison to central composite designs, the designs offer restricted orthogonal blocking capabilities. These designs are rotatable (or almost rotatable), with three levels of each factor. The effects of temperature (20, 25, and 30 °C), initial total sugars (3, 5, and 7%), and time (3, 6, and 9 days) were investigated (Table 1). Selected responses were total flavonoids [μg RE/mL] and total sensory mark (1–5).

RESULTS AND DISCUSSION

Total flavonoids

Results of total flavonoids are presented in Table S1 (Supplementary material).

The initial medium contained 99.4±2.1 μg RE/mL of total flavonoids and this was the highest measured value in this investigation. The results of total flavonoids obtained for the fermentation media indicated that the higher content was related to the higher initial total sugars content and it was in the range from 24.8±0.3 to 51.8±0.5 μg RE/mL.

The total flavonoids content (for products with 7% of initial total sugars content), of samples obtained at 30 and 25°C, was the highest at the beginning of the fermentation (49.1±0.3 μg RE/mL) and the values decreased during the process. For products obtained at 30 °C, the lowest value was measured on the third day of fermentation (31.1±0.7 μg RE/mL). Contents determined on the sixth and ninth days were higher in comparison to the third day. For products obtained at 25 °C, total flavonoids decreased linearly until the sixth day when the lowest value was determined (33.2±0.7 μg RE/mL). After nine days of fermentation,

the value increased by around 18% in comparison to the sixth day. For products obtained at 20 °C, content decreased until the third day of fermentation. A mild increase (for around 9%) was established on the sixth day, in comparison to the third day of the process. The pronounced increase was established at the end of the fermentation (62.6±6.3 μg RE/mL) and the obtained value was 75% higher in comparison to the sixth day.

The total flavonoids content (for products with 5% of initial total sugars content), of samples obtained at 30, 25, and 20°C, was the highest at the beginning of the fermentation (38.3±0.7 μg RE/mL). For products obtained at 30 °C, the content decreased after the ninth day, and the lowest values were measured after the third and the sixth day of the process. The lowest content values were the same and about 17% lower in comparison to the ninth day. For products obtained at 25 °C, the total flavonoids content decreased after the third and the sixth day. On the ninth day, the content increased by 17% when compared to the sixth day. For products obtained at 20 °C, the value decreased after the third day by around 26%. On the sixth day, the value was the same as at the beginning, i.e., it increased by 36% in comparison to the third day. After nine days of fermentation, the value decreased again by around 29% in comparison to the sixth day. The values determined on the ninth and third days were approximately the same.

The total flavonoids content (for products with 3% of initial total sugars content), of samples obtained at 30, and 25°C, was the highest at the start of fermentation (25.4±0.8 μg RE/mL) and the values decreased during the process. For products obtained at 30 °C, total flavonoids content was approximately the same on the third, sixth, and ninth fermentation days. In comparison to the 0 fermentation day, the values determined on the third and sixth day were for around 36%, and after the ninth day for around 32% lower. For products obtained at 25 °C, the content linearly decreased until the sixth day. On the ninth day, the total flavonoids increased by around 11% in comparison to the sixth day. On the other hand, for products obtained at 20 °C, the total flavonoids content was the lowest at the beginning of the process and during the fermentation, the increase in values was established. The value determined on the third day was 100% higher in comparison to the start of the process. Contents measured on the sixth and ninth day were lower when compared to the third day. The determined values decreased after the third and the sixth day. The highest total flavonoids content showed in the sample obtained after three days of the process and it amounted to 50.4±6.8 μg RE/mL.

Of all of the examined variables, process

temperature was the most influential one. The lowest examined (20 °C) was responsible for the highest values of total flavonoids in kombucha products.

Modern literature suggests that bacteria species (*E. coli*, *C. glutamicum*, *L. lactis*, and *Bacillus sp.*) can be applied in flavonoids production [21]. The presence of flavonoids in kombucha products on winery effluent can be related to the applied fermentation medium (winery effluent obtained after must flotation in white wine production), i.e. to the used grapes. Since all of the kombucha products showed lower flavonoids content than the applied fermentation medium, it can be implied that kombucha metabolic activity led to the degradation of flavonoid compounds, probably by the enzymes secreted from kombucha microorganisms [22]. The partial oxidation of flavonoids might lead to the formation of polymerized substances with higher molecular mass [19,5].

Existing literature gives the overview of total flavonoids content in different types of kombucha samples. The majority of papers on kombucha products with plant extracts showed an increase in total flavonoids values as the result of kombucha fermentation. Some investigations showed the opposite trend, as well. These results suggested that the flavonoids content in kombuchas was influenced by

the fermentation process and plant type [5].

Öztürk *et al.* [23] determined the total flavonoids content of traditional (with black tea) and alternative (with hawthorn, hop, and madimak) kombucha products and established that the fermentation process enhanced the flavonoids content, which is opposite to the results obtained in this study. The same trend was recognized by Kilic and Sengun [5], as well. This difference can be related to the fact that Öztürk *et al.* [23] and Kilic and Sengun [5] used higher contents of applied herbs, in comparison to the diluted winery effluent used in this examination. Higher values of total flavonoids in kombucha products were related to sucrose, as the carbon source, and nettle leaves in comparison to honey, as the carbon source, and Anatolian hawthorn [5]. On the other hand, Vitas *et al.* [19] obtained results on total flavonoids that correlated to the ones determined in this study, i.e. the kombucha fermentation also led to a decrease in values.

Modeling of total flavonoids content

The experimental design for process variables and responses is presented in Table 1. Values given in parenthesis are predicted by the selected mathematical model. The design has 15 experiments, with three replications in the center point.

Table 1. Box-Behnken experimental design with three independent factors and the obtained results for total flavonoids content and sensory mark.

Exp.	Factors - Independent variables			Responses - Dependent variables	
	Temperature [°C]	Initial total sugars [%]	Time [days]	Total flavonoids [µg RE/mL]	Total sensory mark
1	20	3	6	37.2 (34.1)	2 (2)
2	20	5	3	28.6 (31.0)	4 (3)
3	20	5	9	27.0 (27.2)	2 (2)
4	20	7	6	36.1 (36.6)	2 (2)
5	25	3	3	23.2 (23.9)	3 (3)
6	25	3	9	21.7 (24.6)	2 (2)
7	25	7	9	38.8 (38.1)	2 (2)
8	25	7	3	44.3 (41.4)	3 (3)
9	30	3	6	15.9 (15.4)	3 (3)
10	30	5	3	22.9 (22.7)	4 (4)
11	30	5	9	26.4 (24.0)	2 (2)
12	30	7	6	40.8 (43.9)	3 (3)
13	25	5	6	24.1 (24.0)	2 (3)
14	25	5	6	23.0 (24.0)	2 (3)
15	25	5	6	24.9 (24.0)	3 (3)

* values in parenthesis are predicted by the selected mathematical model

Design Expert has a number of statistical tables that provide help to model selection for further study. Models that comply with the criteria are highlighted by the software and marked as "suggested". Model summary statistics gives several comparative measures for model selection. Ignoring the aliased model, for total flavonoids content and sensory mark the quadratic and linear models are suggested, respectively.

The experimental data for total flavonoids content

were fitted with the second-degree polynomial equation to create models characterizing the influence of the aforementioned operational parameters on the kombucha fermentation. Table 2 shows the linear (b_1, b_2, b_3), quadratic (b_{11}, b_{22}, b_{33}), and interaction (b_{12}, b_{13}, b_{23}) model coefficients and corresponding p-values.

The obtained results indicate the statistical significance of linear and quadratic effects of initial total sugars. In the regression equation, the interaction between initial total sugars and time is statistically

significant. Temperature linear influence is more pronounced in comparison to the linear influence of time, i.e., corresponding p-values are lower.

Table 2. Coefficients of regression equation for total flavonoids content.

| Effects | Coefficient | | *p*-value |
	Actual	Coded	
Intercept			
b_0	191.3	24.00	<0.0001
Linear			
b_1	-7.057	-2.863	0.05205
b_2	-29.220	7.750	<0.0001
b_3	-2.654	-0.638	0.5964
Quadratic			
b_{11}	0.055	1.362	0.4492
b_{22}	1.784	7.137	0.0077
b_{33}	0.09583	0.863	0.6256
Interaction			
b_{12}	0.650	6.500	0.0096
b_{13}	0.085	1.275	0.4604
b_{23}	-0.167	-1.000	0.5583

A summary of the analysis of variance of the second-degree polynomial model for total flavonoids content is given in Table S2. The model developed for total flavonoids content is significant with a *p*-value of 0.010.

In addition to the high coefficient of the determination value, the proposed second-degree polynomial models had a nonsignificant lack of fit (*p*-value 0.053). Adequate precision is an indicator of signal-to-noise ratio and a ratio greater than 4 is desirable. The ratio of 10.9 has indicated an adequate signal for the response. As a result, these findings suggest that a regression model may be employed to analyze response trends. The impacts of chosen variables on total flavonoids content could be successfully described using a second-degree polynomial model.

Response surface plots were also created to better understand the interactions of independent variables - operating circumstances (temperature, initial total sugars, and time) to total flavonoids content. The response surface plots depict the effects of two independent variables on one response, while the third independent variable's value was fixed to the mean of the tested range of values.

The effects of initial total sugars and temperature are given in Figure 1. As can be seen, total flavonoids content is at maximum value for higher total sugars content. An increase in the initial total sugars increased the total flavonoids content for all selected fermentation temperatures.

On the other hand, the influence of temperature is different at low and high initial total sugars values. At low initial sugar values increase in temperature results in a decrease in the total flavonoids content, whilst at

Figure 1. Response surface plot representing the influence of initial total sugars and temperature on the total flavonoids content.

higher total sugars content increase in temperature results in increased total flavonoids content. Several studies have shown that the microbial spectrum of the kombucha consortium may vary and any change in the fermentation conditions might affect the final product [21]. These findings, i.e. decrease of total flavonoids content suggest that some microbial species in kombucha are involved in the conversion of flavonoids during fermentation; however, more research is needed to determine this [24,25]. The increase in total flavonoids may be caused by the activity of certain microorganisms that can break down the polyphenol compound, as flavonoids may also be produced from other polyphenols. Certain species of lactic acid bacteria have been known to have the capability to degrade polyphenols such as *L. hilgardii* which is frequently found in wine [26,27].

Figure 2 shows the simultaneous influence of time and temperature on the total flavonoids content.

Figure 2. Response surface plot representing the influence of time and temperature on the total flavonoids content.

An increase in temperature results in an insignificant decline of the total flavonoids content for all selected fermentation duration periods. During fermentation, a

slight decrease in total flavonoids was observed at all predetermined temperatures. The highest total flavonoids content showed the samples obtained after three days of the process.

The results of total flavonoids obtained in this study were in accordance with the results obtained in the production of small white apricot wine in which case the highest content (around 40 µg RE/mL) of total flavonoids was determined on the second day of the process [28]. On the other hand, Liang *et al.* [29] determined up to 100 times higher total flavonoids content in green tea-infused white wine. This could be attributed to the applied production process and the addition of green tea. Öztürk *et al.* [23] determined the total flavonoids content as quercetin equivalents in traditional black tea, hawthorn, hop, and madimak-flavored kombucha. The obtained results suggested that the kombucha fermentation process led to the increase in flavonoids content. The madimak flavored kombucha proved to be the superior product because of the used fermentation medium, and not the performed fermentation process. Vitas *et al.* [18] concluded that alternative herb-based kombucha products had higher flavonoids content than traditional tea-based ones. The results obtained by Vitas *et al.* [18] were in accordance with the results of the present study.

The effects of initial total sugars and time are given in Figure 3. Total flavonoids have the highest value for the higher total sugars content. The increase of the initial total sugars increased the total flavonoids content for all predetermined fermentation periods.

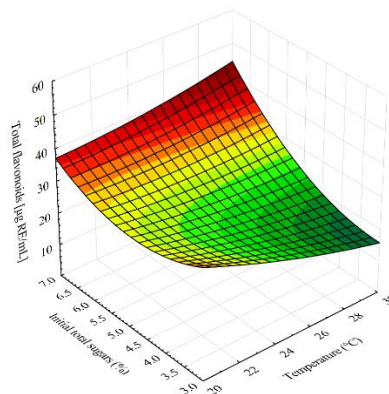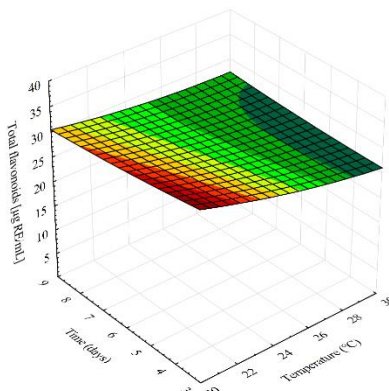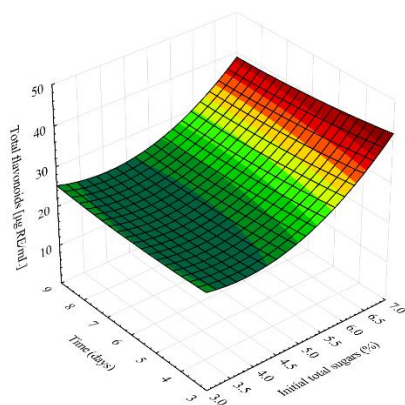*Figure 3. Response surface plot representing the influence of initial total sugars and time on the total flavonoids content.*

During the process of fermentation, total flavonoids did not vary significantly. Similar results were reported for the kombucha fermentation process of green and pu'er teas where no significant changes in the total flavonoids [25].

Sensory mark

Results of the sensory mark are presented in Table S3. It is very well known that the color of the food product suggests the possible taste and the freshness of the products. Odour is related to the behavior in food choice and taste influences the perception of flavor. In food products, flavonoids are usually responsible for the taste and color [30].

Color

Kombucha products obtained from a fermentation medium with 7% of initial total sugars had the highest color mark (5) on the sixth day at 30 °C. This was the only product whose color mark was higher than the sample mark from the fermentation start. The lowest color mark (2) showed products obtained at 25 °C (third and sixth day) and 20 °C (sixth day). The most suitable temperature was 30 °C, and the least favorable temperature was 25 °C.

Kombucha products obtained from a fermentation medium with 5% of initial total sugars had the highest color mark (5) on the sixth day at 30 °C, as well as products with 7% sugars. The lowest color mark (1) had a sample produced at 20 °C. The most suitable temperature was 30 °C, and the least favorable temperature was 20 °C. Products obtained at 30 °C (sixth and ninth day) and the sample produced at 25 °C (ninth day) had a higher color mark than the sample from the fermentation start.

Kombucha products obtained from a fermentation medium with 3% of initial total sugars had the highest color mark (4) on the sixth day at 30 °C, as well as products with 7 and 5% sugars. The lowest color mark (1) showed products obtained at 25 °C (sixth day) and 20 °C (sixth and ninth day). The most suitable temperature was 30 °C, and the least favourable temperature was 20 °C, as for the products with 7 and 5% of initial total sugars content. Only the product obtained at 30 °C after six days had a higher color mark than the sample from the beginning of fermentation.

Odor

Kombucha products obtained from a fermentation medium with 7% of initial total sugars had the highest odor mark (4) on the third day at 30 and 20 °C. The lowest odor mark (1) showed products obtained at 30, 25, and 20 °C on the ninth day. The most suitable temperature was 30 and 20 °C, and the least favorable temperature was 25 °C. Samples produced at 30 °C (third and sixth day), 25 °C (third day), and 20 °C (third day) had higher odor marks than the fermentation start product.

Kombucha products obtained from a fermentation

medium with 5% of initial total sugars had the highest odor mark (5) on the third day at 30 and 20 °C, as the products with 7% sugars. The lowest odor mark (1) showed products obtained at 30, 25, and 20 °C on the ninth day, as the products with 7% of sugars. The most suitable temperatures were 30 and 20 °C, and the least favourable temperature was 25 °C, for the products with 7% of sugars. Samples produced at 30 °C (third and sixth day), 25 °C (third day), and 20 °C (third and sixth day) had higher odor marks than the product from the beginning of fermentation.

Kombucha products obtained from a fermentation medium with 3% of initial total sugars had the highest odor mark (4) on the third day at 30, 25, and 20 °C. The lowest odor mark (1) showed products obtained at 30, 25, and 20 °C on the ninth day, as the products with 7 and 5% of sugars. All of the fermentation temperatures showed the same suitability for the production. Samples produced at 30, 25, and 20 °C on the third and sixth days had higher odor marks than the fermentation start product.

Taste

Kombucha products obtained from a fermentation medium with 7% of initial total sugars had the highest taste mark (5) on the third day at 25 °C. The lowest taste mark (1) showed products obtained at 30, 25, and 20 °C on the ninth day, as well as the sample from the fermentation start. The most suitable temperature was 25 °C, and the least favorable temperatures were 30 and 20 °C. Samples produced at 30 °C (third and sixth day), 25 °C (third and sixth day), and 20 °C (third and sixth day) had higher taste marks than the fermentation start product.

Kombucha products obtained from a fermentation medium with 5% of initial total sugars had the highest taste mark (5) on the third day at 30, 25, and 20 °C. The lowest taste mark (1) showed products obtained at 30, 25, and 20 °C on the ninth day, as well as the sample from the beginning of the process. All of the fermentation temperatures showed the same suitability for the production. Samples produced at 30 °C (third and sixth day), 25 °C (third and sixth day), and 20 °C (third and sixth day) had higher taste marks than the product from the fermentation start, as the products with 7% of sugars.

Kombucha products obtained from a fermentation medium with 3% of initial total sugars had the highest taste mark (4) on the third day at 30 and 20 °C. The lowest taste mark (1) showed products obtained at 30, 25, and 20 °C on the ninth day, as well as the sample from the beginning of the process. All of the fermentation temperatures showed the same suitability for the production. Samples produced at 30, 25, and 20

°C on the third and sixth days had higher taste marks than the fermentation start product.

Cohen *et al.* [31] established that the sensory characteristics of kombucha products were more influenced by the process temperature than the sucrose content. Based on the formed metabolites, lower temperatures were more suitable since the obtained products were sweet. Higher temperatures lead to astringency and sourness that are not pleasant. Cohen *et al.* [31] also suggested that higher sugar content was related to a higher preference for kombucha products.

Modeling of total sensory mark

The total sensory mark was chosen for modeling as the most significant parameter of the sensory mark.

Table 3. shows the coefficients of the regression equation for total sensory mark in terms of coded and real variable values, as well as the related p-values. The obtained results have indicated that the factor of initial total sugar can be removed from the linear model while keeping model adequacy. A statistically significant coefficient is associated with the time of fermentation.

Table 2. Coefficients of the regression equation for total sensory mark.

Effects	Coefficient		*p*-value
	Actual	Coded	
Intercept			
b_0	2.8500	2.600	<0.0001
Linear			
b_1	0.0500	0.250	0.1546
b_3	-0.2500	-0.7500	<0.0001

A summary of the analysis of variance of the linear model for total sensory mark is given in Table S4. The model developed for the total sensory mark proved significant with a *p*-value of 0.0016. The "lack of fit *F*-value" of 0.58 implies that the lack of fit is not significant relative to the pure error. Adequate precision of the linear model for sensory characteristics, 9.608, indicates an adequate signal so this model can be used to navigate the design space. The sensory mark increases with the increase of temperature while it decreases with the duration of the fermentation process. Initial total sugar content does not influence the total sensory mark.

In a previously published paper [17], it was reported that based on the sensory mark, the consume day samples were products obtained after three days of fermentation. In this investigation, a more detailed insight into the sensory mark was given. The total sensory mark was higher (3) and (4) for products obtained after three days of fermentation at 30, 25, and 20 °C. These results indicated that regardless of the

initial total sugars content and fermentation process temperature, kombucha products ready for consumption were produced after three days of the process. Traditional kombucha beverage is usually obtained after 7–14 days [1] and the production of kombucha beverages on winery effluent leads to a significant reduction in the process duration and therefore to the economic savings, as well.

Optimization

Optimization of the operational parameters during kombucha fermentation was performed using the desirability function approach. The optimization was aimed at maximization of the total flavonoids and the sensory mark. The method combines a number of responses into a single response called the desirability function. The selected responses are transformed into individual desirability values in the range from 0 to 1. The overall desirability of the process is computed as the geometric mean of the individual desirability functions [20]. From the optimization results by the desirability function approach, it can be concluded that the optimal results in terms of the selected goal were obtained at 30 °C with an initial total sugars of around 7% and a fermentation period of three days. The optimized values of independent variables would result in the predicted values of 44.98 μg RE/mL for total flavonoids and 3.6 for the sensory mark. After the validation experiment, results are in good agreement with the optimized values given by the model i.e. total flavonoids content and sensory mark are 45.2 μg RE/mL and 4, respectively.

CONCLUSION

Total flavonoids content and sensory mark of winery effluent-based kombucha was established. The highest flavonoids content was determined in the initial medium (99.4±2.1 μg RE/mL) and the kombucha fermentation process led to the decrease in its value. The highest content in the consumed day (three days) kombucha beverages amounted to 50.4±6.8 μg RE/mL and it was measured in the product obtained at 20 °C with 3% of the initial total reducing sugars. The highest total sensory mark had consumed day kombucha beverages produced at 20 and 30 °C with 7, 5, and 3% of initial sugars, as well as the product obtained at 25 °C with 5% of sugars.

Results of statistical analysis by response surface methodology led to the conclusion that RSM is applicable for modeling of total flavonoids content in kombucha beverages. Therefore, they can be applied for quality evaluation in the production of kombucha beverages on winery effluent. The optimum production

58

conditions for the kombucha beverages with the highest values of total flavonoids (44.98 μg RE/mL) and sensory mark (3.6) were: the fermentation time of 3 days, the initial total sugars content around 7%, and temperature of 30 °C. Future research can be oriented towards the determination of single flavonoids compounds, as well as other phenolic compounds..

REFERENCES

[1]   S. Vukmanović, PhD Thesis, Faculty of Technology Novi Sad, University of Novi Sad (2022). https://nardus.mpn.gov.rs/handle/123456789/21144?locale-attribute=sr.

[2]   N. Abaci, F.S. Senol Deniz, I.E. Orhan, Food Chem.: X 14 (2022) 100302. https://doi.org/10.1016/j.fochx.2022.100302.

[3]   L.D.L. de Oliveira, M.V. de Carvalho, L. Melo, Rev. Ceres 61 (2014) 764–779. https://doi.org/10.1590/0034-737X201461000002.

[4]   M.M. Giusti, T.C. Wallace, In Handbook of Natural Colorants, T. Bechtold, R. Mussak, Eds., John Wiley & Sons, Ltd, Chichester, UK (2009), p. 255–275. https://doi.org/10.1002/9780470744970.ch16.

[5]   G. Kilic, I.Y. Sengun, Food Biosci. 53 (2023) 102631. https://doi.org/10.1016/j.fbio.2023.102631.

[6]   L.T. Phung, H. Kitwetcharoen, N. Chamnipa, N. Boonchot, S. Thanonkeo, P. Tippayawat, P. Klanrit, M. Yamada, P. Thanonkeo, Sci. Rep. 13 (2023) 7859. https://doi.org/10.1038/s41598-023-34954-7.

[7]   X. Wang, D. Wang, H. Wang, S. Jiao, J. Wu, Y. Hou, J. Sun, J. Yuan, LWT 168 (2022) 113931. https://doi.org/10.1016/j.lwt.2022.113931.

[8]   D. Cvetković, S. Markov, M. Djurić, D. Savić, A. Velićanski, J. Food Eng. 85 (2008) 387–392. https://doi.org/10.1016/j.jfoodeng.2007.07.021.

[9]   D. Cvetković, O. Šovljanski, A. Ranitović, A. Tomić, S. Markov, D. Savić, B. Danilović, L. Pezo: An artificial neural network as a tool for kombucha fermentation improvement, Chem. Ind. Chem. Eng. Q. 28 (2022) 277–286. https://doi.org/10.2298/CICEQ211013002C.

[10] E. Lončar, M. Djurić, R. Malbaša, L.J. Kolarov, M. Klašnja, Food Bioprod. Process. 84 (2006) 186–192. https://doi.org/10.1205/fbp.04306.

[11] R. Malbaša, L. Jevrić, E. Lončar, J. Vitas, S. Podunavac-Kuzmanović, S. Milanović, S. Kovačević, J. Food Sci. Technol. 52 (2015) 5968–5974. https://doi.org/10.1007/s13197-014-1648-4.

[12] J. Vitas, R. Malbaša, A. Jokić, E.S. Lončar, S.D. Milanović, Mljekarstvo 68 (2018) 116–125.

https://doi.org/10.15567/mljekarstvo.2018.0205.

[13] R. Malbaša, E. Lončar, M. Djurić, M. Klašnja, L. J. Kolarov, S. Markov, Food Bioprod. Process 84 (2006) 193–199. https://doi.org/10.1205/fbp.05061.

[14] F. Valiyan, H. Koohsari, A. Fadavi, J Food Sci Technol. 58 (2021) 1877–1891. http://doi:10.1007/s13197-020-04699-6.

[15] S. Vukmanović, J. Vitas, S. Kravić, Z. Stojanović, A. Đurović, B. Cvetković, R. Malbaša, Chem. Ind. Chem. Eng. Q. 00 (2024) 1–1. https://doi.org/10.2298/CICEQ231002001V.

[16] J. Vitas, S. Vukmanović, R. Malbaša. Waste Biomass Valorization 14 (2023) 4187–4200. https://doi.org/10.1007/s12649-023-02130-7.

[17] S. Vukmanović, J. Vitas, A. Ranitović, D. Cvetković, A. Tomić, R. Malbaša, LWT 154 (2022) 112726. https://doi.org/10.1016/j.lwt.2021.112726.

[18] J. Vitas, S. Vukmanović, J. Čakarevic, L. Popović, R. Malbaša, Chem. Ind. Chem. Eng. Q. 26 (2020) 157–170. https://doi.org/10.2298/CICEQ190708034V.

[19] J.S. Vitas, A.D. Cvetanović, P.Z. Mašković, J.V. Švarc-Gajić, R.V. Malbaša, J. Funct. Foods 44 (2018) 95–102. https://doi.org/10.1016/j.jff.2018.02.019.

[20] A. Jokić, Z. Zavargo, Z. Šereš, M. Tekić, J. Membr. Sci. 350 (2010) 269–278. http://dx.doi.org/10.1016/j.memsci.2009.12.037.

[21] S.A. Villarreal-Soto, S. Beaufort, J. Bouajila, J.-P. Souchard, P. Taillandier, J. Food Sci. 83 (2018) 580–588. https://doi.org/10.1111/1750-3841.14068.

[22] R. Jayabalan, P. Subathradevi, S. Marimuthu, M. Sathishkumar, K. Swaminathan, Food Chem. 109 (2008) 227–234. https://doi.org/10.1016/j.foodchem.2007.12.037.

[23] T.B.E. Öztürk, B. Eroğlu, E. Delik, M. Çiçek, E. Çiçek, Food Technol. Biotechnol. 61 (2023) 127–137. https://doi.org/10.17113/ftb.61.01.23.7789.

[24] A. Braune, M. Blaut, Gut Microbes 7 (2016) 216–234. https://doi.org/10.1080/19490976.2016.1158395.

[25] Y. Hsieh, M.-C. Chiu, J.-Y. Chou, J. Food Qual. 2021 (2021) 1735959. https://doi.org/10.1155/2021/1735959.

[26] D. Hunaefi, D.N. Akumo, H. Riedel, I. Smetanska, Antioxidants 1 (2012) 4–32. https://doi.org/10.3390/antiox1010004.

[27] H. Rodríguez, J.A. Curiel, J.M. Landete, B. de las Rivas, F. López de Felipe, C. Gómez-Cordovés, J.M. Mancheño, R. Muñoz, Int. J. Food Microbiol. 132 (2009) 79–90. https://doi.org/10.1016/j.ijfoodmicro.2009.03.025.

[28] X. Pu, P. Ye, J. Sun, C. Zhao, X. Shi, B. Wang, W. Cheng, LWT 176 (2023) 114536. https://doi.org/10.1016/j.lwt.2023.114536.

[29] Z. Liang, P. Zhang, W. Ma, X.-A. Zeng, Z. Fang, Food Biosci. 54 (2023) 102884. https://doi.org/10.1016/j.fbio.2023.102884.

[30] S. Kumar, A.K. Pandey, Sci. World J. 2013 (2013) 162750. https://doi.org/10.1155/2013/162750.

[31] G. Cohen, D.A. Sela, A.A. Nolden, Foods 12 (2023) 3116. https://doi.org/10.3390/foods12163116.

JASMINA VITAS
ALEKSANDAR JOKIĆ
NATAŠA LUKIĆ
STEFAN VUKMANOVIĆ
RADOMIR MALBAŠA

Univerzitet u Novom Sadu, Tehnološki fakultet Novi Sad, Bulevar cara Lazara 1, 21000 Novi Sad, Republika Srbija

PRIMENA MODELOVANJA U KONTROLI BIOAKTIVNOG KVALITETA KOMBUHA NAPITAKA

U ovom radu je ispitivana primena modelovanja na sadržaj ukupnih flavonoida i senzornu ocenu kombuha napitaka dobijenih na otpadnom toku iz proizvodnje vina. Parametri procesa su bili sledeći: period fermentacije - 0, 3, 6 i 9 dana; temperatura fermentacije - 20, 25 i 30 °C i početni sadržaj ukupnih redukujućih šećera - 3, 5 i 7%. Ukupni flavonoidi su određeni spektrofotometrijski, a do senzorne ocene se došlo primenom opisne metode i metode petobalnog bod sistema. Tokom fermentacionog procesa kombuhe, koji je trajao 9 dana, sadržaj ukupnih flavonoida je opao. U proseku, ukupna senzorna ocena je pokazala da se konzumni kombuha proizvodi dobijaju nakon 3 dana fermentacije, bez obzira na temperaturu fermentacije ili sadržaj šećera. Da bi se proizveo kombuha napitak najboljeg bioaktivnog kvaliteta, metoda odzivne površine je predložila sledeće procesne parametre: period fermentacije - 3 dana; početni sadržaj ukupnih redukujućih šećera - 7% i temperatura fermentacije - 30 °C..

Ključne reči: otpadni tok iz proizvodnje vina; ukupni flavonoidi; kombuha; senzorne karakteristike; metoda odzivne površine.

59

CEMRE AVŞAR[1,2]
SUNA ERTUNÇ[2]

[1]Toros Agri-Industry, Research and Development Center, Mersin, Turkey

[2]Ankara University, Department of Chemical Engineering, Ankara, Turkey

REACTION PARAMETER OPTIMIZATION OF AMMONIUM SULFATE PRODUCTION FROM PHOSPHOGYPSUM

Article Highlights
- A facile approach to phosphogypsum-derived ammonium sulfate production is presented
- The application of the proposed reaction sequence on industrial potential is discussed
- An effective waste management strategy for phosphogypsum is proposed

Abstract

Phosphogypsum (PG), the by-product of wet process phosphoric acid production, has a high recycle and reuse potential within the scope of compliance with CE strategies. This study offers a straightforward, two-step solid/liquid heterogeneous reaction sequence, providing the conversion of PG to ammonium sulfate (AS). Experiments were conducted following the OFAT design matrix with 3 factors, namely solid/liquid (w/v) ratio, pH, and particle size. The highest PG to AS conversion was achieved at 54.55% by utilizing PG below 125 µm particle size in the reaction performed with 1/10 solid/liquid (w/v) ratio at pH 10. Nitrogen and sulfur content of AS samples were characterized by Dumas Method and gravimetric SO_4 (ISO 9280:1990) analysis, respectively. The elemental composition was determined by ICP-OES, the crystallographic structure was investigated by XRD analysis, and the surface morphology of the particles obtained in the reaction was examined by SEM analysis. The chemical composition of AS product obtained at these conditions was determined as 21.29 wt% nitrogen and 24.23 wt% sulfur, respectively; where theoretical nitrogen and sulfur content in AS is 21.21 wt% and 24.24 wt%, respectively. This study provides outputs that have industrial importance since it proposes a novel approach for effective waste valorization and a new insight into AS production in the current fertilizer shortage.

Keywords: ammonium sulfate; circular economy; wet conversion; phosphogypsum; resource recovery.

SCIENTIFIC PAPER

UDC 666.913:54

Recent estimations show that the global population has increased to 8.1 billion, and projections expect that the number will reach up to 8.5 billion by 2030, and 9.8 billion by 2050 [1]. A direct relation between the population and food demand has made it crucial to achieve higher yields per application in agriculture. Mineral fertilizers include the essential nitrogen (N), phosphorus (P), and potassium (K) nutrients together with trace elements specified in variable formulations, and they are extensively used to enhance yield. According to the demand for mineral fertilizer application, annual production capacity has also increased to balance the supply and demand [2,3]. Geopolitical and economic world events also affect the affordability and availability of fertilizers. The COVID-19 pandemic resulted in elevated costs of raw materials and final fertilizer products, interrupting the food production and supply balance and resulting in changes in dietary patterns. Following the Russian-Ukrainian conflict, the world this time faced a malnutrition challenge since these countries provide 24% of the global wheat demand [4,5]. In the 4 years after the emergence of the COVID-19 pandemic, it can

be said that agriculture has been mostly affected in terms of the supply-demand ratio, labor shortages in the farming systems, and relevant negative impacts on the rural economy due to price fluctuations and lack of markets [6]. Lockdowns in the major countries have disrupted the balance in the production chain as in the case of China, the world's largest urea manufacturer [7]. Apart from the food-fertilizer perspective, energy should also be discussed since fertilizer production is an energy-intensive process. COVID-19 has also had a negative impact on the energy market and oil prices, which indirectly affects the fertilizer production capacity [8]. Russia, on the other hand, is an important exporter of mineral fertilizers and apart from the pandemic, the Russia-Ukraine conflict has resulted in decreasing production trends in N, P, and K-based fertilizers [9].

Food shortage risks cause new economic and societal concerns, and it is clearly foreseen that the food supply-demand chain will face possible disturbance soon. Apart from food demand, population increase brings an increase in the industrialization capacity. These two key factors have a cumulative effect on the unsustainable resource consumption and greenhouse gas (GHGs) emission increase, resulting in irreversible environmental challenges. Global warming, global resource depletion, and industrial or municipal waste increase have resulted in crisis on environmental and societal scale [10]. These latest socio-economic and environmental issues have recalled the importance of sustainable resource utilization. In this manner, the industrial waste management approach might provide a viable route by introducing the waste generated into re-processes. Introducing the circularity of industrial wastes to serve for circular economy (CE) strategy would also maintain sustainable resource consumption.

Phosphoric acid is the main raw material in phosphate-based fertilizer production. Demand for mineral fertilizers also triggered the annual production capacity of phosphate-based fertilizers and as-related phosphoric acid production. Phosphogypsum (PG) management, the by-product of wet process phosphoric acid production, is a multi-fold problem solver related to the above-mentioned highlights. Being generated up to 300 million tons annually and having a relatively low recycling rate below 15%, the rest amount is stored in landfills or discharged into aquatic environments [11].

Increasing the circularity of PG for various applications would provide an efficient approach to the industrial waste storage problem, which might have adverse effects on the ecosystem in the long term together with providing multi-step sustainable resource utilization cycles [12].

Relation between PG utilization and agriculture

PG is chemically gypsum ($CaSO_4 \cdot 2H_2O$) with some impurities, having approximately 30% Ca in CaO form and 55% S in SO_4 form, making it a suitable resource for agricultural applications. Its porous structure and high water-holding capacity make the material a mitigating tool for soil degradation and soil improvement. Apart from these direct application methods, PG can also be introduced into the production cycle as raw material for organomineral fertilizer production [13]. Another utilization approach of PG is the ammono-carbonation route, in which ammonium sulfate (AS) is produced [14]. AS has nitrogen and sulfur as ammonium and sulfate forms, respectively, and provides dual nutrients to plants due to its chemical structure [15]. Application of AS can be conducted directly as a fertilizer or can be utilized as the nitrogen and/or sulfur source in the formulation of compound fertilizers. Conventional ammono-carbonation route of PG yields AS and calcium carbonate ($CaCO_3$), both products have commercial value for various industrial applications. This route also provides effective approaches to permanent CO_2 storage as stable $CaCO_3$, also known as the mineral carbonation route [16–18]. Utilization of PG as the raw material for AS production processes would provide an efficient waste management strategy. This approach would also provide a problem-solving policy for the management of PG piles on a local basis and a tool for low-cost raw materials for AS production. PG valorization in AS production processes would also provide a solution to increasing fertilizer demand. Besides, with an annual generation rate of up to 300 million tons today, PG will be provided as a continuous raw material supply for the continuity of the AS production process. The straightforward route provided by this study might offer an effective PG management strategy in developing PG-derived AS production technology. The outcomes of the study have industrial importance since it provides a novel approach for effective waste valorization. In addition, having a high potential to scale up, this study would carry a new insight into low-cost AS production in the current fertilizer shortage.

In the study on the production of ammonium sulfate from phosphogypsum due to the extreme fluctuation in ammonia prices with the COVID-19 pandemic, it was reported that the cost of producing ammonium sulfate from phosphogypsum would be more costly than the producer's production of ammonium sulfate without using phosphogypsum as a raw material [19]. The use of waste materials such as phosphogypsum as raw materials will be an important contribution to the sustainability of the circular

economy, as the amount of fixed inputs such as in-process raw materials and temperature to increase production efficiency will vary during the reaction, positively affecting the reaction efficiency. In this respect, producing ammonium sulfate from a waste material such as phosphogypsum, which is an industrially controversial waste material, will avoid its contribution to the reaction efficiency or a feasibility study that is not excessively high.

MATERIAL AND METHODS

Production of AS from PG through the ammono-carbonation route is an old-school technology. Known as the Merseburg Process in the literature, the reaction sequence is based on the reaction between anhydrous or hydrated gypsum ($CaSO_4 \cdot H_2O$) and ammonium carbonate (($NH_4)_2CO_3$), yielding AS (($NH_4)_2SO_4$) and calcium carbonate ($CaCO_3$) [20]. In case where PG is utilized, the reaction sequence is given in Eqs. (1−3) below:

$$NH_3 + H_2O \rightarrow NH_4OH \tag{1}$$

$$2NH_4OH + CO_2 \rightarrow 2(NH_4)_2CO_3 + H_2O \tag{2}$$

$$CaSO_4 \cdot 2H_2O + (NH_4)_2CO_3 \rightarrow (NH_4)_2SO_4 + CaCO_3 + 2H_2O \tag{3}$$
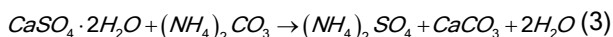
Merseburg Process is only available when there is a continuous CO_2 source. In this manner, this old-school technology can be a research hotspot, because it provides both CO_2 and PG consumption [21]. However, the investment and operating costs of the process hinder the real-time operation on an industrial scale and only 3% of the global AS production is through the "gypsum" route [22].

AS production through the reaction of PG and phosphoric acid in alkali media as a two-step sequence Eqs. (4) and (5) can also be viable [23].

$$5CaSO_4 \cdot 2H_2O + 3H_3PO_4 \rightarrow Ca_5(PO_4)_3OH + 5H_2SO_4 + 9H_2O \tag{4}$$

$$10NH_4OH + 5H_2SO_4 \rightarrow 5(NH_4)_2SO_4 + 10H_2O \tag{5}$$
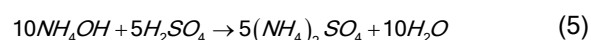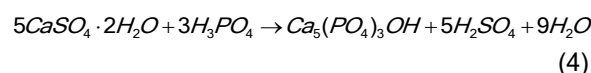
PG samples used in the study were provided by a fertilizer manufacturer in Turkey. 85% H_3PO_4 (Sigma Aldrich) and 21% NH_4OH (diluted by 25% NH_4OH, Sigma Aldrich) were used as the reagents in the reaction. The above-mentioned alkali route Eqs. (4) and (5) is conducted through the preparation of PG: water suspension followed by H_3PO_4 addition for decomposition of PG and calcium phosphate (hydroxyapatite, HAp) formation (Fig. 1). Further steps include pH adjustment via aqueous NH_4OH solution to yield ($NH_4)_2SO_4$ as filtrate.
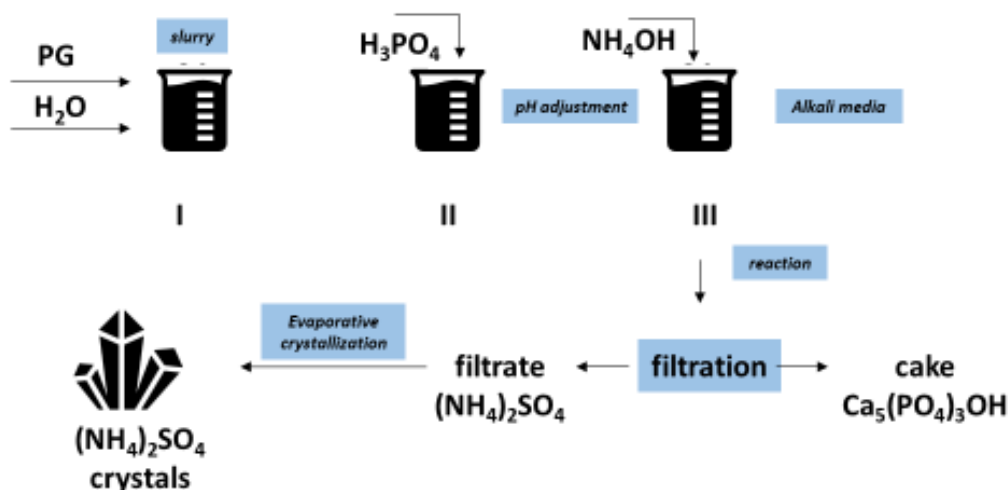
Figure 1. Simplified schematic illustration of the reaction system.

Alkali conditions also provide the precipitation of HAp particles, obtained as the cake when the reaction is terminated. Final AS crystals are obtained via further evaporative crystallization of the filtrate at 120 °C. Obtained AS crystals were oven-dried at 80 °C until constant weight was achieved. HAp particles were also oven-dried at 80 °C.

SEM analysis

SEM analysis (FEI Quanta 650) was conducted to investigate the morphological characteristics of obtained AS samples. The analysis parameters were

63

determined as maximum magnification 5000, WD; 9.7 mm, resolution 50 nanometers.

The setting of the model and reaction parameters

Optimization of the reaction conditions should be designed in such an experimental strategy to investigate the degree of interactions between variables and experimental error, which have relatively high importance in the design matrix. One factor at a time (OFAT) strategy is designed to investigate the factor relation, in which the matrix was set to seek information about one individual factor per experimental trial while keeping the other factor level constant and observing the sensitivity of the reaction system to the factors [24–26]. The research hypothesis in the study Eqs. (4) and (5) provides a two-step, heterogenous solid-liquid reaction system. The stirring rate was kept constant at 750 rpm in all runs to prevent precipitation of the solid PG particles by providing a continuum in the solid-liquid interface and increasing the reaction surface area. Agitation speed also provided the elimination of mass transfer limitations by reducing diffusion resistance in the heterogenous reaction media.

Experiment runs were conducted at ambient pressure. Although temperature is an important parameter in the reaction yield, thermodynamic analysis of the reaction sequence was calculated regarding the overall reaction given below:

$$5CaSO_4 \cdot 2H_2O + 3H_3PO_4 + 10NH_4OH \rightarrow \qquad (6)$$
$$Ca_5(PO_4)_3OH + 5(NH_4)_2SO_4 + 19H_2O$$
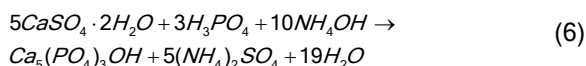
The equilibrium constant (K) of the overall reaction was calculated according to the Van't Hoff equation Eq. (7) by calculating the standard molar Gibbs energy of formation of the reactants at 25 °C (Table 1):

$$\Delta G_f \rightarrow -RT\ln(K) \qquad (7)$$

where R is the gas constant, T is temperature and K is the equilibrium constant.

Table 1. Standard Gibbs energy of formation of reactants and products at 25 °C.

	G_f (kJ/mol)			
reactants		Ref.	products	Ref.
$CaSO_4\cdot2H_2O$	-1795.7	[26]	$Ca_5(PO_4)_3OH$	-5929.7	[28]
H_3PO_4	-1119.1	[26]	$(NH_4)_2SO_4$	-901.7	[26]
NH_4OH	-253.85	[26]	H_2O	-237.14	[26]

According to the data given in Table 1, the reaction equilibrium constant (K) was calculated to be >>1, indicating that the reaction was spontaneous-

irreversible at 25 °C. Thus, temperature was kept constant at 25 °C in experiment runs. OFAT method was applied to investigate the sensitivity of the reaction sequence based on a quantitative variance system and observed the effects upon the measurement of the output responses. Particle size, solid/liquid ratio in PG/water suspension, and pH (alkalinity strength) were chosen to be the factors, whereas AS yield was the response calculated from the conversion of PG to AS Eq. (8) obtained through evaporative crystallization of the filtrate at 120 °C. Obtained AS crystals were oven-dried at 80 °C until constant weight was achieved.

$$Conversion\ yield\,(\%) = \frac{m\left(SO_4^{2-}\right)_{filtrate}}{m\left(SO_4^{2-}\right)_{PG,initial}} \cdot 100 \qquad (8)$$

where $m(SO_4^{2-})_{filtrate}$ and $m(SO_4^{2-})_{PG,initial}$ denote the quantitative amount of SO_4^{2-} in the filtrate and PG sample, respectively.

Determination of factor ranges

Reaction runs were conducted with PG samples having two different particle sizes, sieved in a range of <10^4 μm and <125 μm to observe the rate-limiting effect of particle size.

According to Eq (4) and (5), the first step prior reaction was the preparation of PG/water suspensions to provide the aqueous reaction media. The solid/liquid (w/v) ratio was investigated at 3 levels, having a constant proportion between the edges and the medium in the determined factor range. This parameter is also directly proportional to the concentration of the filtrate obtained at the end of the reaction and as-related energy consumption during the evaporative crystallization step. Lower aqueous solubility of PG might be a rate-limiting step in the proposed two-step solid-liquid heterogeneous reaction system to provide an adequate solid surface. Although salt solutions are effective in enhancing the solubility of PG, there might be a significant chlorine contamination risk according to the chlorine content of the salt solution [29,30]. Additionally, chloride ions in the reaction media might favor the reaction to ammonium chloride formation and lower the yield of the desired product. Thus, water has been chosen to prepare the suspension before the reaction. Factor ranges were determined in such a ratio to prevent the slurry formation at a constant stirring rate according to the literature search and PG/water suspensions were prepared to have 1/5, 1/7.5, and 1/10 (w/v) ratios [31].

The acidity of the reaction media increases with H_3PO_4 addition. This step provides the degradation of $CaSO_4\cdot2H_2O$ structure and formation of calcium-phosphate structure (HAP). Further NH_4OH addition

provides the precipitation of HAP particles in alkali media, which generally occur at a slightly alkaline (pH 9–11) range [32, 33]. Thus, the pH range of the reaction runs was determined to be 9–11. NH_4OH addition favors $(NH_4)_2SO_4$ formation, being the nitrogen source of the desired product.

Table 2. OFAT design matrix for three factors.

Particle size	Solid/liquid ratio (w/v)	pH	Run #
<10⁴ µm	1/5	9	1
		10	2
		11	3
	1/7.5	9	4
		10	5
		11	6
	1/10	9	7
		10	8
		11	9
<125 µm	1/5	9	10
		10	11
		11	12
	1/7.5	9	13
		10	14
		11	15
	1/10	9	16
		10	17
		11	18

Reaction runs were conducted in closed vessels according to the OFAT design (Table 2), investigating the factor-response relation per run of overall 18. Cake and filtrate were separated by filtration after the reaction was terminated, followed by the evaporative crystallization step of the filtrate to obtain AS crystals.

RESULTS AND DISCUSSION

18 runs with two replications were conducted to minimize experimental errors. The stirring rate was arranged as 750 rpm in all of the runs to create a constant solid/liquid interface between the reactants. Responses to the factors, mass conversion (%) of PG to AS, were calculated from the net AS amount obtained via the evaporative crystallization step. Table 3 gives the calculated averages of mass conversion of the replicated experiments.

According to the data given in Table 3, optimum reaction conditions in the OFAT matrix were obtained in run # 17. Figures 2 and 3 give the factor-response relation in the OFAT design matrix according to the particle size of PG used, <10⁴ µm and <125 µm, respectively.

Figure 2 gives the conversion (%) of PG in specified PG/water (w/v) and pH range. 1/5 and 1/7.5 PG/water (w/v) ratio show relatively lower conversion when compared to 1/10 PG/water (w/v) ratio.

Similar to the results obtained in <10⁴ µm particle-sized PG, <125 µm particle-sized PG shows the same

Table 3. Response analysis of experiment runs.

Particle size	Solid/liquid ratio (w/v)	pH	PG conversion (%)
<10⁴ µm	1/5	9	32.99
		10	32.97
		11	21.29
	1/7.5	9	35.16
		10	38.99
		11	25.90
	1/10	9	46.67
		10	49.41
		11	49.05
<125 µm	1/5	9	31.25
		10	28.04
		11	28.01
	1/7.5	9	26.34
		10	40.41
		11	36.39
	1/10	9	52.3
		10	54.55
		11	50.14
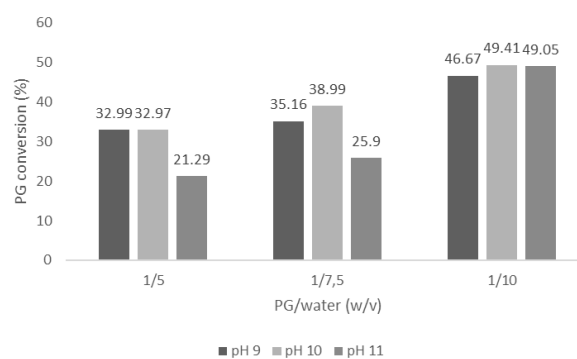
Figure 2. PG conversion (%) according to solid/liquid ratio and pH (PG particle size <10⁴ µm).
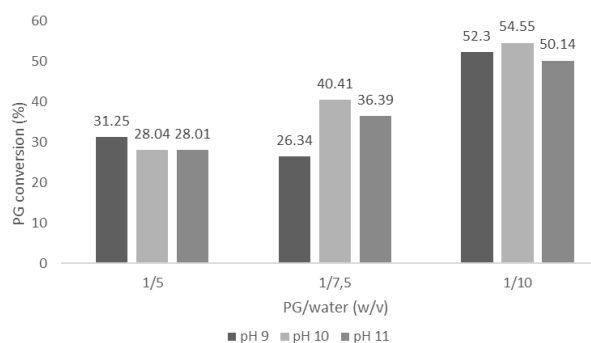
Figure 3. PG conversion (%) according to solid/liquid ratio and pH (PG particle size <125 µm).

conversion trend. A higher conversion ratio at 1/10 PG/water (w/v) ratio might be attributed to the lower aqueous solubility of PG at dense PG-water suspensions [34]. Solubility of PG at aqueous media is a driving force for the availability of SO_4^{2-} in the reaction media, which will further act as the sulfur source in the formation of AS.

NH_4OH addition has critical importance in ther

reaction sequence since it is the nitrogen source of the desired AS product. pH and NH_4OH addition are related to each other, and the lowest conversions were obtained for pH 9 condition sets. Reactions conducted at pH 10 and 11 showed similar conversion (%) at a 1/10 PG/water (w/v) ratio, however, the highest conversion yields were obtained at pH 10 condition. Higher conversion with lower raw material input might favor the economic feasibility of the reaction sequence in case of scaling up. A decrease in the particle size has increased the conversion yield of PG. Variations in the particle size might have acted as a rate-limiting step during the reaction [35]. $<10^4$ µm particle-sized PG might have a variable particle size distribution when compared to <125 µm particle size range and lower particle size has increased the surface area during the reaction.

According to the factor-response analysis, the optimum reaction conditions for the proposed reaction sequence were determined as in the case of run #17, where the PG/water ratio was 1/10 (w/v), pH 10 with PG having <125 µm particle size. Experimental studies revealed that a higher conversion yield was obtained as the particle size of the PG sample decreased. This phenomenon can be attributed to the increase in the reaction rate due to the increased surface area as the particle size of the reactant decreases. 54.55% mass conversion was obtained at the determined optimum conditions. However, stoichiometric conversion (Eq. 6) was calculated as 76.74%. When compared to stoichiometric data, the 54.55% conversion efficiency of PG can be considered relatively low. Reaction modifications such as excess NH_4OH utilization, incorporating AS in the reaction media as the seed product, or observing the catalytic effect of H_2SO_4 on the probable ongoing side reaction between NH_4OH can be employed to increase the conversion efficiency. H_2SO_4 can also be utilized as a crystallization aid after phase separation by directly introducing it to the filtrate in the evaporative crystallization step [36].

Chemical composition verification of obtained AS in the optimum conditions was conducted via Dumas and ISO 9280:1990 methods to measure nitrogen and sulfate content, respectively. Ammonium sulfate theoretically has 27.27 wt% of NH_4, which is attributed to 21.21 wt% of nitrogen. According to Dumas method, synthesized AS product had 21.29 wt% nitrogen. Sulfate content in theoretical AS is 72.72 wt%, whereas sulfur content is calculated as 24.24 wt%. According to ISO 9280:1990 analysis, the AS sample had 72.69 wt% sulfate, which is calculated as 24.23 wt% sulfur. Chemical composition analysis results revealed that the nitrogen and sulfur content of obtained AS samples comply with theoretical grades in AS.

The elemental composition of AS samples obtained at the optimum conditions was investigated by the ICP-OES analysis (Table 4) in comparison with the analytical grade AS (Sigma Aldrich).

Table 4. ICP-OES analysis results of AS.

Sample	Elemental Composition (ppm)			
	Al	Cd	Cu	Mn
Reference AS Sigma Aldrich	1,533	(-)	(-)	0,0197
AS obtained at <125 µm PG, s/l 1/10 (w/v), pH 10	1,429	0,143	1,404	(-)

Cr, Ni, and Pb were not detected in both reference and obtained AS samples. The Al content in the obtained AS sample was lower than the reference, at 1.429 and 1.533 ppm, respectively. Cd and Cu were not observed in the reference material; however, 0.143 and 1.404 ppm Cd and Cu were analyzed in the obtained AS sample, respectively. Contrary to Cd and Cu, the Mn content was analyzed in the reference AS sample as 0.0197 ppm and was not analyzed in the synthesized AS sample. According to ICP-OES results, the synthesized AS sample has a low impurity content, indicating that PG-based impurity transition occurs to the solid phase, and the AS sample obtained through evaporative crystallization of the filtrate has relatively low impurity content. ICP-OES results of PG used in the reaction and HAp particle obtained in the optimum reaction conditions are given in Table 5.

Table 5. ICP-OES analysis results of PG and HAp.

Sample	Elemental Composition (ppm)					
	Cd	Cr	Cu	Mn	Ni	Pb
PG [36]	1,56	6,27	9,55	15,7	17,16	3,68
HAp [37]	1,468	6,059	NA	3,429	0,3	3,552
*Not Applicable						

Table 5 indicates that the major amount of the impurities that originated in PG remained in the solid phase after the conversion reaction. Considering 54.55% PG conversion to AS, the solid phase can be evaluated as a Ca-rich precipitate with impurities on ppm level.
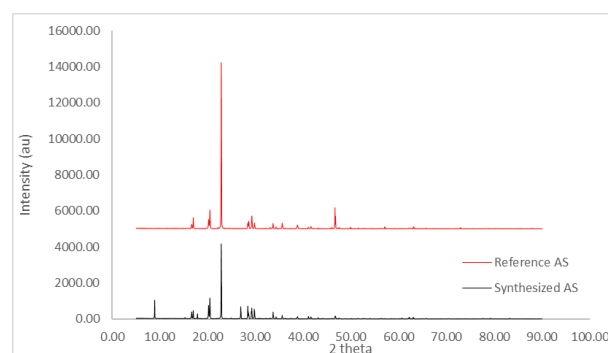

Figure 4. XRD patterns of reference and synthesized AS samples.

.

Figure 4 was provided as including the XRD pattern of JCPDS standard as a small figure in the upper section, indicating that the crystallographic structure of both samples shows high consistency. Relatively lower intensities of the characteristic peaks of synthesized AS samples are attributed to the impurities in the sample.

The preliminary analysis shows that the obtained crystal product meets the chemical content requirements of AS, but further characterization analysis should be employed. However, the problem is that HAp obtained as a by-product in the production of ammonium sulfate from phosphogypsum cannot be utilized in the agricultural industry [38,39], except for the impurities such as cadmium it contains. It is directly related to the problem of dissolution rate in water and soil.

HAp obtained in the synthesis route can be evaluated through various routes. Owing to the calcium and phosphorus in its chemical composition, HAp particles can be used in agriculture as an alternative phosphorus fertilizer with calcium nutrients. Besides, micronutrient impregnation might also help to widen the fertilizer formulation for specific applications such as nutrient demand for a particular plant growth or deficient nutrient content in the soil where fertilizer is applied. HAp can also be functionalized as a slow-release fertilizer, providing nutrient release in a prolonged time rather than burst release after application [40,41]. HAp particles can also be evaluated as a substitute for bone ash in the ceramics industry; however, there is a lack of literature in this field [42].

According to SEM analysis (Figures 5 and 6), important results were obtained about the transition to crystal structure and the surface properties of different by-products formed depending on the conversion rate.
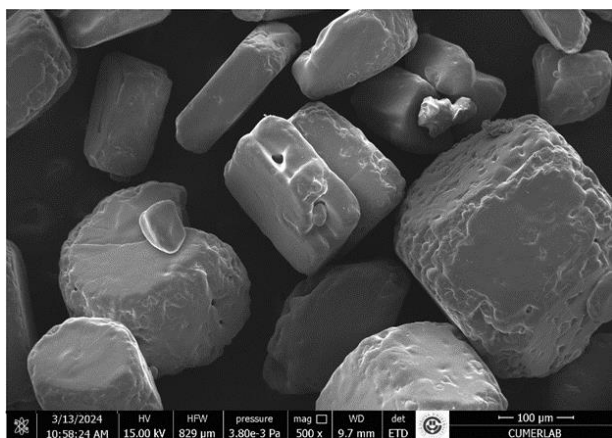
Figure 5. Surface morphology of ammonium sulfate obtained as a result of the experimental process.

During the ammonium sulfate formation reaction,

a significant difference in the crystal structure stands out depending on the conversion rate, but with the formation of HAp, it has been observed that rod-like molecules develop in a way that creates deformation in the crystal structure.
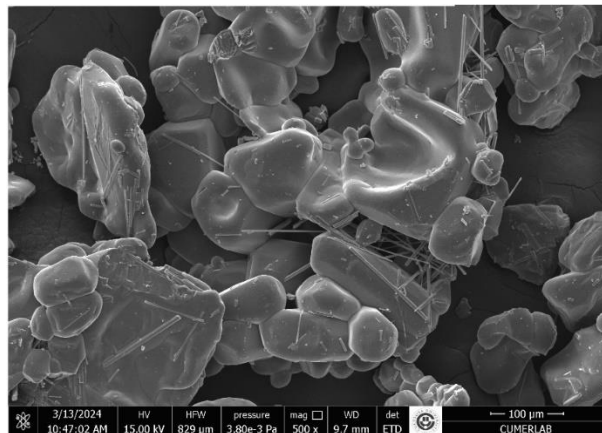
Figure 6. By-products such as HAp formed during the experimental process depending on the conversion rate of ammonium sulfate and their effects on the crystal structure.

According to Figure 6, effective phase separation might reduce reaction residues in the AS sample.

CONCLUSION

The two-step, heterogeneous solid/liquid reaction sequence provided by this study offers the conversion of PG to AS and calcium phosphate, namely hydroxyapatite. OFAT design matrix with three factors, solid/liquid ratio, pH, and particle size, was utilized to investigate the PG conversion (%) as the response. 18 experiment runs with two replicates were performed and the highest PG conversion was achieved at 54.55% in a reaction conducted with a solid/liquid ratio (w/v) of 1/10, pH 10, and PG with the particle size of <125 μm. Obtained solid sample in these reaction conditions had 21.29 wt% nitrogen and 24.23 wt% sulfur, meeting the nitrogen and sulfur content requirement of AS. A dilute suspension system favors PG solubility and provides an adequate solid/liquid interface, and a decrease in particle size also enhances the solid interface. These parameters might adversely affect the economic feasibility of the proposed sequence in terms of scaling up due to the high amount of process water consumption. Detailed research on the development of the study might enhance the industrial applicability of the proposed synthesis route. In case of scaling up, this study might provide local investments where PG piles are stored, where an effective recycle route for PG and low-cost production of AS are conducted.

AVŞAR & ERTUNÇ: REACTION PARAMETER OPTIMIZATION OF…

Chem. Ind. Chem. Eng. Q. 31 (1) 61–69 (2025)

ACKNOWLEDGMENT

NOMENCLATURE

PG	Phosphogypsum
AS	Ammonium sulfate
HAp	Hydroxyapatite
OFAT	One factor at a time
CE	Circular Economy
GHG	Greenhouse Gas
XRD	X-Ray Diffraction Spectroscopy
ICP-OES	Inductively Coupled Plasma-Optical Emission Spectroscopy

REFERENCES

[1] N. Amiri, M. Yacoubi, M. Messouli, IGI Global (2023) 69–192. https://doi.org/10.4018/978-1-6684-4649-2.ch007.

[2] A. Paucean, V. Muresan, Processes 11(1) (2023) 150. https://doi.org/10.3390/pr11010150.

[3] J.C. Cheong, J.T.E. Lee, J.W. Lim, S. Song, J.K.N. Tan, Z.Y. Chiam, K.Y. Yap, E.Y. Lim, J. Zhang, H.T.W. Tan, Y.W. Tong, Sci. Total Environ. 715 (2020) 136789. https://doi.org/10.1016/j.scitotenv.2020.136789.

[4] T. Eftimov, G. Popovski, M. Petkovic, B.K. Seljak, D. Kocev, Trends Food Sci. Technol. 104 (2020) 268–272. https://doi.org/10.1016/j.tifs.2020.08.017.

[5] M. Ali, A. Aljounaidi, A. Ateik, SSRN eLibrary. http://doi.org/10.2139/ssrn.4320568.

[6] A.M. Asegie, S.T. Adisalem, A.A. Eshetu, African J. Sci. Technol. Innov. Dev. 16 (2) (2024), 253–264. https://doi.org/10.1080/20421338.2023.2295626.

[7] URL:https://www.reuters.com/markets/commodities/china-slows-fertiliser-exports-raising-industry-concerns-india-2023-09-08/ (19.02.2024).

[8] S. Saraf, A. Bera, Int. J. Oil, Gas Coal Technol. 35(2) (2024) 205–240. https://doi.org/10.1504/IJOGCT.2024.136546.

[9] H. van Meijl, H. Bartelings, S. van Berkum, H.D. Cui, Z.S. Kristkova, W.J. van Zeist, Commun. Earth Environ. 5 (2024) 59. https://doi.org/10.1038/s43247-024-01208-x.

[10] M.S. Uddin, K. Mahmud, B. Mitra, A.E. Hridoy, S.M. Rahman, M. Shafiullah, M.S. Alam, M.I. Hossain, M. Sujauddin, Sustainability 15(3) (2023) 1748. https://doi.org/10.3390/su15031748.

[11] G. Liu, M. He, H. Chen, A.M. Rashad, Y. Liang, Constr. Build. Mater. 415 (2024) 135030. https://doi.org/10.1016/j.conbuildmat.2024.135030.

[12] B. Bouargene, K. Laaboubi, M.G. Biyoune, B. Bakiz, A. Atbir, J. Mater. Cycles Waste Manage. 25 (2023) 1288–1308. https://doi.org/10.1007/s10163-023-01617-8.

[13] M.A. Matveeva, Y.D. Smirnov, D.V. Suchkov, Environ.

Geochem. Health 44 (2021) 1605–1618. https://doi.org/10.1007/s10653-021-00988-x.

[14] A. Idboufrade, B. Bouargene, B. Ennasraoui, M.G. Biyoune, A. Bachar, B. Bakiz, A. Atbir, S. Mançour-Billah, Waste Biomass Valor. 13 (2022) 1795–1806. https://doi.org/10.1007/s12649-021-01600-0.

[15] B. Bouargene, A. Marrouche, S.E. Issiouy, M.G. Biyoune, A. Mabrouk, A. Atbir, A. Bachar, R. Bellajrou, L. Boukbir, B. Bakiz, J. Mater. Cycles Waste Manage. 21(6) (2019) 1563–1571. http://dx.doi.org/10.1007%2Fs10163-019-00910-9.

[16] M. Zhang, X. Fan, Sci. Rep. 13 (2023) 4156. https://doi.org/10.1038/s41598-023-28251-6.

[17] Y. Ennaciri, A. Cherrat, H. El Alaoui-Belghiti, M. Bettach, Mor. J. Chem. 11(2) (2023) 444–459. https://doi.org/10.48317/IMIST.PRSM/morjchem-v11i2.35817.

[18] A.O. Gezerman, Int. J. Chem. Technol. 6(2) (2022) 102–107. https://doi.org/10.32571/ijct.1187158.

[19] A. IM.Chou, (1995) Technical report, March 1-May 31, 1995. No. DOE/PC/92521-T241.

[20] C. Avşar, D. Tümük, S. Ertunç, A.O. Gezerman, Chem. Rev. Lett. 5(1) (2022) 83–91. https://doi.org/10.22034/crl.2022.329067.1154.

[21] C. Avşar, D. Tümük, A.E. Yüzbaşıoğlu A.E., A.O. Gezerman, Kem. Ind. 71(9-10) (2022) 633–638. https://doi.org/10.15255/KUI.2021.088.

[22] C.R. Canovas, R. Perez-Lopez, F. Macias, S. Chapron, J.M. Nieto, S. Pellet-Rostaing, J. Clean. Prod. 143 (2017) 497–505. https://doi.org/10.1016/j.jclepro.2016.12.083.

[23] S. Mousa, A. Hanna, Mater. Res. Bull. 48(2) (2013) 823–828. https://doi.org/10.1016/j.materresbull.2012.11.067.

[24] D.D. Frey, F. Engelhardt, E.M. Greitzer, Res. Eng. Des.14 (2003) 65–74. https://doi.org/10.1007/s00163-002-0026-9.

[25] F. Campolongo, J. Cariboni, A. Saltelli, Environ. Model. Software 22(10) (2007) 1509–1518. https://doi.org/10.1016/j.envsoft.2006.10.004.

[26] J. Wang, W. Wan, Int. J. Hydrogen Energy 34(1) (2009) 235–244. https://doi.org/10.1016/j.ijhydene.2008.10.008.

[27] S. Billon, P. Vieillard, Am. Mineral. 100(2-3) (2015) 615–627. https://doi.org/10.2138/am-2015-4925.

[28] B. Puzio, M. Manecki, M. Kwasniak-Kominek, Minerals 8(7) (2018) 281. https://doi.org/10.3390/min8070281.

[29] I. Hammas, K. Horchani-Naifer, M. Ferid, Int. J. Miner. Process.123 (2013) 87–93. https://doi.org/10.1016/j.minpro.2013.05.008.

[30] C. Avşar, S. Ertunç, Environ. Qual. Manage. 32(3) (2022) 367–374. https://doi.org/10.1002/tqem.21929.

[31] A.T. Kandil, M.F. Cheira, H.S. Gado, M.H. Soliman, H.M. Akl, J. Radiat. Res. Appl. Sci. 10(1) (2017) 24–33. https://doi.org/10.1016/j.jrras.2016.11.001.

[32] J.F. Ferguson, D. Jenkins, J. Eastman, J. Water Pollut. Control Fed. 45(4) (1973) 620–631.

[33] Y. Lei, B. Song, van der Weijden, M. Saakes, C.J.N. Buisman, Environ. Sci. Technol. 51(19) (2017) 11156–11164. https://doi.org/10.1021/acs.est.7b03909.

[34] A. Bounaga, A. Alsanea, K. Lyamlouli, C. Zhou, Y. Zeroual, R. Boulif Rittmann, Biotechnol. Adv. 57 (2022) 107949.

https://doi.org/10.1016/j.biotechadv.2022.107949.

[35] T. Mashifana, F. Ntuli, F. Okonta, S. Afr. J. Chem. Eng. 27 (2019) 1–6. https://doi.org/10.1016/j.sajce.2018.11.001.

[36] J. Park, W. Lee, J.K. Choe, Y. Choi, Sep. Purif. Technol. 318 (2023) 123869. https://doi.org/10.1016/j.seppur.2023.123869.

[37] C. Avşar (2023). PhD Thesis, Ankara University Institute of Natural and Applied Sciences.

[38] Unpublished report. Toros AGRI Industry and Trade Co. Inc. R&D Center, Mersin/ Turkey.

[39] C. Avşar (2022). Kem. Ind. 71 (2022).

https://doi.org/10.15255/KUI.2021.057.

[40] Y. Wibisono, V. Rafianto, D. Alvianto, G. Djoyowasito, B. D. A. Nugroho, C. Arif, Int. J. Recycl. Org. Waste Agric. 12 (4) (2023) 601–614. https://doi.org/10.30486/ijrowa.2023.1964772.1518.

[41] M. Ammar, S. Ashraf, J. Baltrusaitis, Ceramics 6(3) (2023) 1799–1825. https://doi.org/10.3390/ceramics6030110.

[42] A. Kara, R. Stevens, J. Eur. Ceram. 22(5) (2002) 731–736. https://doi.org/10.1016/S0955-2219(01)00371-5.

CEMRE AVŞAR[1,2]
SUNA ERTUNÇ[2]

[1]Toros Agri-Industry, Research and Development Center, Mersin, Turkey

[2]Ankara University, Department of Chemical Engineering, Ankara, Turkey

OPTIMIZACIJA REAKCIONIH PARAMETARA PROIZVODNJE AMONIJUM-SULFATA IZ FOSFOGIPSA

Fosfogips (PG), nusproizvod proizvodnje fosforne kiseline u vlažnom procesu, ima visok potencijal recikliranja i ponovne upotrebe u okviru usaglašenosti sa strategijama cirkularne ekonomije. Ova studija nudi jednostavnu, dvostepenu heterogenu čvrsto/tečno reakciju kojom se PG konvertuje u amonijum-sulfat (AS). Eksperimenti su sprovedeni prema dizajnu OFAT matrice sa 3 faktora - odnos čvrsto/tečno, pH i veličina čestica. Najveća konverzija PG u AS od 54,55% postignuta je korišćenjem PG čestica manjih od 125 µm u reakciji izvedenoj sa odnos čvrsto/tečno 1/10 pri pH 10. Sadržaj azota i sumpora u AS uzorcima je određen Dumasovom metoda i gravimetrijski kao sulfat (ISO 9280:1990)a, redom. Elementarni sastav je određen ICP-OES, kristalografska struktura je ispitana KSRD analizom, a površinska morfologija čestica dobijenih u reakciji SEM analizom. Hemijski sastav AS proizvoda dobijenog u ovim uslovima je 21,29 tež% azota i 24,23 tež% sumpora, redom; teorijski sadržaj azota i sumpora u AS je 21,21 tež% i 24,24 tež%. Ova studija pruža rezultate koji imaju industrijski značaj jer predlaže novi pristup za efektivnu valorizaciju otpada i novi uvid u proizvodnju AS u trenutnoj nestašici đubriva.

Ključne reči: amonijum sulfat; cirkularna ekonomija; mokra konverzija; fosfogips; iskorišćenje resursa.

NAUČNI RAD

BERENICE CLIFTON-GARCÍA[1]
JUAN VILLAFAÑA-ROJAS[2]
ORFIL GONZÁLEZ-REYNOSO[3]
JORGE RAMON ROBLEDO-ORTIZ[1]
RICARDO MANRÍQUEZ-GONZÁLEZ[1]
PORFIRIO GUTIÉRREZ-GONZÁLEZ[4]
YOLANDA GONZÁLEZ-GARCÍA[1]

[1]Departamento de Madera, Celulosa y Papel, Centro Universitario de Ciencias Exactas e Ingenierías, Universidad de Guadalajara. Guadalajara, México

[2]Departamento de Biotecnológicas y Ambientales, Universidad Autónoma de Guadalajara, México

[3]Departamento de Ingeniería Química, Centro Universitario de Ciencias Exactas e Ingenierías, Universidad de Guadalajara. Guadalajara, México

[4]Departamento de Matemáticas, Centro Universitario de Ciencias Exactas e Ingenierías, Universidad de Guadalajara. Guadalajara, México

SCIENTIFIC PAPER

UDC 628.35:66:633.15

USE OF AN INTERNAL LOOP AIRLIFT BIOREACTOR TO PRODUCE POLYHYDROXYALKANOATES BY *Stenotrophomonas rhizophila*

Article Highlights
- First report on *Stenotrophomonas rhizophila* culture using cheap molasses to produce PHB
- High biomass and PHA yields were reached using an easy-to-construct airlift bioreactor
- A feeding strategy based on replenishing the liquid loss resulted in high polymer accumulation

Abstract

Airlift-type bioreactors present advantages over conventional systems such as efficient mass transfer, simplicity of construction, and low energy consumption. Thus, they are a good alternative for the production of polyhydroxyalkanoates (PHAs) nevertheless, their use for that purpose has been barely studied. This work addresses the design, construction, and hydrodynamic characterization of a 2.4 L internal loop airlift bioreactor, evaluating the effect of the airflow, liquid volume, and disperser position, on the interfacial area and the mixing time. Then, it was used for the fed-batch production of PHB by Stenotrophomonas rhizophila from sugar cane molasses. It was found that the conditions to increase the interfacial area and minimize the mixing time were: airflow of 1.5 vvm, liquid volume of 2400 mL, and disperser position of 5 mm (distance between the air disperser and the drag tube). Under that configuration, the maximum biomass concentration, PHB production, and PHB accumulation achieved (54 h of culture) were 65.4 g/L, 39.9 g/L, and 60.2 % (g of PHB/100 g dry biomass), respectively. The polymer was poly-3-hydroxybutyrate, with a melting temperature of 170°C, crystallinity of 56.4 %, and a Mw of 735 kDa.

Keywords: airlift bioreactor; molasses; polyhydroxyalkanoates; Stenotrophomonas rhizophila.

Polyhydroxyalkanoates (PHAs) are microbial bioplastics accumulated as intracellular granules by different microbial species under conditions of nutritional stress caused by an excess of a carbon source accompanied by a deficit of other nutrient (nitrogen, phosphorus, magnesium, among others) [1–2]. This kind of biopolyester can behave as thermoplastics or elastomers (depending on their chemical structure) with physical, chemical, and mechanical properties similar to those of petroleum-based plastics such as polypropylene [1–2]. PHAs, unlike plastics of petrochemical origin, are obtained from renewable carbon sources and are biodegradable, which is a great advantage. In addition, they are biocompatible and can be used in the biomedical field. The PHAs' production process has been focused on the use of stirred tank

bioreactors. The airlift-type bioreactor has been less used for this purpose, though it is an interesting alternative as demonstrated by some reports, in which biomass production and polymer accumulation showed encouraging data [3–6]. Airlift reactors promote pneumatical agitation with flows in the defined cycle. Among their advantages are the absence of moving parts, low shear stresses, low energy consumption, good mixing, and efficient mass transfer. Moreover, they are easy to manufacture and scale up. The agitation and mixing in this type of reactor occurs using an internal or external loop. As for the internal loop airlift, the reactor consists of two concentric tubes, with an ascent zone of the liquid with gas, and a descent zone where the liquid is relatively gas-free. The enhanced performance of an airlift bioreactor for aerobic fermentation processes depends on its hydrodynamic behavior. This analysis is based on the evaluation of dynamic parameters such as the mixing time and the gas-liquid interfacial area (calculated from the bubble size and the gas retention value). The operation variables most important for the bioreactor performance include the disperser position (the distance on the *y-axis* between the air disperser and the drag tube), airflow, and volume of the liquid [7–10].

Besides the use of low-energy consuming bioreactors, such as the airlift-type for producing PHAs, another important fermentation strategy to achieve a competitive process, is based on the formulation of culture media from inexpensive carbon sources, such as sugarcane molasses.

It is a sugar-rich viscous liquid generated after the sugar extraction from the sugarcane. The main carbohydrate in molasses is sucrose, followed by some fructose and glucose. In addition, molasses contains minerals and vitamins in small concentrations [11]. They are generated in many tropical countries, where sugarcane is a major crop. In Mexico (2018), 51 sugarcane mills produced around 5.8 Mtons of sugar and 1.76 Mtons of molasses [12], so they are a promising, abundant, and available substrate for the cost-effective production of PHAs. This has been investigated using some bacteria such as *Pseudomonas fluorescens* A2a5, *Bacillus megaterium* ATCC6748, *Cupriavidus necator* DSM 545 [13], *Bacillus cereus* SS105, *Ralstonia eutropha* ATCC 17699 [14], *Pseudomonas corrugata*, *B. cereus SPV* [15], *B. subtilis* AMN1, mixed cultures [16], *B.megaterium* BA-019, *B. flexus* AZU-A2, *B. subtilis* BPP-19, and *Clostridium beijerinckii* ASU10 [17]. However, molasses might contain high concentrations of growth inhibitors (phenolic compounds, melanoidins, metal ions, etc.), so this substrate must be pretreated before fermentation to reduce the inhibitory effect it has

on many PHAs-producing bacteria [17–18]. Another issue about using molasses as a carbon source is that only a few PHA-producing bacteria can metabolize the sucrose contained in it. Thus, it is necessary to genetically modify such bacteria for them to express the gene that encodes for the enzyme ˅-fructofuranosidase, which is responsible for the hydrolysis of sucrose (a critical step to metabolize this disaccharide) [18].

On the other hand, *Stenotrophomonas rhizophila* (a bacterium isolated by our group [19], used in the present research) has demonstrated the ability to assimilate sucrose (without requiring genetic modifications), and to grow in the presence of inhibitory compounds [20–22]. Therefore, it is expected to produce PHAs from molasses, without pretreatment.

Considering the above, the present research is focused on the hydrodynamic characterization of an internal loop airlift bioreactor and its use for cultivating *S. rhizophila* using molasses as a low-cost substrate. It is expected that by changing the operation variables previously mentioned, an appropriate configuration for increasing the interfacial area and decreasing mixing time will be attained, which would favor the growth and biopolymer by *S. rhizophila*.

MATERIAL AND METHODS

Airlift bioreactor design and construction

The stainless steel T304 airlift bioreactor built was an internal loop concentric tube type, designed to operate with a maximum working volume of 2.4 L. Its geometric ratios are 0.33 between the diameter of the drag tube and the diameter of the outer tube, 6.56 between the height and diameter of the outer tube, and 0.57 between the heights of the inner and outer tubes [23–25], as shown in Fig. 1. This design was conceived based on the recommended ratios for airlift reactors (less than 10 liters) found in the literature: 0.3, between the diameter of the drag tube and the diameter of the outer tube; 6, between the height and diameter of the outer tube; and 0.6, between the heights of the inner and outer tubes [24]. The versatility of the airlift reactor's design makes it flexible because the modification of the drag tube is simple. Despite the ratio differences (with respect to that reported in the literature), the functionality of the airlift bioreactor built was considered appropriate according to the results obtained from the hydrodynamic analysis. It is worth mentioning that stainless steel polished surfaces influence gas retention and liquid velocity, as they contribute to a better performance of the pneumatic transport for the phases inside the bioreactor [24–27]. The airflow necessary for the pneumatic transport was

CLIFTON-GARCÍA *et.al.*: USE OF AN INTERNAL LOOP AIRLIFT…

Chem. Ind. Chem. Eng. Q. 31 (1) 71−82 (2025)

provided by compressed air at 2 bar, sterilized through a 0.2 µm pore size membrane filter. It was controlled with a rotameter varying from 0.5 to 1.5 vvm. The control of the temperature at 30 °C was achieved with a heating blanket. On the bioreactor top lid, a condenser was placed to reduce the amount of water lost due to evaporation during fermentation, while at the bioreactor base, there were two valves: one used to sample and another to discharge.
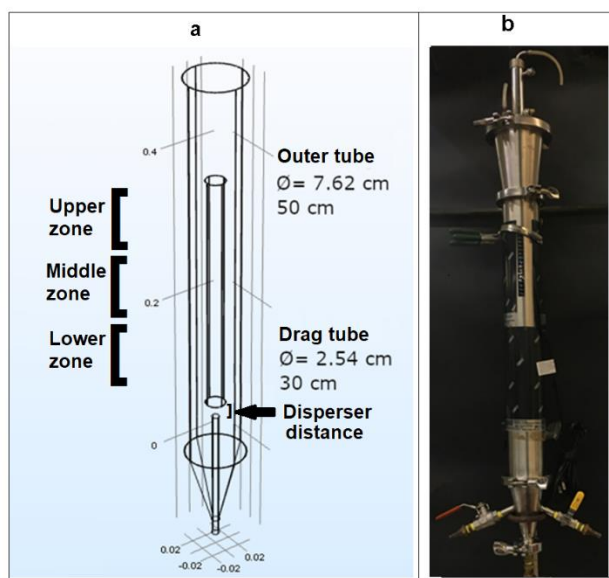

Figure 1. Airlift reactor. (a) design; (b) stainless steel.

Hydrodynamic characterization

The hydrodynamic operation of the bioreactor was investigated according to a central composite design (CCD), which is a methodology used to explore the impact of independent variables (experimental factors) on response variables. Aeration flow, liquid volume, and disperser position, were the three independent variables studied, and their influence on two response variables was investigated: the interfacial area and mixing time. The CCD involves 2^3 factorial runs and a center point [28] (Table 1), resulting in nine experiments (Table 2). The confidence level used was 95%. This response surface optimization technique was applied to maximize the interfacial area and minimize the mixing time. The *STAGRAPHICS Centurion* program was used for data analysis.

Table 1. Factors and levels studied by the CCD experimental design.

Level	Airflow (vvm)	Liquid volume (mL)	Disperser position [a] (mm)
-1	0.5	2200	5
0	1	2300	10
1	1.5	2400	15

[a] Distance on the *y-axis* between the air disperser and the drag tube

The interfacial area Eq. (1) was calculated from Eq. (2), Eq. (3), and the equivalent bubble diameter [7]:

Interfacial area: $A = \dfrac{6\varepsilon}{d(1-\varepsilon)}$ (1)

Retained volume: $\Delta V = V_{G+L} - V_L$ (2)

Volume expansion: $\varepsilon = \dfrac{\Delta V}{\Delta V + V_L}$ (3)

where A is the Interfacial area (cm^2), ε is the volume expansion, d is the bubble diameter (cm), ΔV is the liquid volume expansion (cm^3), V_L is the liquid volume (cm^3), and $V_{(G+L)}$ is the volume of gas and liquid (cm^3).

The bubble size was determined by taking photographic shots of the bubbles (dividing the drag tube into three zones, Fig. 1). Later, the equivalent diameter was calculated using the Regionprops in the MatLab program, for the analysis, the photograph was transformed into grayscale and then the image was transformed to binary [7]. It is worth mentioning that transparent glass tubes were adapted to the airlift fermenter, instead of stainless-steel tubes, to visualize and measure the bubbles, as well as to determine the mixing time, as follows. A tracer pulse method was used: A pulse of tracer (1 mL of 0.1 M NaOH or 1 mL of 0.1 M HCl, depending on pH dissolution) was added to the bioreactor filled with distilled water with phenolphthalein as an indicator, at which point the time count was begun. The time was stopped when the color change was complete throughout the reactor.

Molasses characterization

Sugar cane molasses was chosen as the carbon source, due to its high availability and low cost, it was provided by a local sugarcane mill. It was characterized for total sugars by the phenol-sulfuric method [29] and specific sugars by HPLC, using a Waters equipment with an IR 2914 detector and an HPX87P column (Biorad) at 85 °C. Water was used as the mobile phase with a flow rate of 0.6 mL/min. A molasses volume of 20 µL (previously diluted 1:200) was filtered through a 0.45 µm pore size membrane and analyzed. Total nitrogen and phosphate content was also determined (Kjeldahl and Vanadate-molybdate method, respectively) [30].

Bacterial strain and inoculum preparation

The fermentation process to produce PHAs, using the airlift bioreactor, was carried out by *S. rhizophila*, a PHA-producing bacteria with the ability to metabolize sucrose [19]. The inoculum was prepared using the next culture medium (sucrose medium): sucrose, 20 g/L; NaCl, 2 g/L; KH$_2$PO$_4$, 2.25 g/L; (NH$_4$)$_2$SO$_4$,10 g/L; MgSO$_4$x7H$_2$O, 0.5 g/L; CaCl$_2$xH$_2$O, 0.02 g/L; yeast extract, 5 g/L; and peptone, 5 g/L. The pH was adjusted to 7. The inoculum was

prepared as follows: 6 to10 isolated colonies growing in solid sucrose medium (agar, 16 g/L) were transferred to 10 mL of the same medium (120 mL Erlenmeyer flask) and incubated in a rotary shaker (24 h, 30 °C, and 150 rpm). Then, it was transferred to 230 mL of fresh medium (1L Erlenmeyer flask) and incubated as previously mentioned. Finally, this culture was used to inoculate the bioreactor.

Fed-batch culture using the airlift bioreactor and molasses

The culture medium consisted of: molasses (20 g/L of total sugars); NaCl, 2 g/L; KH_2PO_4, 2.25 g/L; $(NH_4)_2SO_4$, 10 g/L $MgSO_4 \cdot 7H_2O$, 0.5 g/L; $CaCl_2 \cdot xH_2O$, 0.02 g/L; yeast extract, 5 g/L; peptone, 5 g/L. The amounts of major nutrients present in the diluted molasses were (in g/L) nitrogen 0.21 and phosphorus 0.01. The pH was adjusted to 7. A volume of 2200 mL of molasses medium was sterilized and aseptically added to the airlift bioreactor (previously sterilized); then, 200 mL of inoculum was added. The working volume (2400 mL) was set according to the results from the hydrodynamic study, as well as the airflow (1.5 vvm), and the disperser position (5 mm). The air was filtered using a Midistart 2000 sterile filter (0.20 µm PTFE, Sartorius); temperature and pH were maintained at 30 °C and 7, respectively.

Considering that a volume of 240 mL/day was lost (due to water evaporation and sampling) and that a nutrient imbalance condition was needed for PHA biosynthesis, a feeding strategy for gradually reaching a high C:N ratio, and simultaneously compensating the water loss was implemented (maintaining a constant volume). For that purpose, pulses of 120 mL of concentrated molasses (200 g/L), without any other culture medium's component, were added every 12 h. Five samples per day (20 mL each) were withdrawn and analyzed to determine: total sugars, total biomass, polymer, and ammonium concentration.

Quantification of fermentation products and substrates

The determination of total carbohydrates was performed using the phenol-sulfuric method, and the specific sugars by HPLC as previously described.

The ammonium concentration was measured with an ammonium electrode (Cole-Parmer, 27504), and then used to calculate the C:N ratio in the culture medium.

For biomass quantification (denominated as total biomass), the samples were centrifuged for 30 min at 2200 *g*, then, the biomass pellet was washed with a physiological solution and centrifuged again. The washed biomass was freeze-dried (Labconco) and

weighed. The biomass resulting after PHB extraction was also weighted and represents the catalytic biomass (denominated as residual biomass in the present work).

For PHB quantification, the freeze-dried total biomass was suspended in 96% ethanol, at a 1:5 ratio (w/v), with agitation for 24 h. Subsequently, it was recovered by centrifugation and allowed to dry at room temperature for 24 h. The dry total biomass was resuspended in chloroform (1:5 w/v) in a glass flask with a magnetic stirrer (24 h). After that, the residual biomass was removed by filtration, and the chloroform was evaporated until a PHB film was formed and weighed (this step was performed twice). Finally, the remaining PHA inside the cells was determined by the crotonic acid method [31].

The biomass production data along the culture was fitted to a modified Gompertz equation (Eq. 4) to determine the kinetic parameters, using the Nonlinear Least Squares method to calculate the curve in MatLab [32].

$$X = L + C \cdot e^{-e^{-B(t-\mu_{max})}} \tag{4}$$

where X is the biomass (g/L). L is the lower asymptote value, C is the difference between the curve asymptotes, B is the relative growth rate, t is the time (h) and μ_{max} is the maximum growth rate (1/h).

An exponential equation (Eq. 5) was used to predict the behavior of PHB production [33–34].

$$PHA = \frac{PHA_0 e^{\alpha t}}{1 - \left(\dfrac{PHA_0}{PHA_m}\right)\left(1 - e^{\alpha t}\right)} \tag{5}$$

where PHA_0 is the initial PHA (g/L), PHA_m is the maximum PHA (g/L), α is the accumulation rate (1/h) and t is the time (h).

Polymer characterization techniques
Nuclear Magnetic Resonance (NMR)

NMR proton (^1H) and carbon (^{13}C) spectra of the polymer were obtained using a benchtop Magritek Spinsolve 80 (80 MHz) spectrometer. The PHAs sample (5 mg) was dissolved in deuterated chloroform (0.7 mL) in a 5 mm diameter NMR tube and measured at room temperature.

Differential scanning calorimetry (DSC)

DSC analysis was performed by placing 5.67 mg of PHAs sample in aluminum capsules. The test was conducted at a heating rate of 10 °C/min from -20 to 182°C under nitrogen flow using a Discovery DSCQ

200 equipment. From the thermograms, the peak of the melting temperature (T_m) was obtained after a second melt of the sample, and the crystallinity (X_c) was calculated Eq. (6):

$$X_C(\%) = \frac{\Delta H_{PHA} \cdot 100}{\Delta H_{ref}}$$
(6)

where X_C is the Crystallinity percentage (%), ΔH_m is the experimental heat of fusion and ΔH_{ref} is the heat of fusion (146 J/g) of fully crystalline PHA [35]. The cooling of the sample was obtained at the crystallization temperatures of the sample.

Molecular weight

For molecular weight determination, the PHB sample was dissolved in chloroform (1.5 mg/mL) and then filtered (0.45 μm). The equipment used was a Waters HPLC with an IR 2914 detector, using the GPC HR4 styragel column at 40°C. The mobile phase was NN-dimethylformamide (flow of 1 mL/min) and a sample volume of 20 μL was injected. The calibration curve was performed using polystyrene standards (Fluka 81437) with a molecular weight of 400 to 2,000,000 Da.

RESULTS AND DISCUSSION

Hydrodynamic characterization

In Table 2, the results from each experiment for the response variable, interfacial area, are presented. The airflow and the volume of liquid had a significant effect individually (Fig. S1a, Supplementary material): a greater interfacial area was found when setting the airflow or the volume of liquid at a high level (+1) which is a favorable response for the oxygen transference. On the other hand, the disperser distance does not have a significant effect by itself, but it does when interacting with the liquid volume (Fig. S1a): at disperser position (-1) combined with liquid volume (+1), the highest interfacial area is achieved. Thus, an increase in the airflow and liquid volume results in a rise in the interfacial area, which favors the oxygen transference, given the greater area for mass transference.

Table 2. Interfacial area and mixing time results according to the CCD experimental design (two replicates).

Experiment	Experimental Factors and levels			Response variables Interfacial area (mm^2)		Mixing time (s)	
	Airflow	Liquid volume	Disperser position	R1	R2	R1	R2
1	0	0	0	2489	2031	11.8	11.3
2	-1	-1	-1	697	705	15.9	16.1
3	1	-1	-1	3363	3650	8.1	7.8
4	-1	1	-1	1174	1301	11.2	11.2
5	1	1	-1	4506	4073	5.4	5.2
6	-1	-1	1	1001	975	15.4	17.4
7	1	-1	1	4099	3963	8.8	12.2
8	-1	1	1	1198	1157	12.2	12.1
9	1	1	1	3706	3927	6.1	6.4

Eq. (7), is the multiple regression equation that relates the response variable, interfacial area (A), to the three independent variables: flow (F), volume (V_L), and disperser distance (Dd). The lack of fit test for this equation confirms a linear association between the independent and response variables

$$A = 2474 + 1472F + 173.8V_L + 64.84D_d - 7.681FV_L + 8.045D_d - 156.0V_L D_d - 69.15FV_L D_d$$
(7)

where A is the Interfacial area (cm^2), F is the airflow (volume of air per volume of liquid per minute (vvm), V_L is the liquid volume (cm^3), and D_d is the disperser distance (mm).

Thus, it was found that, with the values of airflow (+1), volume of liquid (+1), and disperser position (-1), an area value of 4266 mm^2 was achieved. The main effect was attributed to the airflow (Fig. S1). A similar result was reported by García-Albuín *et al.* [7]: an increase in the airflow increased the interfacial area.

Since the interfacial area (Eq.1) depends on the retained volume (Eq. 2) and the bubble size, those were analyzed. As for the retained volume behavior (Fig. 2), it is directly proportional to the airflow [26–27, 36–37]: the experiments in which the airflow used was at the low level (-1) (two, four, six and eight) presented a lower retained volume than the experiments where the airflow was set at the high level (+1) (three, five, seven and nine). Meanwhile, in experiment one, the retained volume was an intermediate value since the airflow was set at the center point (0).

Regarding the bubble size, pictures were taken in the different reactor zones (lower, middle, and upper) (Fig. 1a). A change in the size of the bubbles as they ascended the drag tube was observed, it increased in the upper zone due to coalescence. The distribution of the equivalent diameters of the bubbles in each
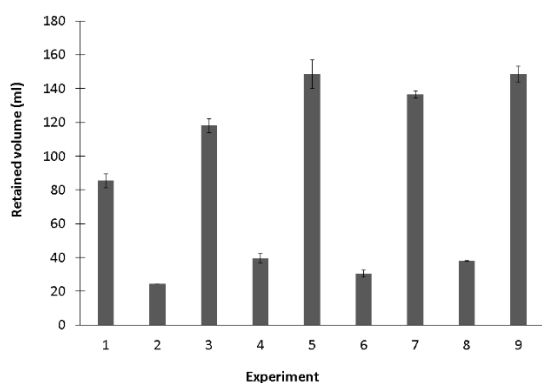
Figure 2. Behavior of the volume of retained air in each experiment (Table 2).

experiment is shown in Fig. 3. The bubble size distribution was more uniform between the different levels of the response factors, compared to those obtained by García-Abuín *et al.* [7] reporting bubble diameters of 6.2 and 9.5 mm (with airflows of 0.07 and 0.17 vvm), in 3.5 L airlift reactor (gas flows of 15 L/h and 36 L/h, respectively). The difference in the bubble diameter between the three zones is significant compared to the variation between the replicates of the different experiments.
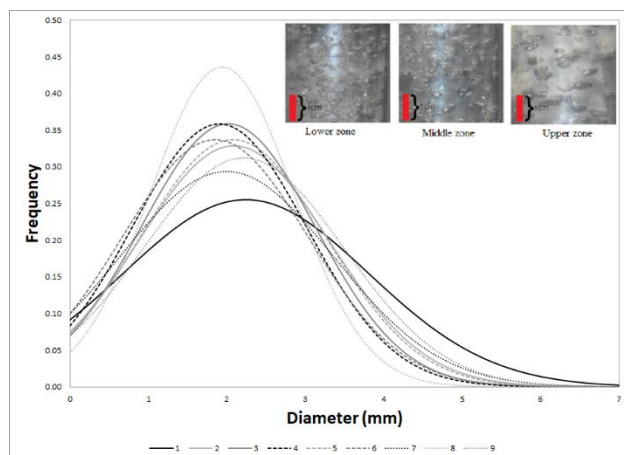

Figure 3. Bubble size distribution resulted in each experiment (Table 2).

Concerning the other response variable studied, mixing time, the results obtained from each experiment are shown in Table 2. The three independent variables tested individually (aeration flow, liquid volume, and disperser position) have a significant effect on this variable (Fig.S1b). The airflow is the factor that exerted the main influence (Fig. S1b), although liquid volume and disperser distance are also important for achieving a homogeneous system in the shortest time (Fig. S1b). Increasing the airflow (+1) results in improved

homogeneity, conversely, using a larger liquid volume (+1) decreases the mixing time within the tested range. About the disperser position, better mixing is favored when it is closer to the drag tube (-1), indicating that positioning the disperser close to the inlet of the drag tube is more efficient. The interaction between the independent variables on the mixing time was not significant (Fig. S1b).

Eq. (8), is the multiple regression equation that relates the three independent variables: flow (F), volume (V_L), and disperser distance (Dd), to the response variable, mixing time (t_m). The lack-of-fit test for this equation confirmed a linear relationship between the independent and response variables.

$$t_m = 10.8 - 3.22F - 1.99V_L + 0.603D_d + 0.264FV_L + 0.257FD_d - 0.137V_LD_d - 0.266FV_LD_d$$
$$2474 + 1472F + 173.8V_L + 64.84D_d - 7.681FV_L + 8.045D_d - 156.0V_LD_d - 69.15FV_LD_d \quad (8)$$

where t_m is the mixing time (s), F is the airflow (volume of air per volume of liquid per minute (vvm)), V_L is the liquid volume (cm³), and D_d is the disperser distance (mm).

The faster mixing time (5.4 s) occurred in the next variables configuration: airflow (+1) 1.5 vvm, liquid volume (+1) 2400 mL, and distance between the disperser and the drag tube (-1) 5 mm. On the other hand, the slowest mixing time (16.4 s) was obtained in the following combination: airflow 0.5 vvm, liquid volume 2200 mL, and disperser position 15 mm (Table 2). The best results for both response variables, the interfacial area and mixing time, were obtained with high airflow (+1), corresponding to experiments three, five, seven, and nine (Table 2).

The optimization (according to the statistical analysis, within the ranges studied) to increase the interfacial area and decrease the mixing time resulted in the following conditions: airflow of 1.5 vvm (3.6 L/min); liquid volume of 2400 mL; and disperser distance of 5 mm (Fig. S2).

Chemical composition of molasses

The characterization of molasses (raw, not diluted) shows a total sugar content of 456.3 g/L (sucrose, 91%; fructose, 6%; and glucose, 3%); and the total nitrogen and phosphorous concentrations were (g/L): 4.8 and 0.28, respectively. Those values are within the range reported for sugarcane molasses: total sugars 200-500 g/L, nitrogen 2.5–8.5, and phosphorus 0.25–1.8 [38–41]. It was important to point out that molasses was diluted to reach a final concentration of 20 g/L of total sugars and then used as a base for the culture medium. Therefore, the

amounts of phosphorous and nitrogen in such molasses were (g/L) 0.21 and 0.01, which are low values to be considered as an interference for the PHB accumulation process.

Fed-batch culture using the airlift bioreactor and molasses

In Table 3, the results from the fermentation, including major kinetic parameters are shown, as well as those from other similar studies, using other strains, carbon sources, and bioreactor types. Fig. 4a shows the total biomass production and the PHB

accumulation kinetics of *S. rhizophila* growing in the airlift bioreactor with molasses as a carbon source. As described in the materials and methods section, molasses were fed in pulses every 12 h, the added also compensated for the water lost due to evaporation caused by aeration, maintaining a constant volume within the reactor. A modified Gompertz equation (Eq. 4) was used to fit the biomass production experimental data (Fig. 4c), obtaining an R-square value of 98.3%. For PHB accumulation, a fitting to an exponential equation (Eq. 5) was performed (Fig. 4d), with an R-square value of 96.1%.

Table 3. PHAs production from sugarcane molasses or sucrose, in airlift and stirred tank bioreactors.

| Bioreactor Type/Volume (L)		Carbon source	Strain	Total biomass (g/L)	PHAs (g/L)	PHAs (%)	Productivity (PHAg/Lh)	$Y_{x/s}$ (g/g)	μ_{max} (1/h)	Reference
Airlift	2.4	Molasses	*Stenotrophomonas rhizophila*	65.4	39.3	60	0.73	0.39	0.27	This work
	7	Starch hydrolizate	*Halomonas boliviensis*	9.2	5.2	56	0.21	0.43	0.45	[5]
	10	Glucose+fructose	*Ralstonia eutropha*	4.1	1.5	37	0.6	-	0.32	[6]
	4	Sucrose	*Azohydromonas australica*	10.8	7.8	73	0.21	0.43	0.45	[3]
	8	Sucrose	*Burkholderia sacchari*	150.0	63.0	42	1.07	0.4	0.4	[4]
Stirred tank	7	Sucrose	*Azohydromonas australica*	27.9	20.6	73	0.3	0.28	-	[42]
	3	Sucrose	*Burkholderia sacchari*	36.5	20.4	56	1.29	0.18	0.23	[43]
	-	Sucrose	*Azohydromonas lata*	142.0	68.4	50	3.97	-	-	[44]
	3	Sucrose	*Burkholderia sacchari*	74.6	53.7	72	1.29	0.38	0.18	[43]
	5	Molasses	*Pseudomonas fluorescens*	32.0	22.4	70	0.23	-	-	[45]
	3	Molasses	*Azohydromonas lata*	-	5.7	68	0.16	-	-	[46]
	10	Molasses	*Bacillus megaterium*	32.5	8.8	26.9	0.73	0.69	0.29	[47]
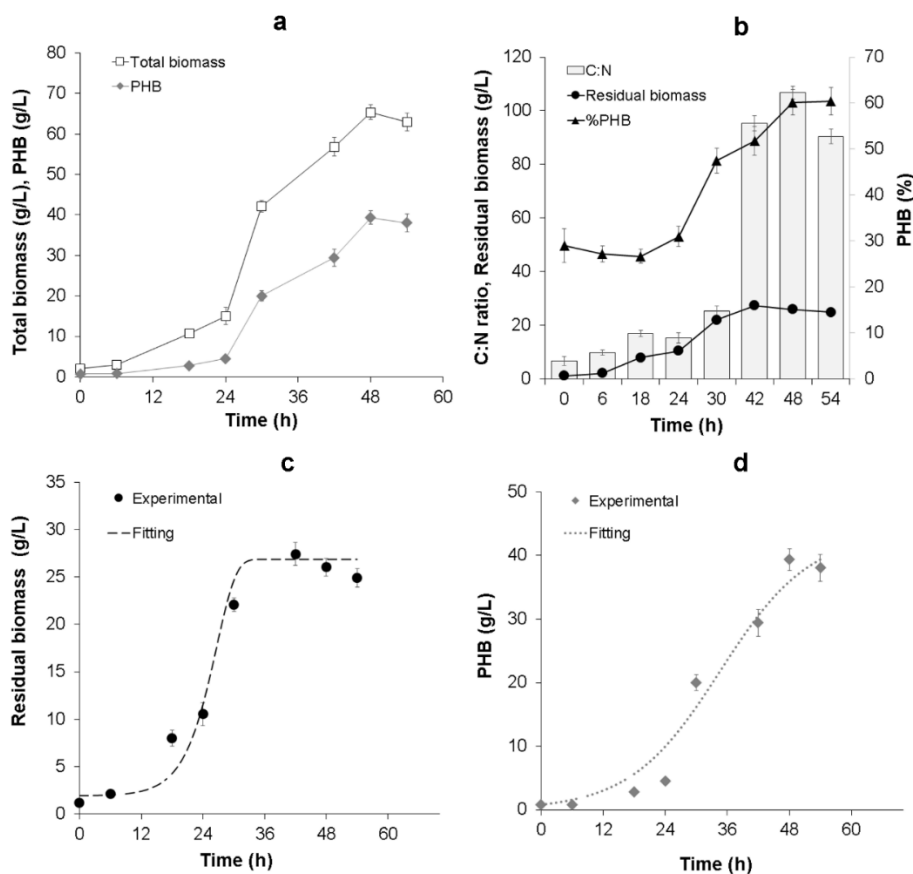
Figure 4. Kinetic profile for biomass production and PHA accumulation by S. rhizophila growing in the airlift bioreactor (fed-batch).

CLIFTON-GARCÍA *et.al.*: USE OF AN INTERNAL LOOP AIRLIFT...

Chem. Ind. Chem. Eng. Q. 31 (1) 71−82 (2025)

It is observed (Fig. 4a) that during the first 24 h, bacterial growth is slow. Then, the exponential growth phase begins and continues until 30 h of culture. After this point, bacterial growth slows down because of the progressive depletion of nutrients other than the carbon source, as only concentrated molasses (without any other nutrient) was periodically fed into the bioreactor, as pulses. From 30 h of culture, the increment in total biomass observed is mostly due to the increment in PHB accumulation within the cell (Fig. 4a). This is more clearly observed in Fig. 4b. where the residual biomass concentration (catalytic biomass) remains almost constant from the 30 h to 54 h of culture, while the percentage of PHB rises, from 31 (at 24 h) to 60.2. It is interesting to point out that *S.rhizophila* synthesizes the polymer before a low nitrogen concentration in the culture medium occurs (0–24 h)(Fig. 4b), though the accumulation increased considerably upon nitrogen limitation (high C:N due to the feeding/consumption of molasses and the continuous ammonia intake). The behavior observed in Fig. 4b is very similar to that presented by *A. latus* DSM1123: a high polymer content at nitrogen-sufficient conditions (around 50%), and an even higher accumulation of (90%) under nitrogen-limiting conditions [48]. Related to the above, Kiselev *et. al* [49] (using hydrolyzed sugar beet molasses to produce PHB by *C. necator*) reported that the amount of polymer accumulated before nitrogen depletion was around 30% (24 h), which is similar to our results. Likewise, after that point the C:N ratio raised, triggering a higher intracellular PHB content (75%) [49]. In this regard, studies on the effect of the C:N ratio on the PHAs accumulation by different bacteria, confirmed that the polymer biosynthesis is stimulated when the C:N ratio rises: *A. australica*, from 41.6 to 60 (PHAs 73%) using sucrose [3]; *Azotobacter chroococcum* 6B, from 68.9 to 137.7 (PHB 63.5%) using glucose [50]; and *Cupriavidus necator*, from 36.1 to 360 (PHAs 80%) on the use of rice hydrolysates [51]. In Fig. 4b, it is observed that the C:N ratio changed from 7:1 (initial condition) to 107:1 (48 h) due to nitrogen source consumption in combination with the carbon source accumulation (which is a regular feature of PHAs production in fed-batch culture). For *S.rhizophila*, the PHB accumulation increased at C:N ratios around 100.

The maximum total biomass concentration, PHB production, and PHB accumulation were: 65.4 g/L, 39.3 g/L, and 60.2 (g PHB/100 g dry biomass). Compared to the same bacterium, the only result reported is from flask cultures: 1.7 g/L of biomass and a PHB content of 13.7% [19]. The results from the present research are higher than those reported for other strains cultivated in similar culture systems (airlift bioreactor, fed-batch culture), such as *Halomonas*

boliviensis, *Ralstonia eutropha* and *Azoydromonas australica* [3, 5–6], as observed in Table 3. On the other hand, are lower than those presented by *Burkoderia sacchari* growing from sucrose, in an airlift bioreactor [4] (Table 3). However, it is important to remark that in that research; an aeration rate of 12.6 vvm was used, which is notably higher (8 times) than that used in the present research (1.5 vvm). *S. rhizophila* presented a μ_{max} of 0.27/h, a total biomass and PHB yields on substrate ($Y_{X/S}$ and $Y_{P/S}$) of 0.39 g/g, and 0.23 g/g, respectively. Those values are within the range reported for other PHAs-producing strains cultivated in airlift bioreactors, such as *R. eutropha* and *A. australica* (Table 3) [3,6], yet it has to be mentioned that it was achieved at a low aeration rate. The PHB accumulation rate was 0.1151/h, and the $PHAs_m$ (the maximum PHB accumulation expected) was 43.64 g/L, according to the results from the exponential equation used to fit the experimental data (Eq. 5).

As for the use of sugar cane molasses or sucrose as the carbon source to produce PHAs by other bacteria (but cultured in stirred tank reactors) the ranges of biomass production and polymer accumulation are variable (Table 3), yet the production of PHB by *S. rhizophila* from molasses is in the higher range, with the advantages of using a low-energy consuming airlift bioreactor.

Polymer characterization

In Fig. 5a, it is shown the ^{1}H NMR spectrum of the polymer obtained (see chemical structure). Here, PHB repeat unit presence is observed by its classical hydrogen signals pattern of CH at 5.5, CH_2 at 2.5 and CH_3 at 1.3 ppm (in the corresponding integration ratio of 1:2:3). Although CH and CH_3 signals showed the expected multiplicity as sextet and doublet, signal of CH_2 did not split as a doublet of quartet (as reported) [52–55] due to the low magnetic field (80 MHz NMR spectrometer) used in the measurement. However, in this case, the important data already demonstrated the identity of the polymer produced: poly-3-hydroxybutyrate. This identity is also corroborated by four carbon signals shown in the ^{13}C NMR spectrum of Fig. 5b. Here, the signal at 168 ppm corresponded to carbonyl carbon from the ester group (C1), and its aliphatic carbon backbone is demonstrated in the signals at 66 (C3), 39 (C2) and 18 ppm (C4) associated to methine, methylene, and methyl groups, respectively.

The results of melting temperature (T_m) were 170 °C (ΔH=82.3 J/g) and the percentage of crystallinity (X_C) was 56.4. The thermograms obtained were as those reported in other PHB production studies, indicating a similar thermal behavior. The
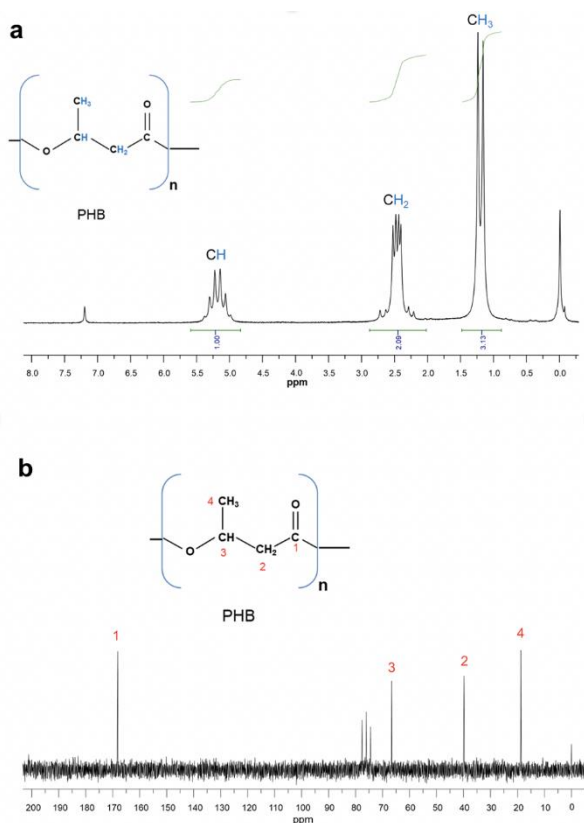
CLIFTON-GARCÍA *et.al.*: USE OF AN INTERNAL LOOP AIRLIFT…

Chem. Ind. Chem. Eng. Q. 31 (1) 71–82 (2025)

Figure 5. ^1H NMR (a) and ^{13}C NMR (b) spectra of the PHAs obtained.

values obtained match those reported for PHB. The T_m is from 164–180 °C and for crystallinity, the range is from 50% to 80% [34,56–58].

The number average molecular weight (M_n), weight average molecular weight (M_w), and the polydispersity index of the PHB produced by *S. rhizophila* were: 310 kDa, 735 kDa, and 2.37. This characteristic depends on several factors, such as the activity and type of PHAs synthetase present in the strain, the type and concentration of the carbon source used, and even the polymer extraction process and purification [59]. Thus, the molecular weight of PHAs produced by different strains under their specific culture conditions is variable. For example, PHAs produced by *Halomonas* sp. weigh 124 kDa (glycerol) in contrast to the 957 kDa of the polymer from *C. necator* DSM 545 (glycerol). Therefore, because the M_w of the polymer synthesized by *S. rhizophila* from molasses was 735 kDa, it is within the reported ranges previously mentioned. The molecular weight of PHAs is directly related to other mechanical and physical characteristics. Depending on their intended use, it will be their desirable molecular weight.

CONCLUSION

The hydrodynamic characterization of the airlift

bioreactor allowed a configuration to minimize the mixing time and maximize the interfacial area. Under such conditions, using a low airflow, and a feeding strategy based on liquid loss compensation, *S. rhizophila* achieved a relevant biomass production with a high polymer accumulation. Thus, these results confirmed that the low-energy consuming airlift bioreactors are suitable for PHA production and that *S. rhizophila* is a promising bacterium to produce PHB from molasses. The next step is to evaluate its ability to produce copolymers. Further studies are necessary to enhance this process: the effect of increasing the molasses concentration; optimization of the culture medium and culture conditions (i.e. pH and temperature); the PHB accumulation under different nutrient-limiting conditions (i.e phosphorous); and the implementation of other operation modes (i.e., perfusion). In addition, the modeling and simulation of the bioreactor, as well as the scale-up studies are also important aspects to consider.

NOMENCLATURE

A	Interfacial area (cm^2)
B	Relative growth rate
C	Difference between the curve asymptotes
Dd	Disperser distance (mm)
d	Bubble diameter (cm)
F	Airflow (volume of air per volume of liquid per minute (vvm))
L	Lower asymptote value
PHA_0	PHA initial (g/L)
PHA_m	PHA maximum (g/L)
t	Time (h)
t_m	Mixing time (s)
V_L	Liquid volume (cm^3)
$V_{(G+L)}$	Volume of gas and liquid (cm^3)
X	Biomass (g/L)
X_C	Crystallinity percentage (%)
Greek letters	
α	Accumulation rate (/h)
ε	Volume expansion (Holdup)
μ_{max}	Maximum growth rate (/h)
ΔH_{PHA}	Experimental fusion enthalpy (J/g)
ΔH_{ref}	Reference melting enthalpy (146 J/g)
ΔV	Liquid volume expansion (cm^3)

REFERENCES

[1] Y. González García, J.C. Meza Contreras, O. González Reynoso, J.A. Córdova López, Rev. Int. de Contam. 29 (2013) 77–115. https://www.scielo.org.mx/pdf/rica/v29n1/v29n1a7.pdf.

[2] T. Keshavarz, I. Roy, Curr. Opin. Microbiol. 13 (2010) 321–326. https://doi.org/10.1016/j.mib.2010.02.006.

[3] G. Gahlawat, B. Sengupta, A.K. Srivastava, J. Ind.

Microbiol. Biotechnol. 39 (2012) 1377–1384. https://doi.org/10.1007/s10295-012-1138-5.

[4] J.G da C. Pradella, M.K Taciro, A.Y.P. Mateus, Bioresour. Technol. 101 (2010) 8355–8360. https://doi.org/10.1016/j.biortech.2010.05.046.

[5] P. Rivera-Terceros, E. Tito-Claros, S. Torrico, S. Carballo, D. Van-Thuoc, D. Quillaguamán, J. of Biol.Res-Thessaloniki. 22 (2015) 8. https://doi.org/10.1186/s40709-015-0031-6.

[6] L.Z. Tavares, E.S da Silva, J.G da C. Pradella, Biochem. Eng. J. 18 (2004) 21–31. https://doi.org/10.1016/S1369-703X(03)00117-7.

[7] A. García-Abuín, D. Gómez-Díaz, ACI. 1 (2010) 2 25–36. https://api.semanticscholar.org/CorpusID:93351577 ISSN-e0718-8706.

[8] G.B. Hurtado, A.M. Otálvaro, P.G. Duarte, Rev. Colomb. Biotecnol. 15 (2013) 106–114. https://doi.org/10.15446/rev.colomb.biote.v15n2.41272.

[9] J.C. Merchuk, Can. J. Chem. Eng. 81 (2003) 324–337. https://doi.org/10.1002/cjce.5450810301.

[10] G. Quijano, S. Revah, M. Gutiérrez-Rojas, L.B. Flores-Cotera, F. Thalasso, Process Biochem. 44 (2009) 619–624. https://doi.org/10.1016/j.procbio.2009.01.015.

[11] L. Jamir, V. Kumar, J. Kaur, S. Kumar, H. Singh, H. Environ. Technol. Rev. 10 (2021) 1, 131–142. https://doi.org/10.1080/21622515.2021.1892203.

[12] J. Aburto, E. Martínez-Hernández, Front. Energy Res. 8 (2021) 612647. https://doi.org/10.3389/fenrg.2020.612647.

[13] K.Y. Sen, S. Baidurah, Curr. Opin. Green Sustainable Chem. 27 (2021) 100412. https://doi.org/10.1016/j.cogsc.2020.100412.

[14] J. Wang, S. Liu, J. Huang, Z. Qu, Bioresour. Technol. 342 (2021) 126008. https://doi.org/10.1016/j.biortech.2021.126008.

[15] A.T. Adeleye, C.K. Odoh, O.C. Enudi, O.O. Banjoko, O. O. Osiboye, E.T. Odediran, H. Louis, Process Biochem. 96 (2020)174–193. https://doi.org/10.1016/j.procbio.2020.05.032.

[16] S. Zhang, J. Wang, H. Jiang, Food Chem. 346 (2021) 128860. https://doi.org/10.1016/j.foodchem.2020.128860.

[17] P. Marciniak, J. Możejko-Ciesielska, Polymers 13 (2021) 11, 1731. https://doi.org/10.3390/polym13111731.

[18] S. Y. Jo, Y.J. Sohn, S.Y. Park, J. Son, J.I. Yoo, K.A. Baritugo, S.J. Park, Korean J. Chem. Eng.38 (2021) 7, 1452–1459. https://doi.org/10.1007/s11814-021-0783-7.

[19] B. Clifton-García, O. González-Reynoso, J.R. Robledo-Ortiz, J. Villafaña-Rojas, Y. González-García, Lett. Appl. Microbiol. 70 (2020) 300–309. https://doi.org/10.1111/lam.13272.

[20] J. Gao, S. Wu, Y. Liu, S. Wu, C. Jiang, X. Li, X. Zhuang, X. Environ. Pollut. 263 (2020) 114622. https://doi.org/10.1016/j.envpol.2020.114622.

[21] S.P. Kumar, B.K. Manjunatha, Sci., Technol. Arts Res. J. 4 (2015) 3, 139–144. https://www.ajol.info/index.php/star/article/view/142953.

[22] B.N. Sánchez-Pérez, A. Zenteno-Rojas, C.I. Rincón-Molina, V.M. Ruíz-Valdiviezo, F.A. Gutiérrez-Miceli, M. A., Vences-Guzmán, R. Rincón-Rosales, Water, Air, Soil

[23] M. Moo-Young, Comprehensive Biotechnology, Academic Press, Burlington (2011), p.199. https://doi.org/10.1016/B978-0-08-088504-9.00095-7.

[24] E.R Gouveia, C.O. Hokka, A.C. Badino-Jr, Braz. J. Chem. Eng. 20 (2003) 363–374. https://doi.org/10.1590/S0104-66322003000400004.

[25] G.C. Noverón, (2009). [Thesis, Instituto Politécnico Nacional] https://tesis.ipn.mx/bitstream/handle/123456789/23318/Nover%c3%b3n%20Nava%20Guillermo%20Cuarto.pdf?sequence=1&isAllowed=y.

[26] M. Blažej, M. Kiša, J. Markoš, Chem. Eng. Process. 43 (2004) 1519–1527. https://doi.org/10.1016/j.cep.2004.02.003.

[27] J.C. Merchuk, M. Gluz, Encycl Bioprocess Technol. Eds M.C. Flickinger and S.W. Drew, New York (2002), p,320 https://doi.org/10.1002/0471250589.ebt029.

[28] M. Mourabet, A. El Rhilassi, H. El Boujaady, M. Bennani-Ziatni, A. Taitai, Arabian J. Chem. 10 (2017) 2, 3292–3302. https://doi.org/10.1016/j.arabjc.2013.12.028.

[29] M. DuBois, K.A. Gilles, J.K. Hamilton, P.A Rebers, Anal. Chem. 28 (1956) 350–356. https://doi.org/10.1021/ac60111a017.

[30] F.W. Gilcreas, Am J Public Health Nations Health. 56 (1966) 3, 387–388. https://ajph.aphapublications.org/doi/pdf/10.2105/AJPH.56.3.387.

[31] M.P. Rajankar, S. Ravindranathan, P.R. Rajamohanan, A. Raghunathan, Biol. Methods Protoc. 3 (2018) 1. https://doi.org/10.1093/biomethods/bpy007.

[32] C.M. Belda-Galbis, M.C. Pina-Pérez, J. Espinosa, A. Marco-Celdrán, A. Martínez, D. Rodrigo, Food Microbiol. 38 (2014) 56–61. https://doi.org/10.1016/j.fm.2013.08.009.

[33] M. Mahmoudi, M.S. Baei, G.D. Najafpour, F. Tabandeh, H. Eisazadeh, Afr. J. Biotechnol. 9 (2010) 3151–3157. https://doi.org/10.4314/ajb.v9i21.

[34] N. Moreno-Sarmiento, D. Malagón-Romero, J. Cortázar, A. Espinosa-Hernández, Univ. Scientiarum. 11 (2006) 41–48, https://www.virtualpro.co/revista/universitas-scientiarum-vol-11-no1/7

[35] E.V. Torres-Tello, J.R. Robledo-Ortíz, Y. González-García, A.A. Pérez-Fonseca, C.F. Jasso-Gastinel, E. Mendizábal, Ind. Crops Prod. 99 (2017) 117–125. https://doi.org/10.1016/j.indcrop.2017.01.035.

[36] M. Mohajerani, M. Mehrvar, F. Ein-Mozaffari, Can. J. Chem. Eng. 90 (2012) 1612–1631. https://doi.org/10.1002/cjce.20674.

[37] T. Zhang, C. Wei, C. Feng, J. Zhu, Bioresour. Technol. 104 (2012) 600–607. https://doi.org/10.1016/j.biortech.2011.11.008.

[38] F. Veana, J.L. Martínez-Hernández, C.N. Aguilar, R. Rodríguez-Herrera, G. Michelena, Braz. J. Microbiol. 45 (2014) 373–377. https://doi.org/10.1590/S1517-83822014000200002.

[39] K.P. Eliodório, G.C.D.G.E. Cunha, F.S.D.O. Lino, M.O.A. Sommer, A.K. Gombert, R. Giudici, T.O. Basso, Sci. Rep. 13 (2023) 1, 10567.

https://doi.org/10.1038/s41598-023-37618-8.

[40] M.S. Khatun, M. Hassanpour, S.I. Mussatto, M.D. Harrison, R.E. Speight, I.M. O'Hara, Z. Zhang, Bioresour. Bioprocess 8 (2021) 1–12. https://doi.org/10.1186/s40643-021-00438-7.

[41] Y.D. N'Guessan, E.M. Bedikou, K.A. Otchoumou, C.I. Assemian, A.C. Ehon, J. Sugarcane Res.11 (2023) 147–157. https://doi.org/10.37580/JSR.2021.2.11.147-157.

[42] M. Koller, Fermentation, 4 (2018) 30. https://doi.org/10.1007/s00449-013-0885-7.

[43] M. Miranda De Sousa Dias, M. Koller, D. Puppi, A. Morelli, F. Chiellini, G. Braunegg, Bioengineering, 4 (2017) 36. https://doi.org/10.3390/bioengineering4020036.

[44] W. Blunt, Levin, N. Cicek, Polymers, 10 (2018) 1197. https://doi.org/10.3390/polym10111197.

[45] L.R.Castilho, D.A. Mitchell, D.M. Freire, Biores. Technol. 100 (2009) 5996–6009. https://doi.org/10.1016/j.biortech.2009.03.088.

[46] M. Zafar, S.Kumar, A.K Dhiman,v J. Ind. Microbiol. Biotechnol., 39 (2012) 987–1001. https://doi.org/10.1007/s10295-012-1102-4.

[47] P. Kanjanachumpol, S. Kulpreecha, V. Tolieng, N. Thongchul. Bioprocess Biosyst. Eng. 36 (2013)1463–74. https://doi.org/10.1007/s00449-013-0885-7.

[48] F. Wang, S.Y. Lee, Appl. Environ. Microbiol. 63 (1997) 9 3703–3706. https://doi.org/10.1128/aem.63.9.3703-3706.1997.

[49] E.G. Kiselev, A.V. Demidenko, N.O. Zhila, E.I. Shishatskaya, T.G. Volova, Bioengineering 9 (2022) 154. https://doi.org/10.3390/bioengineering9040154,

[50] J.C. Quagliano, S.S. Miyazaki, Appl. Microbiol. Biotechnol. 48 (1997) 662–664. https://doi.org/10.1007/s002530051112,

[51] J. Ahn, E.H. Jho, K. Nam, Environ. Eng. Res. 20 (2015) 246–253. https://doi.org/10.4491/eer.2015.055.

[52] A. Bhattacharyya, A. Pramanik, S.K. Maji, S. Haldar, U.K. Mukhopadhyay, J. Mukherjee, AMB Expr. 2 (2012) 34. https://doi.org/10.1186/2191-0855-2-34.

[53] C.K. Chang, H.M. Wang, J. Lan, Polymers. 10 (2018) 355. https://doi.org/10.3390/polym10040355.

[54] W.H. Lee, C.Y. Loo, C.T. Nomura, K. Sudesh, Bioresour. Technol. 99 (2008) 6844–6851. https://doi.org/10.1016/j.biortech.2008.01.051.

[55] R. Li, Y. Jiang, X. Wang, J. Yang, Y. Gao, X. Zi, X. Zhang, H. Gao, N. Hu, Springer Plus. 2 (2013) 335. https://doi.org/10.1186/2193-1801-2-335,

[56] A.J. Dos Santos, L.V. Oliveira Dalla Valentina, A.A. Hidalgo Schulz, M.A. Tomaz Duarte, Part I. Ing. Cienc. 13 (2017) 269–298. https://doi.org/10.17230/ingciencia.13.26.10.

[57] M. Koller, L. Marsalek, Appl. Food Biotechnol. 2 (2015) 3–15. https://doi.org/10.22037/afb.v2i3.8271.

[58] H. Lu, S.A. Madbouly, J.A. Schrader, M.R- Kessler, D. Grewell, W.R. Graves, RSC Adv. 4 (2014) 39802–39808. https://doi.org/10.1039/C4RA04455J.

[59] C. Insomphun, S. Kobayashi, T. Fujiki, K. Numata, AMB Expr. 6 (2016) 29. https://doi.org/10.1186/s13568-016-0200-5.

BERENICE CLIFTON-GARCÍA[1]

JUAN VILLAFAÑA-ROJAS[2]

ORFIL GONZÁLEZ-REYNOSO[3]

JORGE RAMON ROBLEDO-ORTIZ[1]

RICARDO MANRÍQUEZ-GONZÁLEZ[1]

PORFIRIO GUTIÉRREZ-GONZÁLEZ[4]

YOLANDA GONZÁLEZ-GARCÍA[1]

Centro Universitario de Ciencias Exactas e Ingenierías, Universidad de Guadalajara. Olímpica, Guadalajara, Jal

Departamento de Biotecnológicas y Ambientales, Universidad Autónoma de Guadalajara, Zapopan, Jal.

Centro Universitario de Ciencias Exactas e Ingenierías, Universidad de Guadalajara. Olímpica, Guadalajara, Jal.

Centro Universitario de Ciencias Exactas e Ingenierías, Universidad de Guadalajara. Olímpica, Guadalajara, Jal.

UPOTREBA AIRLIFT BIOREAKTORA SA UNUTRAŠNJOM PETLJOM ZA PROIZVODNJU POLIHIDROKSIJALKANOATA POMOĆU *Stenotrophomonas rhizophila*

Bioreaktori tipa air-lifta imaju prednosti u odnosu na konvencionalne sisteme, kao što su efikasan prenos mase, jednostavnost konstrukcije i niska potrošnja energije. Zbog toga su oni dobra alternativa za proizvodnju polihidroksialkanoata (PHA), ali njihova upotreba u tu svrhu skoro da nije proučavana. Ovaj rad se bavi dizajnom, konstrukcijom i hidrodinamičkom karakterizacijom bioreaktora tipa air-lifta sa unutrašnjom petljom od 2,4 lL, procenjujući efekat protoka vazduha, zapremine tečnosti i položaja disperzatora na međufaznu površinu i vreme mešanja. Zatim je korišćen za proizvodnju PHB pomoću Stenotrophomonas rhizophila iz melase šećerne trske. Utvrđeno je da su uslovi za povećanje međufazne površine i minimiziranje vremena mešanja bili: protok vazduha od 1,5 vvm, zapremina tečnosti od 2400 ml i pozicija distributora od 5 mm (udaljenost između distributora vazduha i centralne cevi). U toj konfiguraciji, maksimalna koncentracija biomase, proizvodnja PHB i akumulacija PHB (54 h kulture) bili su 65,4 g/l, 39,9 g/l i 60,2 % (g PHB/100 g suve biomase), redom. Dobijeni polimer je poli-3-hidroksibutirat, sa tačkom topljenja od 170 °C, kristaliničnošću od 56,4 % i molekulskom masom od 735 kDa.

Ključne reči: airlift bioreaktor; melasa; polihidroksialkanoati; Stenotrophomonas rhizophila.

NAUČNI RAD

MOSTAFA HASSANEIN
HUSSEIN MOHAMED

Chemical Engineering
Department, Higher Institute of
Engineering – Shorouk Academy–
Shorouk City, Cairo – Egypt

SIMULTANEOUS MULTI-OBJECTIVE FRAMEWORK OF NATURAL GAS PIPELINE NETWORK OPERATIONS

Article Highlights

- TOPSIS-based multi-objective optimization is proposed
- Minimize power consumption, maximize gas flow rate, and optimize line pack
- Proven effectiveness in three case studies
- Economical gas transportation networks
- Versatile application across network scenarios

Abstract

The optimization of gas transportation networks is essential as natural gas demand increases. Conflicting objectives, such as maximizing delivery flow rate, minimizing power consumption, and maximizing line pack, pose challenges in this context. To address these complexities, a novel multi-objective optimization method based on the Technique for Order of Preference by Similarity to Ideal Solution (TOPSIS) is proposed. The method generates a diverse set of Pareto optimal solutions, empowering decision-makers to select the most suitable solution for gas transportation networks. Three case studies validate the approach's effectiveness, showcasing its advantages in yielding more economical networks and enhancing the cost-effectiveness of natural gas transmission networks. The proposed method's versatility allows application to various gas transportation network scenarios. Decision-makers benefit from a range of Pareto optimal solutions, providing valuable insights. Moreover, the seamless integration of the proposed method into existing gas transportation network optimization frameworks further enhances performance. In conclusion, the study presents a robust multi-objective optimization method based on TOPSIS for gas transportation network optimization. It offers cost-effective solutions and improves the efficiency of natural gas transmission networks. The provision of diverse Pareto optimal solutions enables well-informed decision-making, contributing to sustainable energy solutions in the face of increasing natural gas demand.

Keywords: gas pipeline network; multi-objective optimization; power demand; topsis; line pack; mathematical modeling.

Natural gas is gaining increasing recognition as a primary energy source for the future due to its numerous advantages, including reduced greenhouse gas emissions and lower capital costs. It has emerged as a competitive option in various sectors, particularly in newly developed power generation facilities. The importance of natural gas as a major energy exporter is evident in three key sectors: residential/commercial, industrial, and electric production. The residential/commercial sector relies on natural gas mainly for heating and cooking purposes, while the industrial sector utilizes it in diverse processes, such as chemical production and manufacturing. In the electric generation sector, natural gas is increasingly popular for power generation due to its cost-effectiveness and low emissions. Its unique properties, such as ease of

transportation through pipelines and high energy density, contribute to its reliability and versatility as an energy source. Additionally, natural gas can be stored for extended periods, ensuring a dependable energy supply even during times of high demand or supply disruptions [1].

In summary, natural gas is a promising energy exporter for the future, offering numerous advantages. It is reliable and versatile, catering to residential/commercial, industrial, and electric production sectors. The gas industry involves production, transportation, and sales, primarily focused on pipeline networks categorized as transition and distribution. In pipeline operations, operators prioritize three key objectives: delivery flow rate, economic advantage, and line pack. Factors influencing gas delivery include production capacity, consumer demand, transmission capacity, and storage availability. Economical advantage considers purchasing costs, sales revenue, and pipeline operating expenses. Line pack refers to the stored gas volume in the pipeline. These objectives guide decision-making for efficient and cost-effective gas transportation [2].

Pipeline operations optimization aims to maximize delivery flow rate and line pack while minimizing power consumption, taking into account intricate factors at play. Designing gas transmission networks involves selecting optimal solutions to minimize costs and adhere to restrictions, using advanced mathematical techniques and modeling methodologies. The network comprises gas-collecting pipelines, transition pipelines, distribution pipelines, compressor terminals, and distribution terminals [3]. Gas assembly pipelines collect raw natural gas from output wells and transport it to treatment plants for purification. Transition pipelines then carry purified natural gas over long distances, sometimes spanning thousands of kilometers, from treatment plants to city portal terminals. Finally, distribution pipelines distribute the natural gas to end consumers. Proper planning, design, and maintenance of this critical infrastructure are essential to ensure safety and efficient natural gas transition to meet consumer demands.

In a study by Kashani and Molaei [4], a multi-objective approach was employed to optimize three opposing thematic missions: the highest possible gas delivery rate, maximum line pack, and lowest feasible operating cost. The proposed approach aims to simultaneously optimize these objectives, which may conflict with each other while considering the interdependence and complexity of pipeline operations. This multi-objective optimization enables pipeline operators to make informed decisions that strike a

balance between these objectives, leading to more efficient and cost-effective pipeline operations. By considering multiple objectives, pipeline operators gain a better understanding of the trade-offs involved, aiding in the planning and execution of natural gas transmission pipeline networks, including design and operation. The main objective functions in natural gas pipeline optimization include maximizing gas delivery to specific consumers [3,5], maximizing line pack to meet peak demand and mitigate supply fluctuations [4], and maximizing economic benefit by optimizing gas sales yield and operational costs [6].

In summary, the objective function plays a crucial role in pipeline optimization, guiding the method to balance gas delivery, line pack, and economic benefit. da Silva *et al.* [7] conducted a multi-objective optimization study to assist regulatory decision-making in natural gas transition network design, considering conflicting goals of reducing transitional rent and maximizing imparted gas volume. Suet *et al.* [8] improved a multi-objective optimization process, considering uncertainties in supply conditions and consumption patterns to simultaneously reduce power request and gas supply shortage risk. Liu *et al.* [9] enhanced a dynamic pipeline network paradigm by accurately determining the compressibility factor, aiming to minimize compression costs while considering uncertainties in request and gas composition. These studies provide valuable tools for decision-makers in designing and planning natural gas pipeline networks with improved efficiency and cost-effectiveness.

The proposed approach considers uncertain gas composition and flow rates, using sequential repetitions to achieve a robust and cost-effective solution for optimizing natural gas pipeline networks. Chen *et al.* [10] developed a stochastic multi-objective optimization paradigm that accounts for uncertainties in gas demand and optimizes compressor and belowground gas store operation. The complex paradigm addresses various constraints, reducing operational costs and increasing line pack to achieve optimal solutions. Yin *et al.* [11] developed a surrogate modeling approach using machine learning to regulate flow in the process piping network. The hybrid model enhances computational speed while maintaining accuracy, leading to improved pipeline performance, cost savings, and enhanced safety. These studies offer valuable tools for decision-makers to optimize natural gas pipeline networks, considering uncertainties and enhancing overall efficiency.

Building upon the insights gleaned from the literature review, which accentuates the complexities

and conflicting objectives in gas transportation network optimization.

This paper aims to tackle these challenges. The proposed methodology in this study utilizes (TOPSIS) to optimize natural gas pipeline networks, introducing innovative elements compared to prior research. Notably, TOPSIS excels in handling multi-objective optimization challenges, simultaneously addressing conflicting objectives such as gas delivery flow rate, line pack, and operating cost. The approach integrates sophisticated mathematical models and advanced simulation tools, showcasing versatility in decision-making processes. An emphasis on considering uncertainties in gas composition and flow rates, along with the utilization of sequential repetitions, enhances the robustness of the proposed solution. The versatility of the TOPSIS method itself is highlighted as it adapts to the intricacies of gas transportation network optimization.

Furthermore, the article sets itself apart by practically validating the proposed method through three case studies, demonstrating its effectiveness in achieving cost-efficiency and improved performance.

In conclusion, this study contributes significantly to the field by offering a comprehensive and innovative approach that builds upon the existing literature, providing decision-makers with a robust tool for optimizing natural gas pipeline networks.

MATERIAL AND METHODS

Formulation model for gas pipeline network

Gas pipeline network models can be constructed using a variety of mathematical techniques, such as optimization method, like linear and nonlinear programming (LP), mixed-integer linear programming (MILP), nonlinear programming (NLP), and mixed-integer nonlinear programming (MINLP), as well as graph theory and simulation models for simulating gas flow behaviour under various conditions.

The gas pipeline network formulation form involves defining the objective function, decision variables, constraints, network topology, gas properties, and input data. Subsequently, an appropriate optimization or simulation method is applied to determine the optimal solution that satisfies the requirements of the problem. The selection of the most suitable mathematical technique and optimization or simulation method relies on the specified properties of the gas pipeline network and the problem being addressed [1]. Fig. 1 depicts the typical steps involved in the TOPSIS method that are adopted in this study.

Figure 1. Flow chart of typical steps involved in the TOPSIS approach.

Gas properties

Gas properties are essentially for understanding and predicting the behavior of gases in different applications, including process design, combustion analysis, and gas transportation. The calculation of gas properties relies on fundamental principles of thermodynamics, fluid mechanics, and molecular theory by Menon [12]. Some of these properties that are commonly calculated for gases include.

Gas density

The density and pressure of a gas as shown in the following equation form are associated by entering the compression coefficient, Z in the paradigm.

$$\rho = \frac{PM}{ZRT} \tag{1}$$

where R is the universal gas constant, M is the gas's average molecular weight and relies on its composition. Gas molecular weight is estimated using the easy blending rule stated in the succeeding equation form in which Y_i & M_i are the mole fractions and molecular weights of sorts, respectively.

$$M = \sum M_i Y_i \tag{2}$$

Compressibility factor

The compression coefficient compressibility factor Z is utilized to change the perfect gas equation to consideration for the real gas demeanor. Conventionally, the compression coefficient is

estimated using an equation of state, this coefficient can be uttered as a function of the characteristics of the critical gas mixture T_C, average pressure P_{avg}, of the tube part and the temperature T.

$$Z = 1 + \left(0.257 - 0.533 \frac{T_c}{T} \right) \frac{P_{avg}}{P_c} \tag{3}$$

The average pseudo-critical properties of the gas mixture

The pseudo-critical temperature (T_c) and pseudo-critical pressure (P_c) for natural gas can be approximated using an adequate blending rule that takes into account the critical properties of the individual components of the gas, Y_i:

$$T_c = \sum T_{Ci} Y_i \tag{4}$$

$$P_c = \sum P_{Ci} Y_i \tag{5}$$

Average pressure

The average pressure of gas can be calculated from the below formula [13]:

$$P_{avg} = \frac{2}{3} \left(P_1 + P_2 - \frac{P_1 \cdot P_2}{P_1 + P_2} \right) \tag{6}$$

Specific gravity

The specific gravity of a fluid is defined as the ratio of its density to the density of a reference fluid, such as water or air, at a standardized temperature:

$$S_g = \frac{density\ of\ gas}{density\ of\ air} = \frac{M_{gas}}{M_{air}} \tag{7}$$

The average molecular weight of the gas mixture

The gas molecular weight is estimated through the blending rule, as

$$M_{gas} = \sum M_i Y_i \tag{8}$$

PIPELINE NETWORK CALCULATIONS

Pipeline volume flow rate equation

The flow equation establishes a mathematical relationship between gas flow rate Q, gas properties T_b, G, T, Z, f, pressure P_b, pipe diameter D, and the equivalent length of a horizontal pipe Le, as given by [13].

$$Q = 77.54 \left(\frac{T_b}{P_b} \right) \left(\frac{P_1^2 - P_2^2}{G \cdot T \cdot Le \cdot Z \cdot f} \right) D^{2.5} \tag{9}$$

Friction factor

The friction factor f in pipeline flow is a dimensionless quantity that characterizes the resistance to flow caused by the roughness of the pipeline surface and other factors such as turbulence and viscosity. It is an important parameter in pipeline design and operation, as it affects the pressure drop and energy losses. It can be determined using empirical equations or experimental data. The most commonly used equation for estimating the friction coefficient is the Nikuradse equation, which is an implicit equation that relates the friction factor to the roughness height of the pipeline surface (ε), and the diameter of the pipeline (D). The Nikuradse equation is given by Mohitpour et al. [14]:

$$\frac{1}{\sqrt{f}} = -2 \log \left(\frac{\varepsilon / D}{3.7} \right) \tag{10}$$

Power demand reduction

In transition systems of natural gas, compressor stations consume a significant portion of energy. Thus, decreasing their energy requirements can efficiently raise the competence of the pipeline system and the operating revenue. In addition, most compressors run on gas. Turbines decrease the energy requirement of the compressor stations which have the potential to mitigate greenhouse gas emissions, thereby contributing to environmental sustainability. Given this, it is not surprising that reducing the energy requirement of compressors is a major purpose to improve gas transition systems. Compressor stations play a critical role in the operation of natural gas pipelines, by providing the necessary energy to maintain gas flow and pressure throughout the pipeline system [4]. The energy complemented via the compressor's energy input is approximated as "head" (H), which represents the amount of energy delivered per unit mass of gas. The value of H can be obtained using Eq. (11):

$$H = ZRT \frac{K}{K-1} \left[\left(\frac{P_d}{P_s} \right)^{\frac{(K-1)}{K}} - 1 \right] \tag{11}$$

where K is estimated by the Pambour equation [15]:

$$K = \frac{\sum C_{pi} M Y_i}{\sum C_{pi} M Y_i - R} \tag{12}$$

The energy transferred to the gas within the compressor can be estimated by knowing the compressor head H, gas flow rate Q and isentropic efficiency η_{is}, as described by Demissie [16]:

$$Power = \frac{Q \cdot H}{\eta_{is}} \tag{13}$$

Line pack in pipeline

Line pack LP indicates the quantity of gas that is contained within a pipeline to maintain system pressure and meet fluctuations in demand. When natural gas is delivered through a pipeline system, the gas flow rate and pressure can vary depending on the demand from customers. To ensure that the system pressure remains within a safe and efficient range, pipeline operation often uses a line pack to store excess gas. Gas is stored in pipelines during periods of low demand and subsequently discharged during periods of elevated demand.

Line pack is typically measured in terms of the amount of gas stored per unit length of pipeline, such as cubic feet per mile, or cubic meters per kilometer. The amount of line pack that is required is contingent upon a multitude of factors, such as the dimensions and throughput of the pipeline, the consumption patterns of end-users, and the properties of the gas flow, such as temperature and pressure. The value of LP in MMscf is determined by using the following equation [12]:

$$LP = 7.885 \cdot 10^{-7} \left(\frac{T_{SC}}{P_{SC}} \right) \left(\frac{P_{avg}}{Z \cdot T} \right) \left(D^2 \cdot L \right) \qquad (14)$$

Total cost

The total cost of a natural gas network is subject to influence by several factors such as length, diameter, pressure, and flow rate capacity requirements of the pipelines. It equals the summation of operating and fixed costs [17]:

$$Operating \ \text{cost} = 100000 + \left(Power \cdot 850 \right) \qquad (15)$$

Here, "$Power$" represents the power consumption in the natural gas network. It is the energy consumed by compressors, as mentioned in the discussion about power demand reduction. The operating cost includes a fixed component of 100,000 which could represent baseline operational expenses. The variable component $(Power \times 850)$ captures the cost associated with energy consumption, likely from compressors, as they play a crucial role in maintaining gas flow and pressure.

$$Fixed \ \ cost = \left(1495.4 \cdot Ln(Y_r) - 11353 \right) \cdot D \cdot 250 \cdot \frac{L}{1600} \qquad (16)$$

The fixed cost is determined by a combination of factors, and the natural logarithm of the number of years (Yr) is involved, indicating that the cost structure may be influenced by the duration of the operation. The specific constants and factors used in the equation are likely derived from empirical data or a detailed analysis of the network's characteristics and operational history.

MULTIPLE CRITERIA DECISION MAKING (MCDM)

Multiple criteria decision-making (MCDM) refers to a methodology for decision-making framework that is used to evaluate and select alternatives based on multiple criteria or objectives. MCDM is a useful tool in situations where there are multiple and competing objectives that need to be considered when making decisions. The MCDM process involves identifying the decision problem and the available alternatives, determining the criteria or objectives that are relevant to the problem, determining the relative significance of the criteria, and evaluating the alternatives based on the criteria, this can be done using various techniques, such as scoring or ranking the alternatives based on their performance on each criterion. Once the alternatives have been evaluated, the decision-maker needs to determine the trade-offs between the different criteria or objectives. This involves balancing the relative significance of each criterion against the performance of each alternative on that criterion, and finally making the decision based on the overall evaluation. MCDM has a wide range of uses in disciplines such as finance, engineering, environmental management, and healthcare, among others, are encompassed. However, it is important to note that MCDM can be challenging due to the subjective nature of the evaluation process, the difficulty in assigning weights to criteria, and the potential for information overload. Therefore, it is important to use a rigorous and transparent decision-making process that involves multiple stakeholders and to continually review and update the criteria and weights as new information becomes available [18]:

$$\varphi = \begin{array}{c} \\ \gamma_1 \\ \gamma_2 \\ : \\ : \\ \gamma_m \end{array} \begin{array}{cccccc} \beta_1 & \beta_2 & .. & .. & \beta_n \\ \left[\lambda_{11} \right. & \lambda_{22} & .. & .. & \lambda_{2n} \\ \lambda_{21} & \lambda_{22} & .. & .. & \lambda_{2n} \\ .. & .. & .. & .. & .. \\ .. & .. & .. & .. & .. \\ \lambda_{m1} & \lambda_{m2} & .. & .. & \left. \lambda_{mm} \right] \end{array} \qquad (17)$$

where γ_i, ($i = 1,2, \ldots \ldots, m$) are alternative and β_j, ($j = 1,2 \ldots \ldots, n$) are criteria for a clear view of this method. The TOPSIS method consists of a series of sequential steps that are presented next.

Step1: The most common normalization method is:

1-for max, we have:

$$\eta_{i,j} = \frac{\lambda_{ij} - \min \left(\lambda_{ij} \right)}{\max \left(\lambda_{ij} \right) - \min \left(\lambda_{ij} \right)}, \left(i \in m, \ j \in n \right) \qquad (18)$$

2-for max, we have:

$$\eta_{i,j} = \frac{\max(\lambda_{ij}) - \lambda_{ij}}{\max(\lambda_{ij}) - \min(\lambda_{ij})}, (i \in m, j \in n) \quad (19)$$

As a result, a standardized decision matrix M is acquired indicating the relative performance of the substitutions as:

$$\mu = \begin{bmatrix} \eta_{11} & \eta_{12} & .. & .. & \eta_{1n} \\ \eta_{21} & \eta_{22} & .. & .. & \eta_{21} \\ .. & .. & .. & .. & .. \\ .. & .. & .. & .. & .. \\ \eta_{m1} & \eta_{m2} & .. & .. & \eta_{mn} \end{bmatrix} \quad (20)$$

Step 2: The standard deflection method estimates the weights of purposes through:

$$\tau_i = \frac{\sigma_i}{\sum_k^m \sigma_k} \quad (21)$$

$$\sigma_i = \sqrt{\frac{\sum_{j=1}^m (\lambda_i - \lambda^\sim)^2}{n-1}} \quad (22)$$

$$\lambda^\sim = \sum_{i=1}^m \frac{\lambda_i}{n} \quad (23)$$

Step 3: A set of weights $(\tau_1, \tau_2 ....\tau_n)$ and $\sum_i^n \tau_i = 1$, where $\tau_i > 0$, $(i = 1, 2… n)$ is given to the corresponding criterion λ_i, where $(i = 1,2,…,n)$.

The matrix $\varepsilon = \tau_i \eta_{ij}$ is calculated by multiplying the elements at each column of the matrix μ by their associated weights τ_i, $(i = 1,…,n)$.

$$\varepsilon = \begin{bmatrix} \tau_1\eta_{11} & \tau_2\eta_{12} & .. & .. & \tau_n\eta_{1n} \\ \tau_1\eta_{21} & \tau_2\eta_{22} & .. & .. & \tau_n\eta_{21} \\ .. & .. & .. & .. & .. \\ .. & .. & .. & .. & .. \\ \tau_1\eta_{m1} & \tau_2\eta_{m2} & .. & .. & \tau_n\eta_{mn} \end{bmatrix} \quad (24)$$

Step 4: Calculate the separation measures $(\alpha_i^+ \text{ and } \alpha_i^-)$ between alternatives using the distance MinkowskiLp Metric as follows:

$$\alpha_i^+ = \sqrt{\sum_{j=1}^m (\varepsilon_{ij} - \varepsilon_j^+)^2}, (i = 1,.....,n) \quad (25)$$

$$\alpha_i^- = \sqrt{\sum_{j=1}^m (\varepsilon_{ij} - \varepsilon_j^-)^2}, (i = 1,.....,n) \quad (26)$$

Step 5: In terms of performance evaluation of alternatives, the higher the value, the better the performance.

The optimum alternative is selected according to the

greater relative closeness [18].

$$\theta_i = \frac{\alpha_i^-}{\alpha_i^- + \alpha_i^+}, 0 \le \theta_i \le 1 \quad (27)$$

CASE STUDIES

Case1 (linear)

The linear case consists of six nodes with three pipe arcs: (1-2), (3-4), and (5-6), forming a two-compressor network. The length of each pipe in this case is 80 km. The internal diameter of all pipes is designated as NPS 36 with a wall thickness of 0.952 cm, and a friction factor of 0.0090 is assumed. The reference values for temperature and pressure are established as 15.7 °C and 101.32 kPa, respectively. The compressors available can be represented as a tuple set ((2,3), (4,5)). Each station designated for compression in Case 1 has five centrifugal units operating in parallel [19]. The physical properties of the gas mixture in Case 1 are shown in Table 1. The pipeline network for Case 1 is depicted in Fig. 2.

Table 1. Physical properties of the gas mixture.

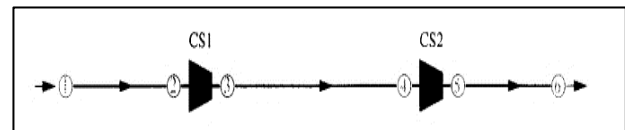| Gas component	C_1	C_2	C_3
Mole Fraction Y_i	0.700	0.250	0.050
Molecular mass(gmole^{-1})	16.040	30.070	44.100
Lower heating value at 15 °C and 1 bar (MJm^{-3})	37.706	66.067	93.936
Critical pressure (kPa)	4600	4880	4250
Critical temperature (°C)	-82.50	32.40	96.65
Heat capacity at constant pressure ($J.mol^{-1}.°C$)	35.663	52.848	74.916

Figure 1. Pipeline network for Case 1.

Table 2 displays data specifications for different scenarios including pressure ranges, flow rate, power, and line pack for Case 1.

Table 2. Data specifications for Case 1.

Scenario	P_{min} (kPa)	P_{max} (kPa)	Flowrate (MMscf)	Power (kW)	Line pack (MMscf)
1	4136.8	5515.8	860.576	7158.7	42.022
2	4205.8	5515.8	806.789	4175.9	43.008
3	4274.7	5515.8	757.986	5644.9	45.876
4	4481.5	5171.0	576.585	2542.8	43.411
5	4619.4	5377.9	694.127	2207.2	45.031

Case2 (Tree)

This Tree case consists of ten nodes with six arcs: (2-3), (4-5), (5-6), (5-7), (8-9), and (9-10). The length of each pipe in this case is 80 km. The inside diameter of all pipes is NPS 36 with a wall thickness of 0.952 cm, and the friction factor is 0.0090. The

reference temperature and pressure for the system are predetermined as 15.7 °C and 101.32 kPa, respectively. All compressor stations in Case 2, denoted by the tuple set {(1,2), (3,4), (3,8)}, are equipped with five centrifugal units operating concurrently [19]. The physical characteristics of the gas mixture in Case 2 are exhibited in Table 1. The pipeline network for Case 2 is shown in Fig. 3. Table 3 displays data specifications for different scenarios, including pressure range, flow rate, power, and line pack.

Table 3. Data specifications for Case 2.

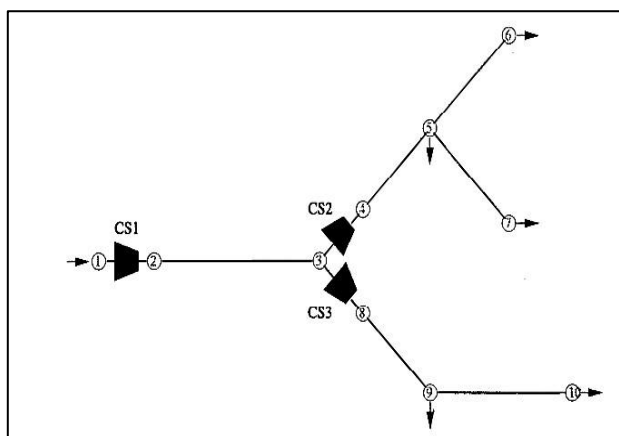| Scenario	P_{min} (kPa)	P_{max} (kPa)	Flowrate (MMscf)	Power (kW)	Line pack (MMscf)
1	4136.8	5515.8	645.432	3989.4	140.640
2	4481.5	5171.0	392.203	1957.4	141.900
3	4619.4	5308.9	579.248	2981.3	147.130
4	4757.3	5446.8	418.182	3161.7	149.200
5	5171.0	5515.8	501.620	1517.4	155.207

Figure 3. Pipeline network for Case 2.

Case 3 (Branched)

The Branched case consists of a pipeline network with twenty nodes and nineteen arcs. Table 4 displays the dimensions of the length and inner diameter for each arc, along with data specifications for different scenarios, including pressure range, flow rate, power, and line pack for Case 3 [20].

The reference temperature and pressure for the system in Case 3 are specified as 15.7 °C and 101.32 kPa, respectively. The relevant physical properties of the gas mixture in Case 3 have been presented in Table 1. The pipeline network for Case 3 is exhibited in Fig. 4.

RESULTS AND DISCUSSION

Hydrodynamic characterization

Table S1 (Supplementary material) contains the normalized decision matrix, standard deviation (σ_i), objective weight (τ_i) results, and the weighted normalized decision matrix for Case 1. The normalized decision matrix result is calculated by using Eqs. (18) and (19). By using the TOPSIS method, which was presented previously, the standard deviation (σ_i) and the objective weight (τ_i) results are obtained using Eqs. (21) and (22).

In the next step, calculate the separation measures and relative closeness by using Eqs. (25–27). The total costs, which are the sum of Eqs. (15) and (16), are exhibited in Table S2.

Table 4. Data specifications, length, and inside diameter data for Case 3.

Data Specifications for Case 3					
Scenario	P_{min} (kPa)	P_{max} (kPa)	Flowrate (MMscf)	Power (kW)	Line pack (MMscf)
1	2901.7	7704.2	963.205	295.29	7877.17
2	2901.7	7504.2	946.178	243.09	7533.44
3	2901.7	7304.3	1478.43	228.18	7413.52
4	2901.7	7103.6	1446.62	464.57	7143.05
5	2901.7	6903.7	1414.36	473.51	6877.93
Length and inside diameter data for Case 3					
Arc	Diameter (cm)	Length (km)	Arc	Diameter (cm)	Length (km)
(1-2)	50.80	4.02	(11-12)	66.04	42.24
(2-3)	76.20	6.03	(12-13)	60.96	40.23
(3-4)	71.12	26.15	(13-14)	60.96	5.02
(5-6)	30.48	43.24	(14-15)	86.36	10.05
(6-7)	15.24	29.16	(15-16)	76.20	25.13
(7-4)	30.48	19.10	(11-17)	30.48	10.55
(4-14)	60.96	55.31	(17-18)	27.94	26.15
(8-9)	86.36	5.02	(18-19)	35.56	98.57
(10-11)	71.12	25.13	(19-20)	30.48	6.03
(9-10)	86.36	20.11			

The optimum scenario is the fifth one with the highest relative closeness when pressures range (4619.4:5377.9 kPa). Table S3 displays the normalized decision matrix, standard deviation (σ_i), objective

weight (τ_i) results, and the weighted normalized decision matrix for Case 2.

The separation measures, relative closeness, and total cost results are exhibited in Table S4. The

Figure 4. Pipeline network for Case 3.

(5171:5515.8 kPa).Table S5 displays the normalized decision matrix, standard deviation (σ_i), objective weight (τ_i)results, and the weighted normalized decision matrix for Case 3.

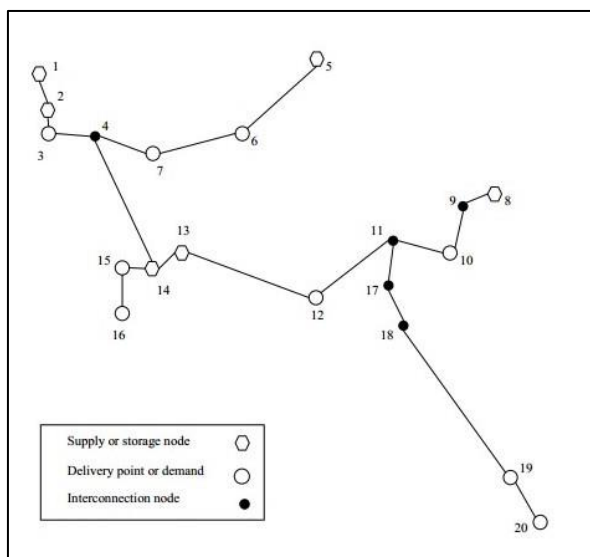The separation measures, relative closeness, and total cost results are exhibited in Table S6. The optimum scenario is the third one with the highest relative closeness when pressures range (2901.7:7304.3 kPa). The calculations of total cost coincide with relative closeness for the three cases whereas scenarios 5 and 3 have the minimum total cost among all scenarios which confirms the accuracy, reliability, and robustness of our proposed method.

The research holds significant value by providing valuable insights into the optimization of gas pipeline networks, empowering industry stakeholders to make well-informed decisions, and enhancing efficiency, reliability, and cost-effectiveness. The proposed TOPSIS approach expands on existing multi-objective optimization techniques for gas pipeline networks in several ways. First, it integrates sophisticated hydraulic and thermodynamic models from previous studies to accurately capture the physics of gas flow. Second, it utilizes a systematic TOPSIS framework to effectively handle trade-offs between conflicting objectives. This provides an advantage over prior weighted sum methods that can struggle with balancing multiple goals [21–23].

Finally, the technique emphasizes robustness under uncertainties, leveraging sequential runs and stochastic modeling to maintain reliability - going beyond deterministic approaches. By leveraging the strengths of different methodologies, this study's TOPSIS-based technique offers a novel synthesis that enhances multi-objective optimization for gas transport.

Future research can expand on this work by exploring alternative optimization techniques, incorporating environmental impact, and safety considerations, and assessing scalability for larger and more complex gas transmission networks. Integrating advanced machine learning and artificial intelligence techniques can also enhance the model's performance.

CONCLUSION

The proposed multi-objective optimization model demonstrates significant potential for improving efficiency, reducing costs, and minimizing fuel consumption in gas transmission networks. The TOPSIS-based approach for handling conflicting objectives offers a novel and effective solution tailored to the complex challenges faced by industry. The model shows promising results in test cases, providing valuable insights into balancing total cost and fuel consumption. This simultaneously considers economic and environmental objectives to support informed decision-making. Further validation on large-scale networks is needed, but the technique shows significant potential for real-world application. The most significant implications of this study are in its ability to simultaneously optimize multiple objectives that are typically addressed separately. By considering delivery flow rate, power consumption, and line pack holistically, more optimized and sustainable solutions can be identified. The insight gained on trade-offs between total cost and fuel consumption is particularly valuable for informed decision-making by gas companies.

In summary, this work demonstrates a significant advancement in gas transmission network optimization that can overcome key limitations of current approaches. With further development, this technique can provide an advanced tool for next-generation pipeline optimization - enabling more effective modeling, planning, and management. The multi-objective technique provides a promising new tool for tackling complex pipeline optimization problems.

ACKNOWLEDGMENT

NOMENCLATURE

σ_i	Standard deviation of performance rating factor ($P_1j,P_2j,\ldots\ldots P_mj$) in the R matrix.
τ_i	Objective weight
P_b	Base pressure (psia)
T_b	Base temperature (°R)
P_1	Is upstream pressure (psia)

P_2	Downstream pressure (psia)
T_f	Gas flowing temperature (°R)
ρ_g	Gas density (lb/ft$^{3)}$
P_{air}	Air density (lb/ft$^{3)}$
D	Pipe inside diameter (inch)
L_e	Equivalent length (mile)
G	Gas gravity
T_{SC}	Suction compressor Temperature (°R)
P_{SC}	Suction compressor Pressure (psia)
R	Universal gas constant (1545 ft. lbf/lbm mol °R)
$Mwt_{(avg.)}$	Average molecular weight of gas
$Mole\% (i)$	Mole percent of each component in gas
$Mwt (i)$	Molecular weight of each component in gas
T_{PC}	Pseudo critical temperature (°R)
P_{PC}	Pseudo critical pressure (psi)
$Pavg$	Average pressure (psi)
T	Gas temperature (K)
T_C	Critical temperature (K)
P_C	Critical pressure (psi)
K	Specific heat ratio (cp/cv) assume it to be 1.26
T_1	Suction temperature (°R)
y_i	Mole fraction of percent of gas component i, dimensionless
M_i	Molecular weight of gas component j, (g/mol)
LHV_i	Mass low heating value of molecules composing the gas (kJ/kg)
$MMscf$	Million standard cubic feet per day

REFERENCES

[1] X. Wu, C. Li, Y. He, W. Jia, Math. Probl. Eng. (2018)1267045. https://doi.org/10.1155/2018/1267045.

[2] C.Li, W.Jia, E.Liu, X. Wu,Int. J. Ind. Eng.19 (6) (2012) 241–251. https://doi.org/10.23055/ijietap.2012.19.6.631.

[3] S. Mokhatab, W.Poe, J.Mak, Handbook of natural gas transmission and processing: principles and practices, Gulf Professional Publishing, (2018) ISBN:0128016647, 9780128016640.

[4] A. Kashani, R. Molaei, Chem. Eng. Res. Des.92 (2014) 2106–2122. https://doi.org/10.1016/j.cherd.2014.02.006.

[5] X. Wu, C. Li, W. Jia, Y. He, J. Nat. Gas Sci. Eng. 21 (2014) 10–18. https://doi.org/10.1016/j.jngse.2014.07.028.

[6] H. Üster, Ş. Dilaveroğlu, Appl. Energy133 (2014) 56–69. https://doi.org/10.1016/j.apenergy.2014.06.042.

[7] F.da Silva, J.de Souza, A.Costa, Comput. Chem. Eng.93(2016) 212–220. https://doi.org/10.1016/j.compchemeng.2016.06.006.

[8] H. Su, E. Zio, J. Zhang, X. Li, L. Chi, L. Fan, Z. Zhang, Comput. Chem. Eng.131 (2019) 106584. https://doi.org/10.1016/j.compchemeng.2019.106584.

[9] K. Liu, L.Biegler, B. Zhang, Q. Chen, Chem. Eng. Sci. 215 (2020) 115449. https://doi.org/10.1016/j.ces.2019.115449.

[10] Q. Chen, C. Wu, L. Zuo, M. Mehrtash, Y. Wang, Y. Bu, R. Sadiq, Y. Cao, Comput. Chem. Eng.147 (2020) 107260. https://doi.org/10.1016/j.compchemeng.2021.107260.

[11] X. Yin, K. Wen, Y. Wu, X. Han, Y. Mukhtar, J. Gong, J. Nat. Gas Sci. Eng.98 (2022) 104384. https://doi.org/10.1016/j.jngse.2021.104384.

[12] E. Menon, Gas pipeline hydraulics, Online Course (2005). https://doi.org/10.1201/9781420038224.

[13] P. Coelho, C. Pinho, J. Brazilian Soc. Mech. Sci. Eng.29 (3) (2007) 262–273. https://doi.org/10.1590/S1678-58782007000300005.

[14] M. Mohitpour, H. Golshan, M. Murray, Pipeline Design & Construction: A Practical Approach, 3rdEd, American Society of Mechanical Engineers, (2007). https://doi.org/10.1115/1.802574.

[15] K. Pambour, R. Bolado-Lavin, G.Dijkema, J. Nat. Gas Sci. Eng. 28 (2016) 672–690. https://doi.org/10.1016/j.jngse.2015.11.036.

[16] A. Demissie, W. Zhu, C. Belachew, Comput. Chem. Eng.100 (2017) 94–103. https://doi.org/10.1016/j.compchemeng.2017.02.017.

[17] T.Edgar, D.Himmelblau, L.Lasdon, Optimization of chemical processes, McGraw Hill, New York,(2001). https://doi.org/10.1002/aic.690490128.

[18] C. Hwang, K. Yoon, Multiple Attribute Decision Making: Methods and Applications, 1st Ed, Springer, Berlin 186 (1981) 58–191. https://doi.org/10.1007/978-3-642-48318-9.

[19] S. Wu, R. Rios, E. Boyd, L. Scott, Math. Comput. Model. 31 (2000) 197–220. https://doi.org/10.1016/S0895-7177(99)00232-0.

[20] F.Tabkhi, L. Pibouleau, C. Azzaro, S. Domenech, J. Energy Resour. Technol. 131 (4) (2009) 043002. https://doi.org/10.1115/1.4000325.

[21] D. Zhou, X. Jia, S. Ma, T. Shao, D. Huang, J. Hao, T. Li, Energy. 253 (2022). https://doi.org/10.1016/j.energy.2022.124068.

[22] J. Zhou, J. Peng, G. Liang, C. Chen, X. Zhou,Y. Qin, J. of Intell.& Fuzzy Systems. 40(3) (2021). 4345–4366. https://doi.org/10.3233/jifs-201072.

[23] M.H.H. Mohamed, H.A.A. Gawad, Deci. Making: Applic. in Manag. and Eng. 7, (2024) 420–441. https://doi.org/10.31181/dmame712024983.

MOSTAFA HASSANEIN
HUSSEIN MOHAMED

Chemical Engineering
Department, Higher Institute of
Engineering - Shorouk Academy -
Shorouk City, Cairo - Egypt

NAUČNI RAD

ISTOVREMENA VIŠEKRITERIJUMSKA OPTIMZACIJA RADA GASOVODA ZA PRIRODNI GAS

Optimizacija transportnih mreža gasovoda je od suštinskog značaja kako se povećava potražnja za prirodnim gasom. Konfliktni ciljevi, kao što su maksimiziranje protoka, minimiziranje potrošnje energije i maksimiziranje zaliha u gasovodima, predstavljaju izazove u ovom kontekstu. Da bi se prevazišle ove složenosti, predložena je nova metoda višekriterijumske optimizacije zasnovane na tehnici za redosled preferencije po sličnosti sa idealnim rešenjem (TOPSIS). Metod generiše raznovrstan skup Pareto optimalnih rešenja, osnažujući donosioce odluka da izaberu najpogodnije rešenje za mreže gasovoda. Tri studije slučaja potvrđuju efikasnost pristupa, pokazujući njegove prednosti u stvaranju ekonomičnijih mreža i povećanju isplativosti mreža gasovoda za prirodni gas. Svestranost predložene metode omogućava primenu u različitim scenarijima mreže gasovoda. Donosioci odluka imaju koristi od niza Pareto optimalnih rešenja koji pružaju vredne uvide. Štaviše, besprekorna integracija predložene metode u postojeće okvire za optimizaciju gasovoda dodatno poboljšava performanse. U zaključku, studija predstavlja robusnu višekriterijumsku metodu optimizacije gasovoda zasnovanu na TOPSIS-u. Nudi isplativa rešenja i poboljšava efikasnost gasovoda prirodnog gasa. Pružanje raznovrsnih Pareto optimalnih rešenja omogućava donošenje odluka na osnovu dobrog informisanja, doprinoseći održivim energetskim rešenjima u uslovima sve veće potražnje za prirodnim gasom.

Ključne reči: gasovodna mreža; višeciljna optimizacija; potreba za snagom; TOPSIS; linijski paket; matematičko modeliranje.

EXPRESSION OF CONCERN

QUALITY RESTORATION OF WASTE POLYOLEFIN PLASTIC MATERIAL THROUGH THE DISSOLUTION-REPRECIPITATION TECHNIQUE

Hadi Jasim Arkan,[1,2] Najmuldeen Faisal Ghazi,[1] Ahmed Iqbal[1]

[1] Faculty of Chemical and Natural Resources Engineering, Universiti Malaysia Pahang, LebuhrayaTunRazak, Gambang, Kuantan, Pahang, Malaysia
[2] Department of Chemical Engineering, College of Engineering, University of Tikrit, Tikrit, Salahaldden, Iraq

We wish to inform our readers that concerns have been raised regarding the integrity of the data presented in the above-mentioned paper, specifically the duplication of images in Figures 1 and 2, which appear identical despite representing different materials. The issue has been flagged as a potential data integrity problem, and we are currently investigating the matter in collaboration with the authors.

At this stage, the investigation is ongoing, and we are awaiting clarification from the authors regarding the accuracy of the figures and the validity of the reported results. As part of our commitment to transparency and ensuring the highest standards of scholarly conduct, we will update our readers on the outcome of the investigation once it is concluded.

In the meantime, we advise readers to interpret the findings of the paper with caution. Should the investigation reveal any issues with the data, appropriate corrective actions, including a corrigendum or retraction, will be considered.

Date and Place

9, January 2025. Belgrade

Editor in Chief

Vlada B. Veljković